Magnétohydrodynamique confinée appliquée aux plasmas de fusion magnétiques

Jorge Morales Mena

N° d'ordre : 2013 – 25 ANNÉE 2013

ÉCOLE CENTRALE DE LYON
LABORATOIRE DE MÉCANIQUE DES FLUIDES ET D'ACOUSTIQUE

ÉCOLE CENTRALE LYON

UNIVERSITÉ DE LYON

THÈSE DE L'UNIVERSITÉ DE LYON

DÉLIVRÉE PAR L'ÉCOLE CENTRALE DE LYON

SPÉCIALITÉ : MÉCANIQUE DES FLUIDES

ÉCOLE DOCTORALE MEGA

CONFINED MAGNETOHYDRODYNAMICS APPLIED TO MAGNETIC FUSION PLASMAS

Préparée au Laboratoire de Mécanique des fluides et d'Acoustique
Soutenue publiquement le 1er Octobre 2013
par

JORGE A. MORALES

Directeur de thèse
WOUTER J.T. BOS

Jury de thèse

Rapporteurs	CAROLINE NORE
	MARINA BÉCOULET
Président	FABIEN S. GODEFERD
Examinateurs	WOUTER J.T. BOS
	HINRICH LÜTJENS
	KAI SCHNEIDER
Invités	YANN CAMENEN
	NICOLAS PLIHON

RÉSUMÉ

La description magnétohydrodynamique est utilisée pour étudier les plasmas de fusion par confinement magnétique dans deux configurations: tokamak et reversed field pinch. Une méthode de Fourier pseudo-spectrale et une technique de pénalisation en volume sont employées pour résoudre les équations. La méthode de pénalisation permet d'introduire des conditions aux limites de Dirichlet et donc de faire varier facilement la géométrie considérée. Les simulations dans des géométries toroïdales de type tokamak montrent l'apparition spontanée de vitesses. Une importante composante toroïdale se développe si le système est peu dissipatif. Il est aussi montré que la brisure de symétrie dans la forme de la section du tore fait apparaître un moment angulaire toroïdal. Pour le Reversed Field Pinch on montre l'émergence de structures hélicoïdales. La forme de ces structures varie en fonction des coefficients de transport ainsi que du paramètre de pincement du champ magnétique imposé. Pour compléter l'étude on compare les résultats du tore aux calculs dans un cylindre périodique. Les différences dans la dynamique des deux cas sont mises en avant. Finalement les simulations sont confrontées à des expériences et un meilleur accord est observé entre simulation et expérience pour la géométrie toroïdale que pour la géométrie cylindrique.

Mots clés : magnétohydrodynamique, tokamak, reversed field pinch, méthode de pénalisation en volume, méthode Fourier pseudo-spectrale, moment angulaire, influence de la toroïdicité.

ABSTRACT

A magnetohydrodynamic description is used to study magnetic fusion plasmas in two different configurations: tokamak and reversed field pinch. A Fourier pseudo-spectral method with a volume penalization technique are used to solve the system of equations. The penalization method is used to introduce Dirichlet boundary conditions and it allows to easily modify the consider geometry. The simulations of a tokamak configuration in a toroidal geometry show the spontaneous appearance of velocities. These velocities are dominated by their toroidal component if the system is little dissipative. It is also shown that the symmetry breaking of the cross section of the torus causes a toroidal angular momentum to develop. For the Reversed Field Pinch configuration we show the appearance of helical structures. The shape of these structures varies with the value of the transport coefficients and with the pinch ratio parameter of the imposed magnetic field. To complete the study, we compare the results of simulations obtained in toroidal and in periodic cylindrical geometries. The differences in the dynamics of these two cases are highlighted. Finally, simulations are compared to experimental data and a significant better agreement is observed between the simulation and the experiment for the toroidal geometry than for the cylindrical case.

Keywords: magnetohydrodynamics, tokamak, reversed field pinch, volume penalization method, spectral method, toroidal momentum, quasi single helicity, toroidicity effects.

CONTENTS

Notations **ix**

I Introduction **1**

II Numerical method and validation **5**

1 Introduction 5
2 MHD Equations 7
3 The numerical code 7
3.1 Pseudo-spectral discretization 7
3.2 Penalization method 8
3.3 Time-discretization 12
4 Parallel performances 14
5 Two-dimensional validation 15
5.1 Two-dimensional Taylor-Couette flow 16
5.2 The Z-pinch 18
5.3 Assessment of the regularization method to enhance the performance of the penalization method 20
6 Three-dimensional validation 21
6.1 Periodic MHD validation 21
6.2 Ohmic decay in a periodic cylinder 22
6.3 Three-dimensional Taylor-Couette flow 24
6.4 Magnetohydrodynamic Taylor-Couette flow 28
6.5 Flow induced by a helical magnetic field 30
7 Concluding remarks concerning the numerical method 33

III Magnetohydrodynamically generated velocities in confined plasma **35**

1 Introduction 35
2 Geometry and governing equations 36
3 Results and discussion 40

3.1 Generation of toroidal velocities at low viscous Lundquist number . . . 40
3.2 Simulations for higher viscous Lundquist numbers . . . 43
3.3 Influence of the safety factor on the dynamics . . . 52
3.4 Influence of the reversal of the imposed toroidal magnetic field . . 55
4 Concluding remarks about the generation of velocities in toroidal geometries 57

IV Magnetohydrodynamics for high pinch ratios in toroidal and cylindrical geometries 61
1 Introduction . . . 61
2 Toroidal simulations . . . 63
2.1 Dynamo effect and transition to a helical state . . . 65
2.2 Evolution of global quantities . . . 71
2.3 Time evolution of the different toroidal modes . . . 73
2.4 Summary of the toroidal simulations . . . 76
3 Cylindrical simulations . . . 77
3.1 Helical flows . . . 79
3.2 Evolution of global quantities . . . 83
3.3 Time evolution of the different axial modes . . . 85
4 Comparison between the results in toroidal and cylindrical geometry . . . 87
4.1 Intercomparison of the simulations . . . 87
4.2 Comparison with experimental data . . . 89
5 Concluding remarks about the toroidal and cylindrical simulations . . . 91

V Conclusion 93

A Theoretical analysis of the Hermite regularization 97
1 Analysis of a model problem . . . 97
2 Evaluation of the error . . . 100

B Imposing non homogeneous Neumann boundary conditions with a penalization method 103
1 Formulation . . . 103
2 Test case: one-dimensional instationary diffusion problem . . . 104

C Corresponding explicit scheme of the semi-implicit penalization method 107

D Calculation of the imposed poloidal magnetic field 109

E Relation of the dimensionless MHD equations to physical values from the JET tokamak **111**

F Large scale forcing of a plasma dynamo **117**

Bibliography **119**

NOTATIONS

$\boldsymbol{A}$	Vector potential
a	Small radius of the torus / Radius of the cylinder
$\boldsymbol{B}$	Magnetic field
E	Energy
$\boldsymbol{E}$	Electric field
$\boldsymbol{F}$	Force field
F	Force / Reversal parameter (RFP)
$\mathscr{F}$	Fourier transform
Ha	Hartmann number
$\boldsymbol{j}$	Current density field
$\boldsymbol{k}$	Cartesian wave vector
k_B	Boltzmann constant
$L/\mathscr{L}$	Length
m	Poloidal wave number / Mass
M	Viscous Lundquist number
n	Toroidal wave number
P	Pressure
Pr	Magnetic Prandtl number
q	Safety factor / Charge

Re	Reynolds number
S	Resistive Lundquist number
$\boldsymbol{u}$	Velocity field
U	Velocity
β	Plasma beta (ratio of the plasma pressure over the magnetic pressure)
Γ	Aspect ratio
η	Penalisation parameter
θ	Temperature
Θ	Pinch ratio (RFP)
λ	Magnetic diffusion coefficient / Mean free path
ρ	Density
σ	Electrical conductivity
τ	Reference time
μ	Magnetic permeability
ν	Kinematic viscosity
Π	Total pressure
ω	Vorticity field
∇	Nabla operator
χ	Mask function / Flux function
Ξ	Auxiliary pressure / Mask function
ζ	Radius ratio

SUBSCRIPTS

0	Imposed
k	Kinetic
mag	Magnetic
P	Poloidal
R	Direction of the big radius for the torus
r	Radius
ref	Reference
T	Toroidal direction
x	x-direction
y	y-direction
Z	Z-direction / Axial direction for the torus
z	z-direction / Axial direction for the cylinder
θ	Azimuthal direction

I

INTRODUCTION

Nuclear fusion is a possible source of energy. Indeed, it is the reaction that powers the sun. The process involves lighter elements than those used in fission reactions. Where in the latter uranium atoms are split, in fusion mainly hydrogen and its isotopes deuterium and tritium are combined to produce other particles like helium. In this process a large amount of energy becomes available. For the last 60 years actively research has been conducted to achieve controlled thermonuclear fusion on earth. Succeeding, this could bring to the planet a source of energy with almost unlimited resources, while generating only a very small amount of radioactive waste. During the past decades various devices and methods have been developed. Two different ways to obtain a controlled reaction are inertial fusion and magnetic fusion. In the former, high energy laser beams hit a target containing the fuel. The resulting shock waves compress and heat the deuterium-tritium mixture making the atoms fuse. In a magnetic fusion configuration to start the reactions very high temperatures have to be reached, of the order of $150 \cdot 10^6 K$ [35], hotter than the center of the sun. For practical reasons the pressure in a magnetic fusion reactor is far less than during a fusion reaction in the stars, and this lack of high pressure must be compensated by an important thermal agitation that increases the probabilities of having collisions fusing the particles.

The main idea behind magnetic fusion is that the very high temperature ionizes the media, forming a plasma that can be controlled, in principle, by means of a magnetic field. This is essential, because no material on earth can support the temperatures reached in a fusion reactor. The conducting fluid, or plasma, can therefore be isolated from the walls by a strong magnetic field. Different magnetic configurations have been studied for the past decades to achieve a controlled magnetic fusion reaction. Two of them, on which we will focus here, are the tokamak and the RFP (Reversed Field Pinch). These two devices have many points in common. The magnetic field is produced by external coils

and is combined with the magnetic field induced by an electric current flowing through the plasma itself. Both configurations have a toroidal shape and the imposed magnetic field that confines the plasma is helical and surrounds the toroidally shaped chamber (see Fig. 1.1).

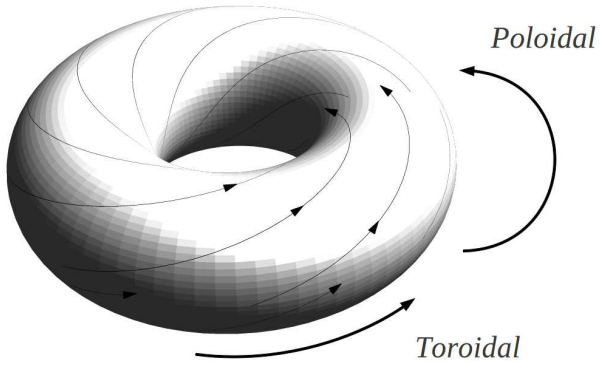

Figure 1.1: Toroidal geometry surrounded by helical magnetic field lines.

The tokamak is technologically the most advanced configuration and has a high probability to achieve a controlled nuclear reaction. In this device a strong magnetic field confines the plasma. The toroidal component of this field is usually larger than the poloidal component. The reason for this is that, in this geometry it is tried to avoid magnetohydrodynamic instabilities that develop if the ratio of toroidal over poloidal field is lower than unity. In contrast, for the RFP the poloidal and toroidal components of the magnetic field are usually of the same order of magnitude. The plasma is then unstable, and several instabilities can develop making the conducting fluid more difficult to confine.

One of the key issues to make a fusion reactor work is the ability to increase the confinement time of the plasma. In practice this is equivalent to reducing the thermal losses, which are mainly caused by turbulent fluctuations. These fluctuations degrade the quality of the confinement and thereby reduce the performance of the fusion reactor. In the tokamak configuration it was discovered three decades ago (in the ASDEX experiment) [109] that, under certain circumstances, the turbulent activity is reduced, leading to a better confinement. This improved regime is called high confinement mode (H mode) in contrast with the commonly found low confinement state (L mode). In H mode the confinement time is roughly two times bigger than in L mode. This increment might seem small but it can be of great importance for the performance of future reactors like ITER (the international experimental reactor being constructed in Cadarache, France).

In existing fusion reactors, large bulk velocities are observed [91, 90]. In particular the H mode is characterized by toroidal velocities that are several times superior to the ones measured in L-mode [94]. It is not yet well understood if these velocities are either

at the origin, or a consequence of the low-to-high confinement transition (L-H transition). Different theories have been proposed to explain the spontaneous generation of toroidal velocity, mostly based on the turbulent transport of toroidal momentum generated at the tokamak edge (e.g., in Refs. [63, 81, 28]), but no complete understanding of the phenomenon is available at present. Toroidal velocities, and the understanding of plasma velocities in general will be one of the main subjects of the present thesis.

The RFP possesses a great advantage compared to the tokamak which is the necessity of a lower magnetic field to confine the plasma, approximatively ten times smaller. The toroidal field has a weak reversal in the plasma edge, which is the reason for the name "Reversed Field Pinch". The weak RFP magnetic field yields several advantages: the use of normal magnets instead of superconductors, high mass density and the possibility of reaching thermonuclear temperatures without additional heating besides the Ohmic one [60]. The drawback of the device is the broad spectrum of magnetohydrodynamic resistive instabilities that increases the turbulence and thereby lowers the energy confinement performance. However, recently quasi-single helicity (QSH) states were observed in experiments. In these states the full turbulent regime is avoided [32]. There is a decrease of magnetic chaos and the formation of a coherent helical structure within the plasma. Further, as for the tokamak, in the RFP important velocities have been measured [86] and their origin also remains unclear.

In this thesis we will focus on the numerical study of these two magnetic fusion configurations (tokamak and RFP) using one of the simplest models describing a plasma, the magnetohydrodynamic (MHD) approximation. Far more sophisticated descriptions of fusion plasmas are at hand nowadays, such as kinetic or gyrokinetic approximations and at a detailed level these descriptions must be superior. However, it seems that at present, if one is interested in global dynamics of the full fusion plasma over timescales relevant to the bulk dynamics, MHD is the only possible description which allows to be treated numerically. With respect to previous fusion related studies our work differs in that we consider both RFP and tokamak dynamics in a fully toroidal domain taking into account nonzero viscosity and resistivity without assuming any macroscopic equilibrium. Several assumptions, such as uniform transport coefficients, isothermal, incompressible plasma dynamics, order unity magnetic Prandtl number, are obviously oversimplifications compared to reality, but they should be considered as a logical first step in understanding the basic viscoresistive MHD behavior, in toroidal geometry, while retaining the freedom to easily change the precise shape of the domain.

In order to allow an efficient computation of the full viscoresistive MHD equations, we use a Fourier pseudo-spectral method. To take into account boundary conditions we have implemented and validated a volume penalisation technique originally developed for hydrodynamics [1]. The large advantage of this method is the flexibility on the considered geometry and the ease of implementation. This flexibility facilitates the comparison of different geometries and the assessment of the boundary effects on the dynamics of the considered physical systems. The strength of the combination of a Fourier pseudo-spectral solver with the penalization method is that the numerical code uses fast Fourier

transforms, that can be easy parallelized, and at the same time a large variety of relatively complex geometries can be taken into account.

In Chap. II we present the MHD equations and detail the numerical algorithm. The penalization method is described and several validation test-cases are exposed. Different implementations of the penalization technique are compared and the order of convergence of the numerical method is presented. We consider two- and three-dimensional test-cases for hydrodynamic and magnetohydrodynamic systems[†].

In Chap. III the study of the magnetohydrodynamic flows generated in toroidal geometries is presented. The magnetic configuration (as measured by the safety factor) is here close to that of the tokamak device. Two different toroidal geometries, one with a symmetric and the other with an asymmetric cross section are compared. The diffusivity of the system is varied and a transition in the flow topology is observed. The differences resulting of the change in the geometry are highlighted as well as the influence of the change of the ratio of the toroidal over the poloidal imposed magnetic field. In particular we present a mechanism which explains the spontaneous generation of toroidal angular momentum, which is also observed in existing tokamaks. The mechanism we observe seems to be generic since it is present even in the coarsest description of a fusion plasma: viscoresistive magnetohydrodynamics[§].

In Chap. IV the toroidal dynamics are presented for a magnetic configuration close to a RFP reactor. The transition from a calm axisymmetric state to a fluctuating helical state are presented for a toroidal and for a cylindrical geometry. The differences in the bulk velocities and other features of the plasma dynamics of these two configurations are stressed. Finally the numerical results are compared to experimental RFP data.

Most of the more technical details are given in the appendices. The dimensionless quantities, that should be introduced in the MHD simulations to reproduce the physical values of a tokamak like JET, are shortly discussed in Appendix E. Also, in Appendix F can we find a short report on preliminary simulations of a plasma dynamo experiment.

[†]This chapter is an adapted version of the manuscript [75], reporting on the investigation carried out in collaboration with Matthieu Leroy and Kai Schneider in Marseille.

[§]Chap. III is an adaptation of a manuscript [74], which was written in collaboration with Kai Schneider and David C. Montgomery.

II

NUMERICAL METHOD AND VALIDATION

1 INTRODUCTION

Magnetohydrodynamics is the discipline that studies the interaction between conducting fluids and magnetic fields. Depending on the topology and the intensity of the magnetic field, as well as on the values of the kinematic viscosity and the magnetic diffusivity, numerous different flow behaviors can be observed. As a function of the viscosity the flows can vary from a laminar to a highly turbulent state and the magnetic diffusivity allows to change the dynamics from a highly diffusive transport to an almost frozen-in advection of the magnetic field. Therefore, in the turbulent state, even in the statistically homogeneous case, a large range of dynamically active scales can be observed. Most of the interesting applications of MHD are however not statistically homogeneous due to the presence of solid walls. Examples are the planetary dynamo mechanism, magnetically confined fusion plasmas and industrial applications involving liquid metals [27, 103]. In order to study these phenomena, either experiments need to be carried out, or a set of nonlinear differential equations must be solved, combined with adequately chosen boundary conditions. In most cases, these equations cannot be solved analytically, so that numerical integration is needed in order to describe the dynamics. A wide range of MHD solvers have been developed over the last decades and an exhaustive listing is beyond the scope of this chapter. Nevertheless we will mention several approaches which are used to compute MHD in wall-bounded geometry. MHD codes applied to tokamak geometry are proposed in [58, 42] and to Reversed Field Pinch geometry in [24]. A more complete review of MHD solvers developed to compute fusion-plasma-related flows is given in [46]. Solvers aiming at a description of the dynamo effect are, for example, given in [38, 45, 89] and computations investigating the magnetorotational instability in bounded domain were reported by Rüdiger and Shalybkov [95], Gissinger *et al.* [36] and Willis and Barenghi

[110]. An early numerical approach to study MHD in cylindrical geometry was proposed and validated by Shan *et al.* [102] and more recently applied to spherical geometry by Mininni *et al.* [64]. Most of these solvers are adapted to either a single geometry or a particular application. To change the geometry substantial effort must be invested to adapt the numerical mesh or to change the basis functions used in the numerical algorithm.

We present in this chapter the implementation and validation of the volume penalization method applied to magnetohydrodynamics. The strength of this approach is the high flexibility in the geometry and the ease of implementation. The volume penalization method is an immersed boundary method [82], in which both the fluid region and the confining boundaries are part of the same computational domain. The influence of the boundaries is then modeled by adding a force or drag term to the dynamical equations in the part of the domain in which the boundaries are to be present. In the volume-penalization method, for the hydrodynamic case, the solid bodies are modeled as porous media whose permeability tends to zero. This so called Navier–Stokes/Brinkman model, where the penalization source term in the momentum equation corresponds to the Darcy drag, was first proposed by Arquis and Caltagirone [3] in the context of the natural convection flow inside a cavity with porous walls. It was then generalized to study fluid - porous wall - solid boundary systems [2]. In addition to being physically motivated, this model is mathematically justified, since Angot *et al.* [1] rigorously proved that the method converges to the Navier–Stokes equations combined with no-slip boundaries, when the porosity in the part of the domain corresponding to the boundaries is taken infinitesimally small. A first use of the method in combination with a pseudo-spectral Navier–Stokes solver was reported in [98]. An extensive validation of the method for three dimensional fixed and moving boundaries is reported in [52].

The strength of the combination of a pseudo-spectral Navier–Stokes solver with the penalization method is the compromise between accuracy and ease of implementation while retaining a great flexibility in the choice of the geometry of the boundaries. The method has been used to study two-dimensional MHD [11, 76, 12] which allowed to compare square, circular and periodic boundaries using the same Cartesian grid and numerical method. In the present chapter we will present a detailed validation of the method for two- and three-dimensional confined hydrodynamic and MHD flows.

The chapter is organized as follows. In section 2 – 3, we expose the physical model and its numerical discretization. Section 4 assesses the parallel performance of our implementation. As a first validation, section 5 presents two-dimensional kinematic and magnetic test cases together with a comparison to analytical results. Validation of the three-dimensional periodic MHD calculations is exposed in section 6.1. Subsequently Ohmic decay is considered in section 6.2. Sections 6.3 and 6.4 compare our three-dimensional results for 3D Taylor-Couette hydrodynamic and MHD flows with those available in the literature, as further validation. Section 6.5 reports on the flow induced in a conducting fluid by the presence of an imposed helical magnetic field.

2 MHD EQUATIONS

The media we study are isothermal, incompressible and we consider constant permeability μ, permittivity ε and conductivity σ of the material. The MHD equations for this case are the Navier–Stokes equation (including the Lorentz force) and the induction equation (that combines Ohm's law, Faraday's equation and Ampère's law). Introducing conventional normalization of the velocity by the Alfvén velocity $C_a = B_0/\sqrt{\rho\mu}$, a reference magnetic field B_0 and a conveniently chosen lengthscale L, the normalized equations read,

$$\frac{\partial \boldsymbol{u}}{\partial t} - \nu\nabla^2\boldsymbol{u} = -\nabla\Pi + \boldsymbol{u}\times\boldsymbol{\omega} + \boldsymbol{j}\times\boldsymbol{B}, \tag{2.1}$$

and

$$\frac{\partial \boldsymbol{B}}{\partial t} - \lambda\nabla^2\boldsymbol{B} = \nabla\times[\boldsymbol{u}\times\boldsymbol{B}], \tag{2.2}$$

where ν is the dimensionless kinematic viscosity (inverse of the Reynolds number), λ the dimensionless magnetic diffusivity (inverse of the magnetic Reynolds number) and $\rho = 1$ is the density. The vorticity $\boldsymbol{\omega}$ and current density $\boldsymbol{j}$ are given by

$$\boldsymbol{\omega} = \nabla\times\boldsymbol{u} \tag{2.3}$$

$$\boldsymbol{j} = \nabla\times\boldsymbol{B}, \tag{2.4}$$

and $\Pi = P + \frac{1}{2}\boldsymbol{u}^2$ is the modified pressure. The velocity field $\boldsymbol{u}$ is considered incompressible and the magnetic field $\boldsymbol{B}$ divergence free,

$$\nabla\cdot\boldsymbol{u} = 0, \tag{2.5}$$

$$\nabla\cdot\boldsymbol{B} = 0. \tag{2.6}$$

To complete the problem one needs to specify the initial and the boundary conditions corresponding to the physical system that we are interested in. In particular the boundary conditions will be discussed in more detail in the rest of this chapter.

3 THE NUMERICAL CODE

The penalization method was introduced into two independently developed pseudo spectral MHD solvers, the L-code from Lyon and the M-code from Marseille. The cross-check of the results obtained by the two codes allowed a careful debugging and implementation of the method.

3.1 PSEUDO-SPECTRAL DISCRETIZATION

A classical Fourier pseudo-spectral method is used for the spatial discretization of a cubic periodic domain Ω of size 2π [17]. The physical size of the domain can be modified

rescaling the box by multiplying by L_x, L_y and L_z. Spatial derivatives are evaluated in Fourier space and multiplications are computed in physical space. In the following we denote the Fourier Transform by the symbol $\hat{}$ or $\mathscr{F}\{\ \}$. All fields are represented as truncated Fourier series and here we show this representation explicitly for the velocity:

$$\boldsymbol{u}(\boldsymbol{x},t) = \sum_{k_x=-N_x/2}^{N_x/2-1} \sum_{k_y=-N_y/2}^{N_y/2-1} \sum_{k_z=-N_z/2}^{N_z/2-1} \widehat{\boldsymbol{u}}(\boldsymbol{k},t) e^{i\boldsymbol{k}\cdot\boldsymbol{x}}, \tag{2.7}$$

$$\widehat{\boldsymbol{u}}(\boldsymbol{k},t) = \frac{8\pi^3}{N_x N_y N_z} \sum_{n_x=0}^{N_x-1} \sum_{n_y=0}^{N_y-1} \sum_{n_z=0}^{N_z-1} \boldsymbol{u}(\boldsymbol{x}_\mathbf{n},t) e^{-i\boldsymbol{k}\cdot\boldsymbol{x}_\mathbf{n}}, \tag{2.8}$$

with the wave vector $\boldsymbol{k} = (k_x, k_y, k_z)$ where $-N_x/2 \leq k_x \leq N_x/2-1, -N_y/2 \leq k_y \leq N_y/2-1, -N_z/2 \leq k_z \leq N_z/2-1$, $\boldsymbol{x}_\mathbf{n} = (n_x 2\pi/N_x, n_y 2\pi/N_y, n_z 2\pi/N_z) \in [0,2\pi]^3$ with $n_x = 0$, ..., $N_x-1, n_y = 0, ..., N_y-1, n_z = 0, ..., N_z-1$. The number of grid points in x, y and z-direction, N_x, N_y and N_z, respectively, can be adapted to obtain the accuracy needed in the different directions. To avoid aliasing errors, *i.e.*, the production of small scales due to nonlinear terms which are not resolved on the grid, the velocity and magnetic fields are dealiased at each time step by truncating its Fourier coefficients using the 2/3 rule [17]. For the transformation between physical and Fourier space two different Fourier transforms were used in the two codes, firstly the P3DFFT routine, based on the FFTW library, secondly the JMFFT library. Both Fourier Transforms have an order of complexity of $N \log_2 N$ with $N = N_x N_y N_z$.

The pressure term can be eliminated from the equations in spectral space by using the incompressibility condition of the medium. This introduces the projector $P_{ij} = \delta_{ij} - k_i k_j / k^2$ in front of the nonlinear term. The Eqs. (2.1) and (2.2) in spectral space are then written:

$$\frac{\partial \hat{u}_i}{\partial t} + \nu k^2 \hat{u}_i = P_{ij} \left\{ \left(\widehat{\boldsymbol{u} \times \boldsymbol{\omega}} + \widehat{\boldsymbol{j} \times \boldsymbol{B}} \right)_j \right\}, \tag{2.9}$$

$$\frac{\partial \hat{B}_i}{\partial t} + \lambda k^2 \hat{B}_i = \left[i\boldsymbol{k} \times (\widehat{\boldsymbol{u} \times \boldsymbol{B}}) \right]_i, \tag{2.10}$$

where $k^2 = |\boldsymbol{k}^2|$.

3.2 PENALIZATION METHOD

The volume penalization method is based on the idea of modeling solid bodies as porous media whose permeability tends to zero. The flow is considered in a domain in which both fluid and solid domains are embedded. The difference between the fluid and solid subdomain is the permeability. In the fluid domain the permeability is infinite and in the solid domain the permeability tends to zero. The method allows to consider an arbitrary

shape and number of obstacles. The equations are modified by adding the penalization term:

$$\frac{\partial \boldsymbol{u}}{\partial t} = \boldsymbol{u}\times\boldsymbol{\omega} - \nabla\Pi + \nu\nabla^2\boldsymbol{u} + \boldsymbol{j}\times\boldsymbol{B} - \frac{\chi}{\eta}(\boldsymbol{u}-\boldsymbol{u}_{wall}) \tag{2.11}$$

$$\frac{\partial \boldsymbol{B}}{\partial t} = \nabla\times(\boldsymbol{u}\times\boldsymbol{B}) + \lambda\nabla^2\boldsymbol{B} - \frac{\chi}{\eta}(\boldsymbol{B}-\boldsymbol{B}_{wall}), \tag{2.12}$$

with $\boldsymbol{u}_{wall}$ and $\boldsymbol{B}_{wall}$ the imposed values of the velocity and magnetic field in the solid domain and η is the permeability of the solid domain, *i.e.*, the penalization parameter, which could be different for each equation, and $\chi(\boldsymbol{x},t)$ the mask function (see Fig. 2.1):

$$\chi(\boldsymbol{x},t) = \begin{cases} 0 & \text{for } \boldsymbol{x}\in\Omega_f, \text{the fluid domain} \\ 1 & \text{for } \boldsymbol{x}\in\Omega_s, \text{the solid domain.} \end{cases} \tag{2.13}$$

Note that $\boldsymbol{B}_{wall}$ can be freely chosen, we are not obliged to penalize all components. For instance choosing $\boldsymbol{B}_{wall} = \boldsymbol{B}_{\parallel}$ with $\boldsymbol{B}_{\parallel}$ the component of $\boldsymbol{B}$ parallel to the wall, only penalizes the normal component and leaves the parallel component free. According to Eqs. (2.11) and (2.12), the flow is governed by the Navier–Stokes and induction equations in Ω_f, and by Darcy's law in Ω_s for small η. As mentioned in the introduction, the convergence of the velocity of the penalized equation in the limit of vanishing η to the solution given by the Navier–Stokes equations with no-slip boundary conditions was rigorously proven by Angot *et al.* [1] for fixed obstacles. The estimates were then refined by Carbou and Fabrie [22], who demonstrated that the solution of the penalized equations converges in the L_2-norm with $\sqrt{\eta}$ towards the solution of the non-penalized equations with Dirichlet boundary conditions. Similar results are anticipated for the induction equation.

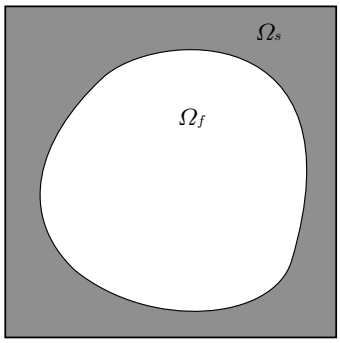

Figure 2.1: The computational domain Ω contains both the fluid domain Ω_f and the solid domain Ω_s.

To use a pseudo-spectral solver we need to Fourier-transform Eqs. (2.11) and (2.12) and we obtain

$$\frac{\partial \hat{u}_i}{\partial t} + \nu k^2 \hat{u}_i = P_{ij}\left\{\left[\widehat{\boldsymbol{u}\times\boldsymbol{\omega}} + \widehat{\boldsymbol{j}\times\boldsymbol{B}} - \mathscr{F}\left\{\frac{\chi}{\eta}(\boldsymbol{u}-\boldsymbol{u}_{wall})\right\}\right]_j\right\}. \tag{2.14}$$

We stress here that the Riesz projector P_{ij} is also applied to the penalization term. Indeed, this form straightforwardly appears in the Fourier-transformed equations when the pressure is eliminated by solving a Laplace equation. The fact that the projector also acts on the penalization term is important to ensure incompressibility, since the penalization term is not necessarily divergence free at the fluid-solid boundary. This is also the case for the magnetic field. Due to the penalization term, the magnetic field is no longer divergence free. One way to cure this is to add an auxiliary pressure to the magnetic field

$$\frac{\partial \boldsymbol{B}}{\partial t} - \lambda \nabla^2 \boldsymbol{B} = \nabla \times [\boldsymbol{u} \times \boldsymbol{B}] \underbrace{-\nabla \Xi}_{\substack{\text{Auxiliary} \\ \text{pressure}}} \underbrace{-\frac{\chi}{\eta}(\boldsymbol{B} - \boldsymbol{B}_{wall})}_{\text{Penalization term}}. \tag{2.15}$$

In the absence of boundaries in the domain, this pressure gradient would be equal to zero, as can be directly seen by solving a Laplace equation for Ξ and using the solenoidality constraint, Eq. (2.6). Indeed the (curl)-term $i\boldsymbol{k} \times \widehat{(\boldsymbol{u} \times \boldsymbol{B})}$ is necessarily divergence free. Eliminating the pressure from Eq. (2.15), we find for the Fourier-transformed equation for the magnetic field,

$$\frac{\partial \hat{B}_i}{\partial t} + \lambda k^2 \hat{B}_i = P_{ij} \left\{ \left[i\boldsymbol{k} \times \widehat{(\boldsymbol{u} \times \boldsymbol{B})} - \mathscr{F} \left\{ \frac{\chi}{\eta} (\boldsymbol{B} - \boldsymbol{B}_{wall}) \right\} \right]_j \right\}, \tag{2.16}$$

which guarantees the incompressibility.

The penalization method allows for a simple implementation of complex geometries, since to change the shape of the walls, one only needs to redefine the mask function. This is a huge advantage, because almost no effort is required to modify the shape of the flow geometry during an investigation and arbitrarily complex shapes can be considered. Several limitations should however be mentioned. First, the dynamical equations are solved in both the fluid domain and the penalized domain, so that, if the penalized domain is large, an important part of the numerical resources is used to compute the dynamically unimportant flow inside the walls (see for example section 6.4). Second, here no mesh refinement near the wall is used, so that, to capture small scale dynamics near boundaries, one needs to globally increase the resolution. Third, the boundary conditions imposed by the numerical method need to be satisfied in the computational domain. Let us explain this latter point in more detail.

Intrinsically, the boundary conditions of the Fourier pseudo-spectral solver are periodic in the three directions. Thus in the computational domain this periodicity must be satisfied. This imposes certain constraints on the geometries and especially on the boundary conditions that can be considered. If in the geometry sketched in Fig. 2.1 the solid domain corresponds to no-slip walls, *i.e.* $\boldsymbol{u}_{wall} = 0$, the periodicity condition is met automatically. However, if the outer-walls are chosen to move in solid-body rotation anti-clockwise, the left border of the domain will move downwards whereas the right border will move upwards. In that case the periodicity condition is not satisfied. A solution to this problem is to add a third, unpenalized, subdomain outside the walls which will allow

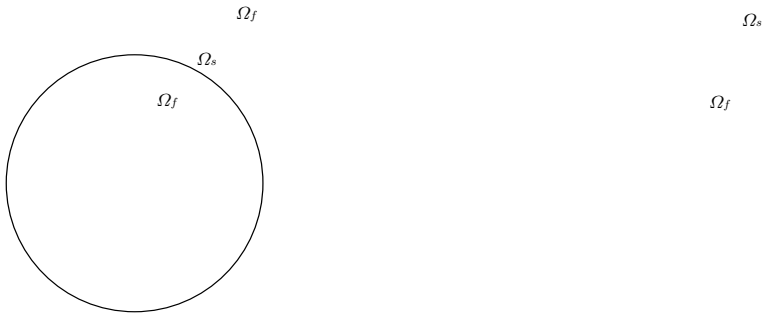

Figure 2.2: Leaving a part of the domain unpenalized at the edges of the computational domain allows to use inhomogeneous Dirichlet conditions at the fluid solid interface, without violating the periodicity condition at the edge of the domain (left). Another option is to interpolate the imposed velocity to a zero value with a horizontal tangent at the domain frontier with an interpolating Hermite polynomial. The velocity field in the whole computational region belongs then to the C^1 class (right).

to respect the periodic boundary conditions of the computational domain. This solution is sketched in Fig. 2.2 (left). However it has an inconvenience which we will describe below.

Discontinuities in the velocity field, or in its gradients, are a source of Gibbs oscillations. These oscillations are an unavoidable feature in the present approach, and as long as their amplitude is small compared to physical effects, they do not constitute a serious problem in most cases. When discontinuities become strong, the Gibbs-oscillations also increase in size. Considering Fig. 2.2 (left), it is clear that if the solid domain turns and the outer fluid domain is very small, the velocity gradient becomes strong in the outer fluid domain and the discontinuity of the velocity gradient will become large on the interface between Ω_s and the outer Ω_f. Gibbs oscillations might get strong in this case. One solution is the following: instead of imposing in Ω_s a solid body rotation, we impose a velocity profile which gives the correct boundary condition at the solid-fluid interface, and which smoothly tends to zero towards the edges of the computational domain Fig. 2.2 (right). The latter solution is slightly more complicated since an interpolation needs to be computed, using a Hermite's interpolating polynomial for instance. Its advantage is that the continuity of the solution and its derivatives between the boundary value and zero value can be imposed in a smooth way, which yields an improved order of convergence of the algorithm, as we will see in section 5 (an analytical analysis can be found in Appendix A).

Another drawback of the penalization method is that it is not yet possible to impose inhomogeneous Neumann conditions at the boundaries using a Fourier spectral code. In Appendix B a one-dimensional penalization method for taking into account

non-homogeneous Neumann boundary conditions is presented. The lack of a three-dimensional implementation makes it not yet possible to impose arbitrary values of the velocity gradient or magnetic gradient, for example, to impose the vorticity and the current density at the walls. This would in particular be important to model the influence of solid boundaries with arbitrary magnetic properties on the magnetic field generated in the fluid. A recent investigation by Kadoch *et al.* [49] presents a technique for implementing homogeneous Neumann conditions using the penalization method with a spectral method. The extension to three-dimensional inhomogeneous Neumann conditions is an important perspective for further research.

3.3 TIME-DISCRETIZATION

Two different implementations of the penalization method in the time-advancing scheme will be compared. The first is explicit and constrains the penalization parameter η to be bigger than the time step Δt to avoid numerical instabilities. The second is a semi-implicit implementation that allows the penalization parameter to be independent of the time step. Second and third order time schemes are used. In all approaches an exact integration of the viscous and magnetic diffusion term is used. In the following two sections these different methods are detailed.

EXPLICIT IMPLEMENTATION OF THE PENALIZATION TERM

In this section we detail the time integration of the equations using an explicit treatment of the nonlinear and penalization terms. It must be noted that along with its simplicity and robustness this approach has a drawback: the explicit treatment of the penalization term imposes a stability condition, in addition to the usual CFL condition. An analytical analysis of the magnetic part of the method has yet to be done to check if it adds another stability condition. Up to now no problem occurred if the same stability criterions were used for the velocity and the magnetic field.

The basic time-stepping schemes that are implemented are an adaptive second and third order Adams-Bashforth method (denoted by AB2 and AB3 respectively). The use of these schemes fits well into our general concept of compromise between the ease of implementation and computational efficiency. Exact integration of the diffusion term is feasible because the Laplace operator is diagonal in Fourier space and hence no linear system has to be solved. It improves stability of the scheme, avoiding the stability condition $\Delta t < \Delta x^2/\nu$. The remaining terms are discretized explicitly to avoid the solution of nonlinear equations, however it implies a CFL condition on the time step size Δt and also a condition due to the explicit discretization of the penalization term , *i.e.,* $\Delta t < \eta$ for AB2 and $\Delta t < \frac{6}{11}\eta$ for AB3, as linear stability analysis shows [52].

For illustration, the equations will be given for the case of the velocity only. The discretization of the magnetic field is handled analogously, the only difference is the exact

form of the nonlinear and penalization terms. First the Navier–Stokes equation is rewritten in the form of a nonlinear evolution equation and transformed into Fourier space,

$$\partial_t \boldsymbol{u} - \nu\nabla^2\boldsymbol{u} = N(\boldsymbol{u}) \tag{2.17}$$

$$\partial_t \widehat{\boldsymbol{u}} + \nu k^2 \widehat{\boldsymbol{u}} = \widehat{N}(\widehat{\boldsymbol{u}}). \tag{2.18}$$

For the initial condition $\widehat{\boldsymbol{u}}(\boldsymbol{k}, t_n)$, the above equation has the following solution

$$\widehat{\boldsymbol{u}}(\boldsymbol{k}, t_{n+1}) \;=\; e^{-\nu\Delta t_{n+1}k^2}\widehat{\boldsymbol{u}}(\boldsymbol{k}, t_n) + \int_{t_n}^{t_{n+1}} e^{-\nu(t_{n+1}-s)k^2}\widehat{N}\left(\widehat{\boldsymbol{u}}(\boldsymbol{k}, s)\right) ds, \tag{2.19}$$

which can be discretized

$$\begin{aligned}
\text{AB2} \quad \longrightarrow \quad \widehat{\boldsymbol{u}}(\boldsymbol{k}, \mathrm{t_{n+1}}) =& e^{-\nu\Delta t_{n+1}k^2}\left(\widehat{\boldsymbol{u}}(\boldsymbol{k}, t_n) + \beta_{10}\widehat{N}^n + \beta_{11}e^{-\nu\Delta t_n k^2}\widehat{N}^{n-1}\right) \\
\text{AB3} \quad \longrightarrow \quad \widehat{\boldsymbol{u}}(\boldsymbol{k}, \mathrm{t_{n+1}}) =& e^{-\nu\Delta t_{n+1}k^2}\left(\widehat{\boldsymbol{u}}(\boldsymbol{k}, t_n) + \beta_{20}\widehat{N}^n\right. \\
&\left. + e^{-\nu\Delta t_n k^2}\left(\beta_{21}\widehat{N}^{n-1} + \beta_{22}e^{-\nu\Delta t_{n-1}k^2}\widehat{N}^{n-2}\right)\right),
\end{aligned} \tag{2.20}$$

with $\widehat{N}^n$ denoting the value of the nonlinear term at the time instant t_n, the second order Adams-Bashforth coefficients

$$\begin{aligned}
\beta_{10} &= \frac{1}{2}\frac{\Delta t_{n+1}}{\Delta t_n}\left(\Delta t_{n+1} + 2\Delta t_n\right) \\
\beta_{11} &= -\frac{1}{2}\frac{\Delta t_{n+1}^2}{\Delta t_n},
\end{aligned} \tag{2.21}$$

and the third order Adams-Bashforth coefficients

$$\begin{aligned}
\beta_{20} &= \frac{\Delta t_{n+1}(2\Delta t_{n+1}^2 + 6\Delta t_n\Delta t_{n+1} + 3\Delta t_{n-1}\Delta t_{n+1} + 6\Delta t_n^2 + 6\Delta t_{n-1}\Delta t_n)}{6\Delta t_n(\Delta t_n + \Delta t_{n-1})} \\
\beta_{21} &= \frac{-\Delta t_{n+1}^2(2\Delta t_{n+1} + 3\Delta t_n + 3\Delta t_{n-1})}{6\Delta t_{n-1}\Delta t_n} \\
\beta_{22} &= \frac{\Delta t_{n+1}^2(2\Delta t_{n+1} + 3\Delta t_n)}{6\Delta t_{n-1}(\Delta t_n + \Delta t_{n-1})},
\end{aligned} \tag{2.22}$$

where $\Delta t_n = t_n - t_{n-1}$ [98]. For start-up a first order scheme is used, as two time steps are required to start a second-order scheme. Similarly a first order and a second order scheme are used to start the third order scheme.

The time step size control is based on the CFL stability limit of the explicit discretization of the nonlinear term, with addition of the stability criterion due to the penalization. Therefore, at each time step t_n, the maximal point-wise velocity is computed and the new time step is given by $\Delta t_{n+1} = C\Delta x/U_{max}$ where $C < 1$ is the CFL constant and Δx is the minimal spatial grid size. Moreover, the time step has to verify the condition $\Delta t_{n+1} < \eta$ (AB2) or $\Delta t_{n+1} < \frac{6}{11}\eta$ (AB3) due to the presence of the penalization term. The same method is applied to the magnetic field and the time step is chosen to be small enough to verify the stability criteria of both the magnetic field and velocity field discretization.

SEMI-IMPLICIT IMPLEMENTATION

As noted in the previous section, the stability condition for a third order time scheme constrains $\Delta t < \frac{6}{11}\eta$. To avoid this limitation, an implicit implementation was introduced by Kolomenskiy and Schneider [52] for Burgers' equation and extended to Navier–Stokes' equation by Jause-Labert *et al.* [47]. In this case the penalization term is evaluated at the time step t_{n+1}. The penalization is thus no longer treated together with the nonlinear term. The diffusion term, as in the explicit method, is exactly integrated.

This method is more time-expensive because two additional Fourier transforms are required. In addition to the projection of the nonlinear term, a second projection is realized (that includes the penalization term at t_{n+1}) to ensure the solenoidal nature of the two considered fields. The fact that the time step can be adaptive (taking into account the CFL condition) makes this technique more suitable for unsteady simulations. The penalization term is introduced using a first order time scheme, which does not influence negatively the precision as long as boundaries are fixed.

The magnetic equations being handled analogously we present the new time scheme for the velocity field

$$\hat{u}_i(\boldsymbol{k}, t_{n+1}) = P_{ij}\left\{\mathscr{F}\left[\frac{\mathscr{F}^{-1}\{\mathscr{Q}_i^n\} + \frac{\Delta t}{\eta}\chi\, u_{wall_i}(\boldsymbol{x}, t_{n+1})}{1+\frac{\Delta t}{\eta}\chi}\right]_j\right\}. \tag{2.23}$$

The third order Adam-Bashforth scheme is retained for the nonlinear terms in this formulation

$$\mathscr{Q}_i^n = e^{-\nu\Delta t_{n+1}k^2}\left(\widehat{\boldsymbol{u}}(\boldsymbol{k}, t_n) + \beta_{20}\widehat{N}^n + e^{-\nu\Delta t_n k^2}\left(\beta_{21}\widehat{N}^{n-1} + \beta_{22}e^{-\nu\Delta t_{n-1}k^2}\widehat{N}^{n-2}\right)\right). \tag{2.24}$$

This numerical scheme for a penalization parameter η sufficiently small ($\eta << \Delta t$) converges towards an explicit modified scheme where the time step Δt replaces the penalization parameter η and where the nonlinear term vanishes in the solid region. We therefore call this method *semi-implicit*. This is further explained in Appendix C. For this case with very small penalization parameter, the permeability of the solid media is given by the value of the time step. The asymptotic convergence of the porous boundaries towards a solid wall, if η is sufficiently small, is in that case limited by the value $\eta_{\text{effective}} \approx \Delta t$.

4 PARALLEL PERFORMANCES

The numerical code is parallelized using MPI libraries. The parallelization performances are evaluated on the calculator *Vargas* of the French high performance computing center IDRIS. The performances are estimated for a hydrodynamic and MHD calculation for three different grid resolutions. The test cases used are a three-dimensional Taylor-Couette flow for the hydrodynamic calculation (see section 6.3) and a MHD Taylor-Couette for the MHD calculation (see section 6.4). The comparison is made to ensure

that the extra MPI exchanges and cache memory effects of the MHD calculations do not produce important slowdowns.

We find that the MHD calculation is roughly twice as long as the hydrodynamic one. This is expected as we use for a MHD run the double number of fast Fourier transforms at each iteration. Note that per iteration, using a semi-implicit implementation of the penalization term, we need 12 Fourier transforms for each vector field. The results are shown in table 2.1 and in Fig. 2.3.

Processors		4	8	16	32	64	128
Time per iteration per proc	Hydro	1.06	0.61	0.47	0.35	–	–
resolution 128^3 (s)	MHD	2.06	1.26	0.76	0.62	–	–
Time per iteration per proc	Hydro	10.01	5.11	2.97	1.80	1.21	–
resolution 256^3 (s)	MHD	19.96	10.06	6.05	3.45	2.41	–
Time per iteration per proc	Hydro	–	–	–	18.61	11.68	8.20
resolution 512^3 (s)	MHD	–	–	–	37.11	22.53	15.10

Table 2.1: Parallel performances of the numerical code.

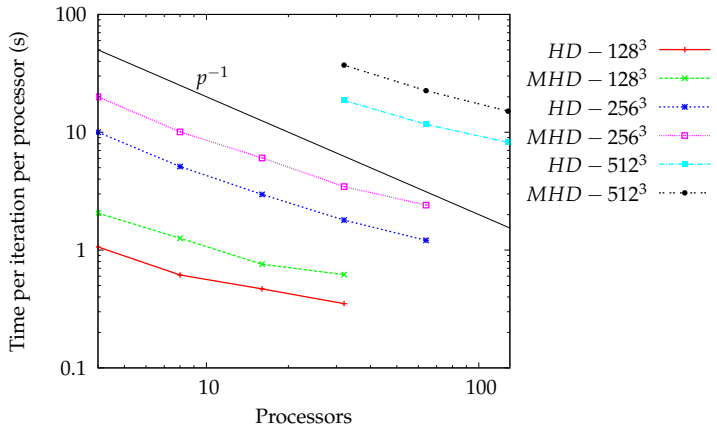

Figure 2.3: Code scaling in the calculator *Vargas* of IDRIS for hydrodynamic and MHD calculations.

The time per iteration per processor scales with the number of processors following an approximate power-law dependence close to the ideal scaling law, 1/(*number of processors*).

5 TWO-DIMENSIONAL VALIDATION

In this section we present a purely hydrodynamic test-case, the two-dimensional Taylor-Couette flow and a purely magnetic test-case, the z-pinch configuration. For both cases

analytical solutions are known, which allows a careful convergence study and which allows to check different ways to introduce the boundary conditions.

5.1 TWO-DIMENSIONAL TAYLOR-COUETTE FLOW

We consider the classical two-dimensional hydrodynamic problem of a flow between two coaxial rotating cylinders (*e.g.*, Taylor [104]). The inner cylinder rotates at constant speed, while the outer cylinder is kept at rest. The steady flow solution of the problem is

$$U_\theta(r) = \frac{\Omega_2 R_2^2 - \Omega_1 R_1^2}{R_2^2 - R_1^2} r + \frac{(\Omega_1 - \Omega_2) R_1^2 R_2^2}{R_2^2 - R_1^2} \frac{1}{r}, \tag{2.25}$$

where $\Omega_{(1,2)}$ are the angular velocities of the cylinders, $R_{(1,2)}$ the radii of the cylinders and r the cylindrical coordinate (see Fig. 2.4).

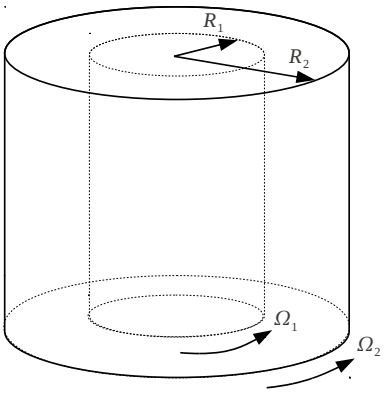

Figure 2.4: Taylor-Couette flow configuration.

The relative L_2 error in the fluid domain $||f_{numerical} - f_{analytical}||_{L_2} / ||f_{analytical}||_{L_2}$ with f being the considered field, is calculated for different penalization parameters η and number of grid points N (64, 128, 256, 512), in one direction with $N = N_x = N_y$ and $N_z = 4$.

As mentioned above, the present calculation is entirely hydrodynamic. The simulations are carried out until a steady state is obtained, so that the error is independent of the time discretization. A cubic domain with size-length 2π is considered, the time step is fixed to a value $\Delta t = 5.10^{-5}$ and the kinematic viscosity $\nu = 1$. The radii R_1, R_2 are $(0.32\pi, 0.82\pi)$ respectively. At $t = 0$ the fluid domain is at rest and the inner-cylinder is set into movement with a fixed velocity $U_\theta(R_1) = 1$ while the velocity $U_\theta(R_2)$ is kept equal to zero. The runs are stopped when the time $t_{max} = 5$ is reached. At this time instant, the difference in the kinetic energy between two iterations is less than 10^{-9} (for a kinetic energy of order unity), which indicates that a steady state is satisfactorily achieved.

The velocity profile imposed in the mask is chosen in two different ways, corresponding to the discussion in section 3.2. In the first case, the velocity in the inner cylinder is

straightforwardly set to a solid-body rotation, $U_\theta = \Omega_1 r$, in the inner cylinder and $U_\theta = 0$ in the outer cylinder. This is the most obvious choice. The component U_r is set to zero at the boundaries. The velocity field is hereby continuous, but there exists a discontinuity of the velocity field derivative at the fluid boundaries (which is also the case in the real, physical situation). The error evolution with the penalization parameter and the convergence of the error with the resolution are shown in Figs. 2.5 and 2.6. For these calculations the expected $\sqrt{\eta}$ convergence order [22] is found and the convergence is second order in space as a function of the resolution N, confirming the results in [52]. We also observe a saturation of the error for large N, corresponding to the penalization error.

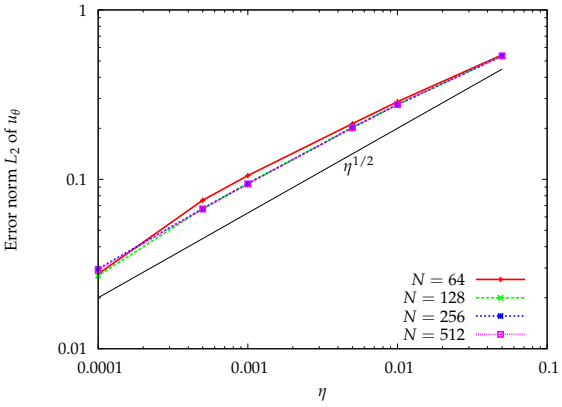

Figure 2.5: Taylor-Couette: convergence of the relative L_2 error of u_θ with the penalization parameter η, convergence order $\sqrt{\eta}$.

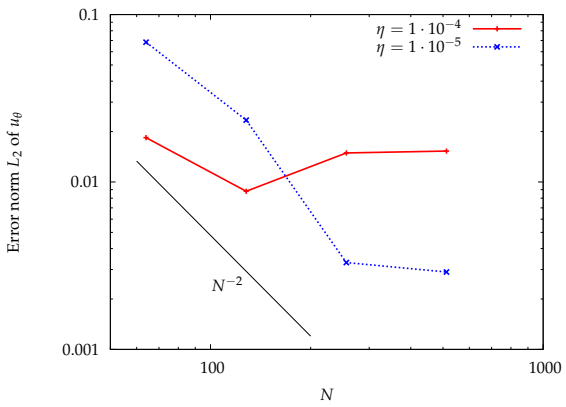

Figure 2.6: Taylor-Couette: convergence of the relative L_2 error of u_θ with the resolution N which shows a second order convergence.

A second way to impose the velocity in the mask will now be described. In this particular test-case the analytical solution is known (Eq. (2.25)) and we can use this information to increase the precision of the method. As mentioned in section 3.2, Gibbs oscillations are created due to discontinuities in the fluid variables or their derivatives. The discontinuity in the velocity gradient field can here be removed by using a 4^{th} order Hermite interpolation at the boundaries at $r = R_1, R_2$. Any purely azimuthal, axisymmetric flow is solenoidal so we can freely choose the velocity $U_\theta(r)$ in the mask, as long as it respects the correct boundary conditions at $r = R_1$, $r = R_2$ and $r = \pi$, the latter condition being imposed by the periodicity of the pseudo-spectral method. The velocity $U_\theta(r)$ in the mask is chosen such that velocity and derivative at the fluid-solid boundaries are continuous. Subsequently the velocity field is interpolated to decay smoothly from the analytical solution at $r = R_1, R_2$ to zero at $r = 0$ and $r = \pi$ respectively, using an interpolating Hermite polynomial. Any discontinuity on the derivative of the velocity field at the fluid boundaries is thus avoided and the Gibbs oscillations are hereby significantly reduced. In principle even higher order velocity derivatives could be smoothed in this way using higher order Hermite interpolation. Note that a similar regularization is used in [54] for the velocity field, where the imposed velocity in the mask is called an internal flow.

The error as a function of the penalization parameter and the convergence of the error

with the resolution are shown respectively on Figs. 2.7 and 2.8. The numerical error is only calculated in the fluid domain. It is observed that the convergence of the error with the penalization parameter is close to third order. An optimum for the penalization parameter depending on the resolution appears, when the gridscale becomes of order $\sqrt{\nu\eta}$. At this scale the viscous term becomes of the order of the penalization term. In Figs. 2.7 and 2.8 results for both explicit and semi-implicit methods are presented.

The regularization of the boundary conditions using an interpolation clearly improves the numerical convergence of the solution with the penalization parameter. Also the convergence with the grid resolution is improved. If the Hermite interpolation is used, a fourth order convergence with N is found for both the explicit (dashed line) and semi-implicit (solid line) implementations (see Fig. 2.8). We recall that if no regularization of the velocity field is introduced, second order convergence is recovered (see Fig. 2.6).

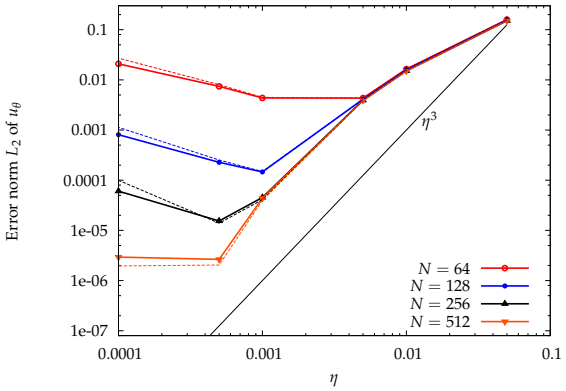

Figure 2.7: Taylor-Couette: convergence of the relative L_2 error with the penalization parameter η, semi-implicit (solid line) and explicit (dashed line) methods.

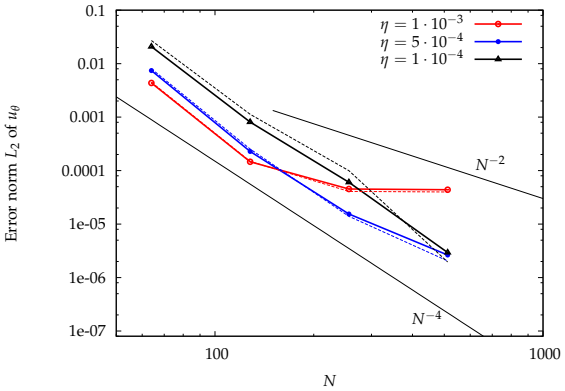

Figure 2.8: Taylor-Couette: convergence of the relative L_2 error with the resolution N, semi-implicit (solid line) and explicit (dashed line) methods.

5.2 THE Z-PINCH

The second validation test is the reproduction of the z-pinch phenomenon, a well-known textbook example of a confined plasma situation [41]. This configuration is illustrated in Fig. 2.9. Two ideal electrodes drive an axial current in the z-direction producing a purely azimuthal magnetic field (in the θ-direction). The current density in the z-direction, which together with the induced azimuthal magnetic field yield a radially pinching Lorentz force, is the motivation for the name z-pinch. In this configuration we set the velocity to zero so the code is entirely magnetic. We impose the boundary conditions $B_\theta = B_C$ and $B_r = 0$ at $r = R_1$ the radius of the fluid domain. The component B_z is not penalized and can freely evolve.

Periodic conditions are set in the axial direction. In this configuration the governing

equations reduce to

$$\partial_t \boldsymbol{B} \;=\; \lambda \nabla^2 \boldsymbol{B} \tag{2.26}$$

In cylindrical coordinates, the steady state solution is a linear evolution of the azimuthal magnetic field

$$B_\theta(r) = \frac{B_C r}{R_1}. \tag{2.27}$$

The quantity B_C/R_1 is linked to the constant axial current density, using Ampère's law,

$$j_z = \frac{2B_C}{R_1}. \tag{2.28}$$

The computational domain is chosen similar to Fig. 2.2 (left). The mask is chosen to be annular, leaving the outer domain free to adapt to the periodic boundary conditions of the computational domain. If a uniform azimuthal magnetic field is imposed inside the mask, the discontinuity in the profile of the radial derivative of the azimuthal magnetic field at the boundary causes Gibbs' oscillations in the current density, analogously to what was observed in the Taylor-Couette case. To avoid this, a linear profile of $B_\theta(r) = \frac{B_C r}{R_1}$ is imposed inside the mask to ensure a continuity with the analytical solution. This feature eliminates the discontinuity at $r = R_1$ in the derivative of the magnetic field and thus greatly reduces the oscillations for j_z. The convergence of the method can be further enhanced by using a Hermite polynomial to smoothly interpolate the magnetic field in the mask to zero at the outer boundaries of the computational domain. With this method, the continuity of the derivative of the magnetic field is assured through the entire domain (see Fig. 2.2 (right)).

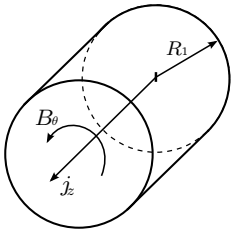

Figure 2.9: z-pinch configuration.

For these simulations the number of grid points are the same as for the Taylor-Couette case ($N \in \{64, 128, 256, 512\}$). The parameters are a cubic domain with size-length 2π with magnetic diffusivity $\lambda = 1$, the time step is fixed to $\Delta t = 5.10^{-5}$ and $t_{max} = 5$. For $t = t_{max}$ the difference in the magnetic energy between two iterations is less than 10^{-9} so we have reached the steady state. The inner radius of the annulus is $R_1 = 0.65\pi$ and the outer radius is $R_2 = 0.78\pi$. If the Hermite polynomial is used, the radius where it reaches the value 0 is $R_3 = 0.94\pi$. The boundary condition $B_C = 1$.

In Fig. 2.10 the convergence of the method is shown as a function of the penalization parameter η and the resolution N. An improved convergence, proportional to η^4 or N^{-4} is observed. The relative importance of the smoothing of the magnetic field in the mask is illustrated in Fig. 2.10 where the results of these computations with and without regularization are compared. Without the regularization technique, the convergence reduces to second order in N and order $\sqrt{\eta}$ for the penalization parameter.

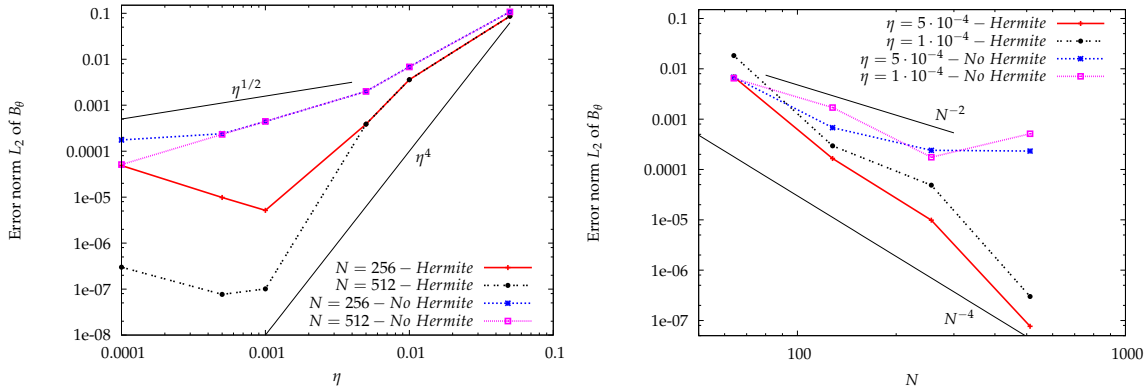

Figure 2.10: Z-pinch: convergence of the relative L_2 error with the penalization parameter η (left) and with the resolution N (right) for the magnetic field in the z-pinch geometry. Comparison of the results with and without Hermite polynomial interpolation.

5.3 ASSESSMENT OF THE REGULARIZATION METHOD TO ENHANCE THE PERFORMANCE OF THE PENALIZATION METHOD

For these two-dimensional test cases, either Taylor-Couette or z-pinch, the error of convergence as a function of the penalization parameter and the resolution are determined. The regularization of the different fields in the solid domain (or mask) allows an enhancement of the accuracy of the numerical solution in the fluid region. The fact that the continuity of the velocity derivative field inside the solid domain affects the error inside the fluid domain is an intrinsic feature of the pseudo-spectral method. Such methods use periodic trial functions and the Gibbs oscillations introduced in one point of the domain decay only inversely proportional to the distance from the discontinuity. The Hermite interpolation method regularizes and yields fields which are C^1 in the whole domain (see Appendix A for an analytical analysis of the Hermite regularization). Gibbs oscillations are thus reduced and consequently the numerical errors are also decreased considerably. The limitation of this method is that an analytical solution must be known, or a baseflow, which is not far from the expected developed flow. Without such regularization the convergence is reduced to second order in resolution, which can be sufficient for many applications, as illustrated in the following sections.

6 THREE-DIMENSIONAL VALIDATION

In this section the code will be validated by considering three-dimensional test-cases. First a periodic MHD case is considered, without using the penalization method, subsequently the magnetic part of the code is validated by studying the Ohmic decay in a cylindrical cavity. Then the three-dimensional Taylor-Couette flow is studied with and without the presence of a magnetic field and to conclude we investigate the instabilities in a cylinder with helical magnetic boundary conditions.

6.1 PERIODIC MHD VALIDATION

To validate the capacity of the numerical code to simulate the three-dimensional non-linear MHD equations, we reproduce first a classical test-case with periodic boundary conditions. This case is the generalization of the Orszag-Tang vortex to three dimensions. The results are compared with those of Mininni *et al.* [65].

The initial condition used for the simulation is given analytically and yields:

$$\boldsymbol{u}(x,y,z,t=0) = [-2\sin(y), 2\sin(x), 0] \text{ for } x,y,z \in [0,2\pi]^3 \tag{2.29}$$

and

$$\boldsymbol{B}(x,y,z,t=0) = \beta[-2\sin(2y)+\sin(z), 2\sin(x)+\sin(z), \sin(x)+\sin(y)] \tag{2.30}$$

with $\beta = 0.8$, the initial kinetic energy, $E_k = 2$, and the corresponding magnetic energy, $E_m = 1.92$. The energies are evaluated by $E_k = \frac{1}{2}\langle \mathbf{u}^2 \rangle$ and $E_m = \frac{1}{2}\langle \mathbf{B}^2 \rangle$ with $\langle .. \rangle$ the volume average. The maximum of the current density is calculated by

$$max\,|\boldsymbol{j}| = max\sqrt{j_x^2 + j_y^2 + j_z^2} \tag{2.31}$$

and the total dissipation rate is

$$\varepsilon(t) = \nu\ \langle \omega^2 \rangle + \lambda\ \langle j^2 \rangle, \tag{2.32}$$

where ν and λ are respectively the kinematic viscosity and the magnetic diffusivity. Three runs are performed: the first with $N^3 = 64^3$ and $\nu = \lambda = 0.01$, the second with $N^3 = 128^3$ and $\nu = \lambda = 0.005$ and the third $N^3 = 256^3$ with $\nu = \lambda = 0.001$.

The evolution of the maximum of the current density and total dissipation rate in the domain are shown in Fig. 2.11. Results are compared using a second- and third-order Adams-Bashforth time advancing scheme described in section 3.3. Both schemes give the same results. The results agree well with the computations presented in reference [65]. The same exponential growth followed by a self similar growth $\sim t^3$ is found in our calculations for the evolution of the maximum current density (see Fig. 2.11 (left)). With an increasing Reynolds number *Re* the maximum of $|\boldsymbol{j}|$ is also found to be reached at later

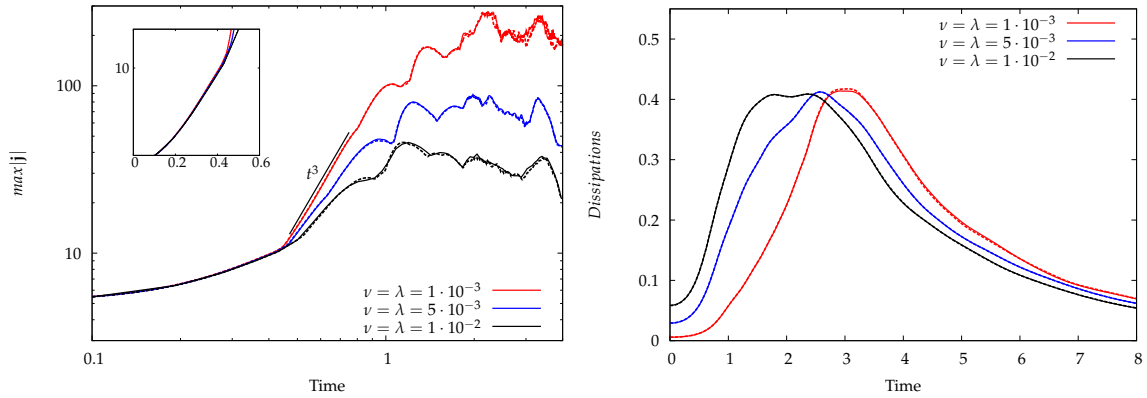

Figure 2.11: Comparison of the solution of the numerical code for the time evolution of the maximum of the current (left) and total dissipation rate (right) using second (dashed line) and third order time-schemes (solid line). The inset (left) shows the evolution at early times in lin-log units.

times. The evolution of the total dissipation rate (see Fig. 2.11 (right)) shows the same delay in the onset of the formation of small scales with increasing Re as exposed in the cited article. This test allows us to evaluate the full MHD code and validate the numerical results for relatively high Reynolds numbers (up to $Re = 3000$).

6.2 OHMIC DECAY IN A PERIODIC CYLINDER

In this test case we compute the evolution of the magnetic field in a periodic three dimensional cylinder coated with an insulator [40, 53]. In the induction equation we set the velocity to zero so the equation for the magnetic field reduces to the diffusion equation:

$$\frac{\partial \boldsymbol{B}}{\partial t} = \nabla^2 \boldsymbol{B}. \tag{2.33}$$

We consider an axisymmetric case, z-independent and the magnetic field has no r component. This case is not completely three-dimensional since we use the three components of the magnetic field (B_x, B_y, B_z), but the derivatives are zero in the z direction. In cylindrical coordinates the set of equations is:

$$\begin{cases} \dfrac{\partial B_\theta}{\partial t} = \dfrac{\partial^2 B_\theta}{\partial r^2} + \dfrac{1}{r}\dfrac{\partial B_\theta}{\partial r} - \dfrac{B_\theta}{r^2} \\ \dfrac{\partial B_z}{\partial t} = \dfrac{\partial^2 B_z}{\partial r^2} + \dfrac{1}{r}\dfrac{\partial B_z}{\partial r}. \end{cases} \tag{2.34}$$

Using separable elementary solutions, the magnetic field can be written in the following form:

$$\begin{cases} B_\theta(r,t) = A\, f(r) e^{-\omega_\theta^2 t} \\ B_z(r,t) = B\, g(r) e^{-\omega_z^2 t}. \end{cases} \tag{2.35}$$

Introducing the following change of parameter: $s = \omega r$ the system of equations writes:

$$\begin{cases} s_\theta^2 f'' + s_\theta f' + ({s_\theta}^2 - 1) f = 0 \\ s_z^2 g'' + s_z g' + s_z^2 g = 0. \end{cases} \tag{2.36}$$

The solutions of these equations are Bessel functions. Imposing at the radius R_0 of the cylinder the azimuthal and axial field vanishing the general solution is:

$$\begin{cases} B_\theta(r,t) = J_1\left(\frac{j_1}{R_0} r\right) e^{-\left(\frac{j_1}{R_0}\right)^2 t} \\ B_z(r,t) = J_0\left(\frac{j_0}{R_0} r\right) e^{-\left(\frac{j_0}{R_0}\right)^2 t}. \end{cases} \tag{2.37}$$

Here $j_0 = 2.4048...$ and $j_1 = 3.8314...$ are the first zeros of the Bessel functions J_0 and J_1 respectively.

In our simulation we set $R_0 = 1$. The decay rate is determined doing a least square fitting of the azimuthal and axial magnetic energy time evolutions (Figs. 2.12 and 2.13). In table 2.2 we present our results for the decay rate of the azimuthal and axial fields and we compare them to the analytical values (see Eq. (2.37)). All the simulations are done with 96^3 grid points, the penalization parameter $\eta = 5 \cdot 10^{-4}$ and the computational domain size is $L_x = L_y = L_z = 2\pi$. We calculate the error for different fixed time steps. In none of these calculations the regularization of the magnetic field in the solid region (mask) is used.

Time step	Theory ${\omega_\theta}^2$	Numerical ${\omega_\theta}^2$	Error ${\omega_\theta}^2$	Theory ${\omega_z}^2$	Numerical ${\omega_z}^2$	Error ${\omega_z}^2$
$1 \cdot 10^{-2}$	14.68	12.68	14 %	5.78	4.99	14 %
$1 \cdot 10^{-3}$		13.99	5 %		5.51	5 %
$5 \cdot 10^{-4}$		14.13	4 %		5.57	4 %
$1 \cdot 10^{-4}$		14.28	3 %		5.62	3 %

Table 2.2: Comparison of analytical (see Eq. (2.37)) and numerical calculation of the decay rate for the Ohmic diffusion in an infinite cylinder.

For these calculations of the diffusion of a magnetic field in a periodic cylinder the decay rate of the azimuthal and axial component of the magnetic field agree quite well with the analytical values. We find the same relative error in the azimuthal and in the axial direction at each considered time discretization.

This test-case yields a validation of the magnetic part of the numerical code and shows that the magnetic boundary conditions are well taken into account via the penalization method. Also we note that the time scheme is well implemented as it allows to recover the analytical decay rates for the considered components of the magnetic field with good accuracy. The numerical solution converges towards the analytical solution if the time step is decreased.

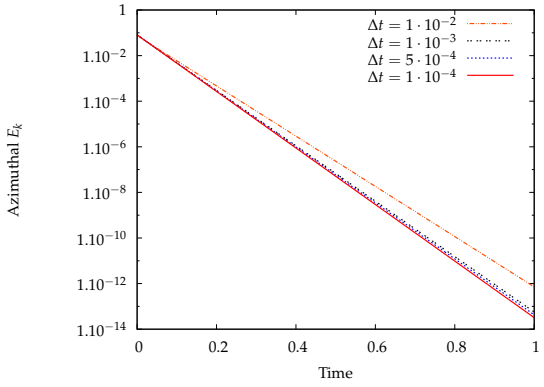

Figure 2.12: Azimuthal magnetic energy decay for different time steps in an periodic cylinder.

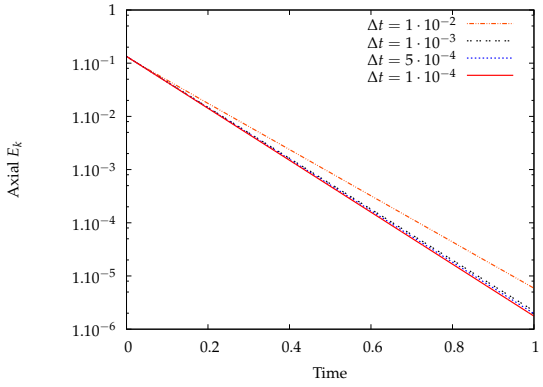

Figure 2.13: Axial magnetic energy decay for different time steps in an periodic cylinder.

6.3 THREE-DIMENSIONAL TAYLOR-COUETTE FLOW

In this test case we aim to determine the critical Reynolds number for the first instability of the Taylor-Couette flow with periodic boundaries in the axial direction. Different values of the Reynolds number are explored with several calculations with a resolution of 128^3 grid-points, the penalization parameter $\eta = 5 \cdot 10^{-4}$ and the computational domain size is $L_x = L_y = 5\pi/2$ and $L_z = 2\pi$. To assess the influence of the Hermite interpolation method, in one of these calculations the regularization of the velocity in the solid region (mask) is used (for the case with $Re = 120$). The reference length scale is the gap between the inner and outer cylinder $\mathscr{L} = R_{ext} - R_{int}$ and the reference velocity is the inner rotation speed $U = \Omega_{int} R_{int}$. The outer cylinder is fixed. We define the Reynolds number and also a radius ratio ζ and a aspect ratio Γ as follows:

$$Re = \frac{U\mathscr{L}}{\nu}, \qquad \zeta = \frac{R_{int}}{R_{ext}}, \qquad \Gamma = \frac{L_z}{\mathscr{L}}, \tag{2.38}$$

where L_z is the axial length. To be able to compare with the literature we take the same values as in [39] for the dimensionless values, radius ratio and aspect ratio, $\zeta = 0.5$ and $\Gamma = 4$. The base flow consists of an azimuthal velocity only, as in the two-dimensional case (section 5.1). The first Taylor-Couette instability is centrifugal and is characterized by vortices that appear and break the axial invariance. Velocities in the radial and axial directions thereby appear. To determine the critical Reynolds number we analyze the evolution of the axial kinetic energy. The analysis of the evolution of the axial kinetic energy allows us to assess the critical Reynolds number (when the instability is triggered). The value of the critical Reynolds is compared with a theoretical value of $Re = 68.23$ that has been determined by Chandrasekhar [25]. We present in Fig. 2.14 the axial kinetic energy evolution for Reynolds numbers varying from $Re = 65.7$ to $Re = 69.7$. We start the simulations with a small random perturbation so the initial axial kinetic energy is non zero. The axial energy either grows or decays exponentially. The critical Reynolds number

can be determined from Fig. 2.14. Increasing the Reynolds number from $Re = 67.3$ to $Re = 68.1$ the axial kinetic energy changes from decaying to increasing. A simple linear interpolation of the growth and decay rates (that are determined with a least square method fitting) gives the value of the critical Reynolds $Re_c \approx 67.9$. The estimated error compared with the theoretical result is $\sim 0.44\%$. The theoretical estimate is thus well approached by our numerical simulations.

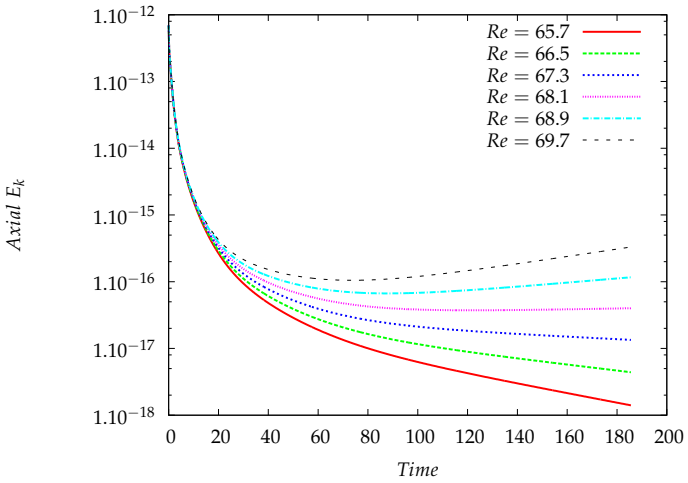

Figure 2.14: Evolution of the axial kinetic energy for different Re numbers.

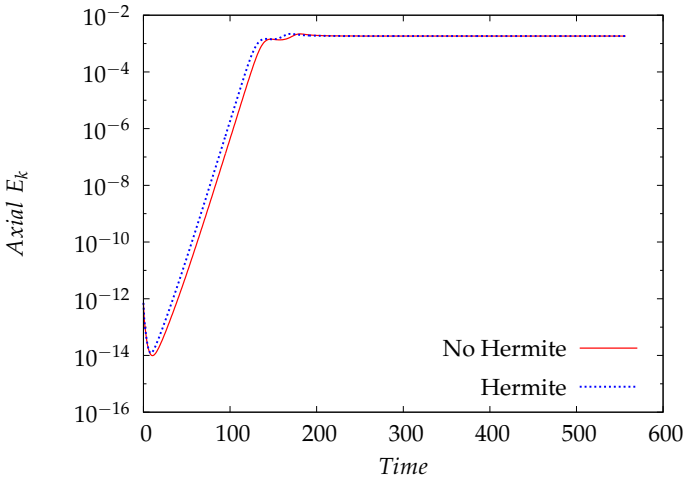

Figure 2.15: Evolution of the axial kinetic energy for $Re = 120$, with and without the regularization technique.

The Taylor vortices appear early in the simulation and they grow or decay in strength depending on the Reynolds number. Fig. 2.15 presents the axial kinetic energy evolution of a Taylor-Couette flow for $Re = 120$ comparing two simulations, one with Hermite regularization and one without. The difference between the two considered methods is

the onset of the instability, it is slightly earlier if the Hermite regularization is used. The growth rates are similar, when the nonlinear saturation is reached, a steady state is obtained that almost coincides for both methods. In Figs. 2.16 to 2.19 we visualize the Taylor vortices in the steady state. Two pairs of counter-rotating vortices appear. The aspect ratio is $\Gamma = 4$ so that four vortices form. In Fig. 2.17 we distinguish the boundary layer, in which the azimuthal vorticity is contrary to the vorticity of the Taylor-vortices.

The flow structure of Figs. 2.16 to 2.19 can be compared with the one presented by Guermond *et al.* (Fig. 5 in [39]). The same flow topology with four vortices is found. In Figs. 2.18 and 2.19 we note that there is a transport of azimuthal momentum by the radial flow. The azimuthal velocity isosurfaces are not axial invariant but they are dragged in- and outwards by the radial flow. A positive radial velocity increases the azimuthal velocity near the inner cylinder.

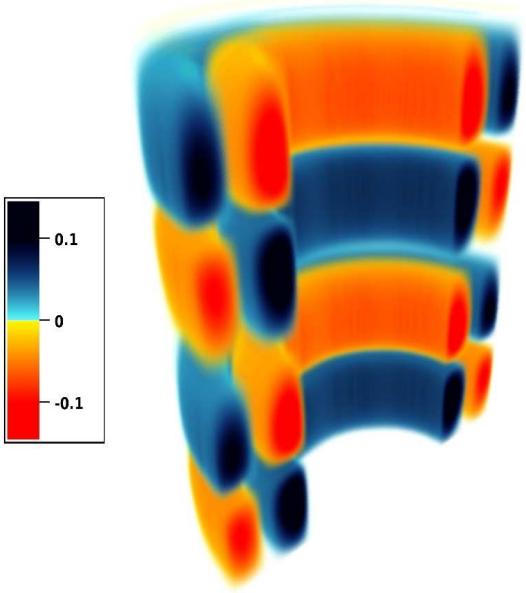

Figure 2.16: Axial velocity u_z (color) for $Re = 120$.

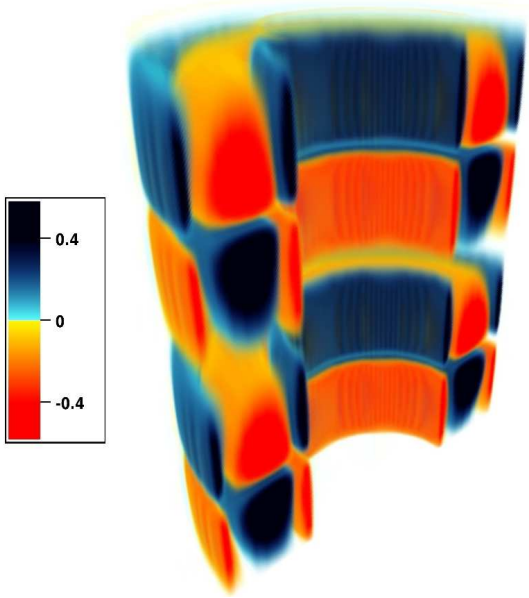

Figure 2.17: Azimuthal vorticity ω_θ (color) for $Re = 120$.

To compare quantitatively both simulations, in table 2.3 the maxima of the three velocity components at the steady state are compared with those of Guermond *et al.* [39].

The azimuthal velocity is not exactly unity because with the penalization method the precise value at the boundary is not necessarily coinciding with the numerical grid as is the case in [39]. Nevertheless the numerical method yields good agreement for all three components of the velocity with the results of the code described in [39]. The three numerical methods yield similar relative variations, there is an improvement in the error with the regularization for the radial component of the velocity field. The improvement is limited because the tangent imposed with the Hermite polynomial is calculated using the

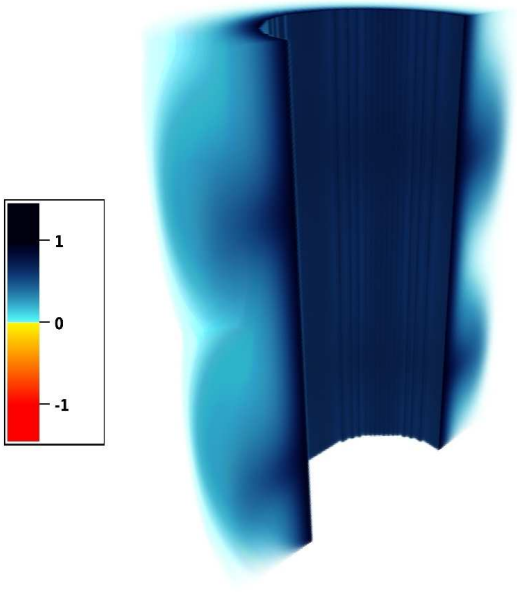

Figure 2.18: Azimuthal velocity u_θ (color) for $Re = 120$.

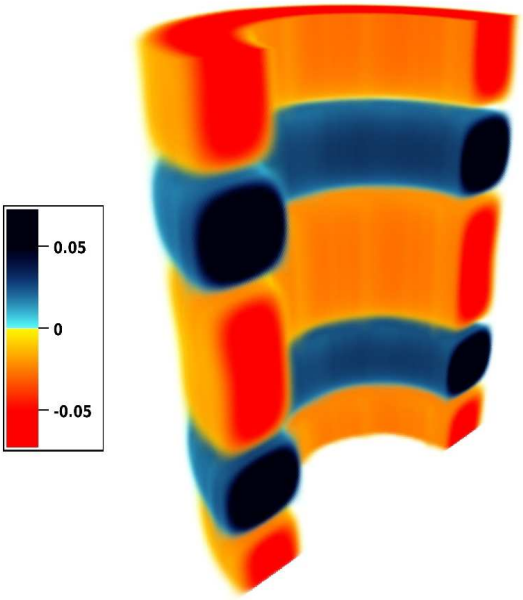

Figure 2.19: Radial velocity u_r (color) for $Re = 120$.

	Guermond *et al.* [39]	3rd order semi-implicit no regularization	2nd order explicit no regularization	3rd order semi-implicit with regularization
max u_r	0.1935	0.19434 ($\sim 0.43\%$)	0.1969 ($\sim 1.75\%$)	0.19355 ($\sim 0.03\%$)
max u_θ	1	0.99693 ($\sim 0.31\%$)	0.9980 ($\sim 0.20\%$)	0.99669 ($\sim 0.33\%$)
max u_z	0.1454	0.14639 ($\sim 0.68\%$)	0.1506 ($\sim 3.57\%$)	0.14632 ($\sim 0.63\%$)

Table 2.3: Maximum velocity components comparison and relative errors for $Re = 120$ in a periodic cylinder.

analytical base flow, which is known in this case. Since the development of the instability makes the flow change, discontinuities appear at the fluid-solid interface and the Gibbs oscillations can grow. The improvement can be substantial if the saturated state is not far from the calculated analytical base flow.

With this test-case the well known linear first instability threshold of the Taylor-Couette flow is found. Also the nonlinear saturation is comparable to what is reported in the literature. The same topology of the flow is observed and quantitatively similar velocity magnitudes at the steady state are established. This makes us confident about the accuracy of the method in taking into account centrifugal, pressure and nonlinear effects in a bounded domain.

6.4 MAGNETOHYDRODYNAMIC TAYLOR-COUETTE FLOW

We now extend our validation to the test-case of the instability of an axisymmetric MHD Taylor-Couette flow with periodic boundary conditions in the axial direction. In this case the instability studied in the previous section is modified due to the presence of an axial magnetic field. An imposed constant axial field B_0 is added to the magnetic field. It is well known that such an axial magnetic field has a significant stabilizing effect. This phenomenon of delay in the appearance of the first Taylor-Couette instability was found by Chandrasekhar [25], confirmed by linear numerical calculations in [95] and by spectral numerical simulations [110, 111]. The fluid flow will try to bend the axial magnetic field lines but the restoring Lorentz force will prevent the fluid motion, which stabilizes the flow profile.

To assess our numerical code in this context, we evaluate the evolution of the axial kinetic energy as a function of the Hartmann number Ha, which measures the ratio between electrodynamic forces and viscous forces. The presence of a uniform magnetic field in the axial direction does not affect the profile of the stable azimuthal velocity that exists without the magnetic field, Eq. (2.25), which we choose as initial condition. The dimensionless geometric parameters, radius ratio ζ and aspect ratio Γ are the same as in the previous section. We introduce here the magnetic Prandtl number which is the ratio of viscosity and magnetic diffusivity. The dimensionless numbers describing the problem are then

$$Pr = \frac{\nu}{\lambda}, \qquad Re = \frac{U\mathscr{L}}{\nu}, \qquad Ha = \frac{B_0\mathscr{L}}{\sqrt{\mu_0\rho\nu\lambda}}, \qquad \zeta = \frac{R_{int}}{R_{ext}}, \qquad \Gamma = \frac{L_z}{\mathscr{L}}, \tag{2.39}$$

where μ_0 is the magnetic constant and ρ is the fluid density. The simulations are performed for $Pr = 1$, $Re = 100$, $\zeta = 0.5$ and $\Gamma = 4$. The resolution used is $N^3 = 128^3$, the penalization parameter $\eta = 5 \cdot 10^{-4}$ and the computational domain size is $L_x = L_y = 5\pi/2$ and $L_z = 2\pi$. For none of these calculations regularization of the velocity or magnetic field in the solid region (or mask) is used. The boundary conditions described in [95] are a fixed azimuthal velocity on the inner cylinder ($U = \Omega_{int} R_{int} = 1$), no-slip on the outer cylinder and perfectly conducting walls, so that the normal magnetic field at the wall and the axial current density vanish ($b_r = 0$ and $j_z = 0$) [95]. With these parameters the Taylor-Couette flow is hydrodynamically unstable, as was observed in the previous section. With the penalization method we can impose the vanishing radial magnetic field but the current density is not constrained.

The evolution of the axial kinetic energy varies as a function of the imposed magnetic field (or Hartmann number), for a fixed Reynolds number, as is shown in Fig. 2.20. These calculations allow us to determine the threshold for the instability. For $Re = 100$ the critical Hartmann number found is $Ha_c \approx 7.9$. Like in the previous section the threshold is determined by linear interpolation of the growth and decay rates. For $Re = 100$ the flow is hydrodynamically unstable and Taylor vortices should appear, but for $Ha > 7.9$, the instability is suppressed by the magnetic field.

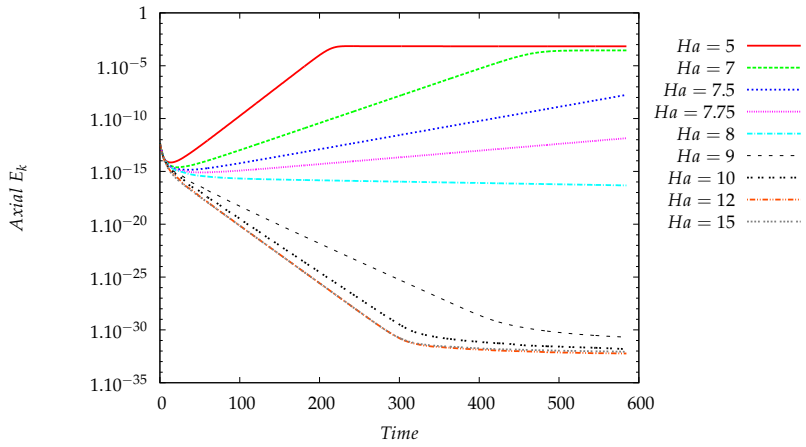

Figure 2.20: Evolution of the axial kinetic energy for different Hartmann numbers.

In Fig. 2.21 we show the topology of the flow resulting of our simulation (cut in the $r-z$ plane). This figure could be compared to Fig. 1 in [110]. This comparison is merely qualitative, since the ratio of the radii is $\zeta = 0.95$ in the cited reference and here we have used $\zeta = 0.5$. We have not tried to quantitatively study the same geometry, since our method is not particularly adapted for the case $\zeta = 0.95$, because a very large part of the computational domain would correspond to the mask. To obtain a reasonable number of grid-points in the fluid domain, extremely large resolutions would be needed. Immersed boundary methods with uniform space discretization are clearly not the most adapted tool for this aspect ratio. The parameters chosen in our simulation are $Pr = 1$, $Ha = 7$, $Re = 100$, $\zeta = 0.5$ and $\Gamma = 4$. Despite the different parameters for the two computations, the resulting hydromagnetic flow has a similar topology. We note how the magnetic lines are advected by the flow. The resulting restoring Lorentz force stabilizes the fluid.

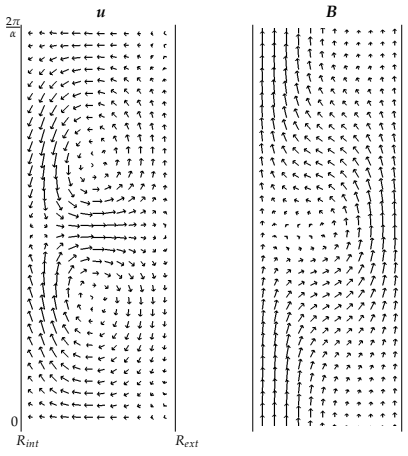

Figure 2.21: Hydromagnetic flow. Cut in the $r-z$ plane of velocity $\boldsymbol{u}$ (left) and magnetic ($\boldsymbol{B}$) field (right) for $Pr = 1$, $Ha = 7$, $Re = 100$, $\zeta = 0.5$ and $\Gamma = 4$.

With this test-case we therefore found the well known stabilizing effect of an axial

magnetic field on the Taylor-Couette flow. Qualitatively the flow behavior is very similar to what is found in other investigations. We were not able to quantitatively compare with the literature since our boundary conditions on the magnetic field are not the same as those considered in previous studies on magnetohydrodynamic Taylor-Couette flow and the parameter ζ was different. To compare with more accuracy our code with the literature we treat in the following section a test case with boundary conditions and geometry which are adapted to our numerical method.

6.5 FLOW INDUCED BY A HELICAL MAGNETIC FIELD

Shan, Montgomery and Chen [102] studied numerically a conductive fluid confined in a periodic cylinder where an axial electric and magnetic field are imposed, which results in a helical magnetic field (see Fig. 2.22). They used a spectral code which decomposed the fields into Chandrasekhar-Kendall orthonormal eigenfunctions of the curl. In that study they discovered a transition between an axisymmetric state with a zero velocity to a laminar helical state where a dynamic equilibrium appears, *i.e.*, a steady state with non zero velocity.

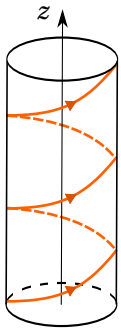

Figure 2.22: Helical magnetic field scheme.

The parameters chosen for the numerical study are selected to closely reproduce the simulations in [102]. A fixed axial magnetic field $B_0 = 4.5$ is imposed and the fluid has a constant magnetic diffusivity and kinematic viscosity $\lambda = \nu = 0.045$. The computational domain size is $L_x = L_y = 0.8\pi$ and $L_z = 8$. The typical length scale is the cylinder radius, $\mathscr{L} = R_0 = 1$, the axial length is $L_z = 8R_0$, the resolution used for the simulations is $N^3 = 128^3$ grid-points and the penalization parameter $\eta = 5 \cdot 10^{-4}$. Three dimensionless numbers characterize the system: the Lundquist number (S), the Hartmann number (Ha) and the pinch ratio for the axisymmetric zero flow state (Θ_0):

$$S = \frac{C_A \mathscr{L}}{\lambda}, \qquad Ha = \frac{B_0 \mathscr{L}}{\sqrt{\rho \mu_0 \lambda \nu}}, \qquad \Theta_0 = \frac{\overline{B_\theta}}{\langle B_z \rangle}, \tag{2.40}$$

with C_A the axial Alfvén velocity $C_A = B_0/\sqrt{\rho\mu_0}$, $\overline{B_\theta}$ is the wall-averaged poloidal magnetic field and $\langle B_z \rangle$ is the volume-averaged axial magnetic field.

The transition between states is determined as a function of one of these dimensionless numbers, the pinch ratio Θ_0, which is varied by adjusting the imposed average axial electric field E_0 and which is directly linked to the poloidal magnetic field. The other dimensionless numbers are maintained constant, $S = Ha = 100$. For the parameters given above, the linear theory predicts a transition for an imposed electric field $E_0 = 0.33$ [102, 71].

To compare with Shan *et al.* we impose the same boundary conditions. The walls are treated as perfect conductors and are coated with a thin layer of insulator. Hereby both the radial magnetic and current density field vanish ($B_r = j_r = 0$). For the velocity field only the radial component vanishes at the wall. The penalization method is used to impose a vanishing normal component of the velocity ($\boldsymbol{u} \cdot \boldsymbol{n} = 0$) without any regularization technique. Also an azimuthal magnetic field B_{0_θ} is imposed via the penalization term. In this case the vanishing radial current density ($j_r = 0$) is automatically satisfied because the azimuthal magnetic field does not generate a radial current density (the r-component of the curl of the imposed magnetic field is zero). The boundary conditions are thus satisfied.

The way the electric field is imposed in our simulations differs from the simulations by Shan *et al.*. In their simulations the electric field explicitly appears in the discretized equations, whereas in our case the electric field is indirectly imposed through the magnetic field at the wall (which can be related to the electric field using Stokes' theorem). This can lead to small differences in the transients, but is not expected to greatly affect the steady state solutions.

The azimuthal magnetic field $B_{0_\theta}(r)$ is imposed with the volume penalization method in the solid region using the regularization technique, like for the z-pinch case (see section 5.2). The azimuthal magnetic field increases linearly with r from $r = R_0$ (the fluid-solid frontier) to $r = 0.34\pi$ and then smoothly tends to zero using a Hermite's interpolating polynomial from $r = 0.34\pi$ to $r = 0.385\pi$. The periodicity of the computational region is hereby satisfied and the magnetic derivative of the base-field is continuous at the wall.

To validate the code we perform the same calculations done by Shan *et al.*. We vary the axial current density (j_z) and we calculate E_0 when the simulation reaches a steady state using Ohm's law

$$E_0 = (-\boldsymbol{u} \times \boldsymbol{B})_z + \frac{j_z}{\sigma}. \tag{2.41}$$

We find (see Fig. 2.24) that the instability threshold between the axisymmetric and helical state is situated between $E_0 = 0.302$ and $E_0 = 0.355$ as found in [102]. The kinetic energy starts to grow when the imposed electric current is $E_0 = 0.355$. The growth rate of the energy is calculated using Alfvén time units ($t_A = t_{num} C_A / L_z$). A least-square fitting gives the growth rate of the kinetic energy as 0.54, corresponding to a growth rate of 0.27. This can be compared to the analytical value 0.279 calculated for an applied electric field $E_0 = 0.35$. Taking into account that our imposed magnetic field is slightly different (since the electric field is imposed indirectly in our case), the two different growth rates match in good order. In Fig. 2.23 the excited mode is visualized, which is a helical mode with azimuthal and axial mode numbers $m = k_z = 1$, respectively, as in [102].

Figure 2.23: First helical mode, velocity streamlines colored with the axial velocity u_z.

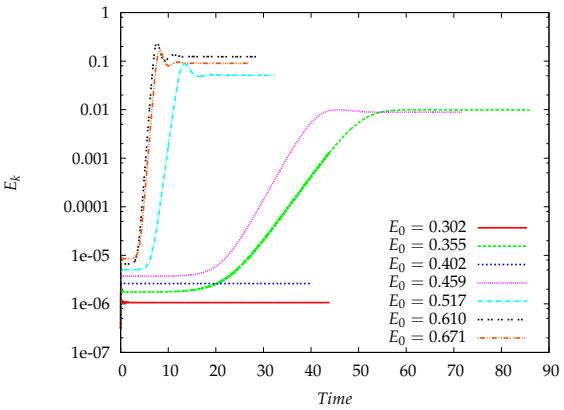

Figure 2.24: Evolution of the kinetic energy for different imposed axial electric fields.

Increasing the pinch ratio to $E_0 = 0.402$ the flow returns to its axisymmetric *copper-wire* solution, which is also observed for certain values in [102]. An explanation for this behavior is the shape of the instability curves in the $\Theta_0 - Ha$ plane. By increasing the pinch ratio, different (m, k_z) helical modes appear at a fixed Ha, but they can disappear by increasing Θ_0 to even higher values. This was investigated in [100].

In the next figures, 2.25 to 2.28, we compare our different simulations with the ones performed by Shan *et al.*. We find quantitatively the same evolution of the average current density and the total dissipation rate ($\varepsilon_T = \lambda \ \langle j^2 \rangle + \nu \ \langle \omega^2 \rangle$). These quantities are time averaged during the dynamical steady state, since the flow becomes chaotic, if the pinch ratio (or E_0) is large.

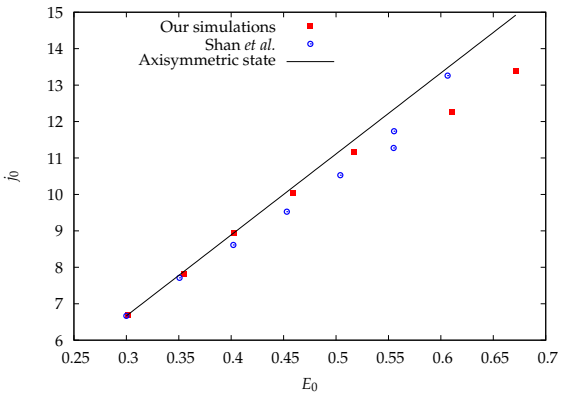

Figure 2.25: Zoom: average axial current as a function of the average electric field.

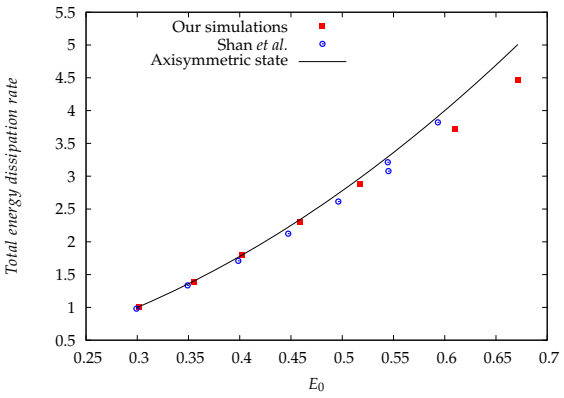

Figure 2.26: Zoom: total energy dissipation rate as a function of the average electric field.

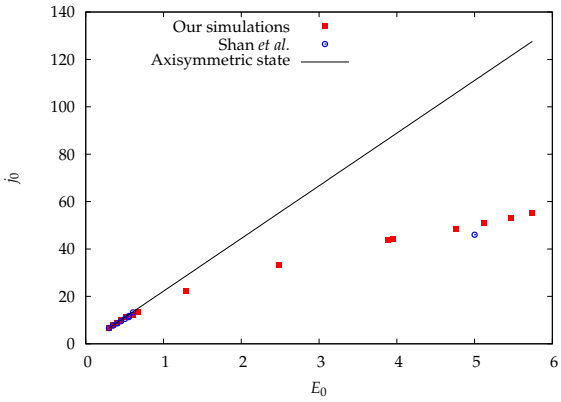

Figure 2.27: Average axial current as a function of the average electric field.

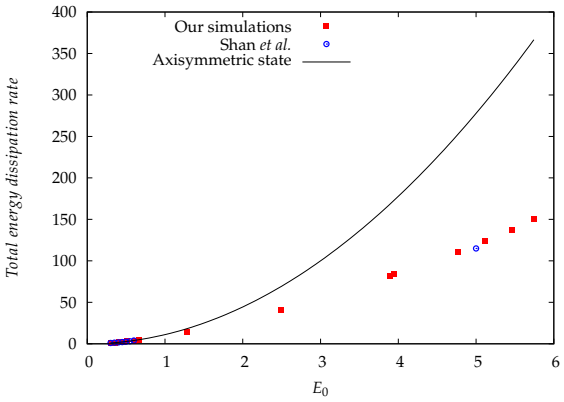

Figure 2.28: Total energy dissipation rate as a function of the average electric field.

Some quantitative differences are observed in Figs. 2.25 and 2.26 for values around $E_0 = 0.6$. At that point both methods might not trigger exactly the same helical modes, since the electric field is imposed in a slightly different way. Both methods might therefore give results corresponding to different multi-mode states. When the pinch ratio is increased further, the deviations become smaller, as can be seen in Figs. 2.27 and 2.28.

This test-case allows us to validate the nonlinear MHD code with boundary conditions imposed on both the velocity and magnetic field. A linear analytical result is confirmed. The "multi-mode" and turbulent states that are observed in literature also appear in our simulations.

7 CONCLUDING REMARKS CONCERNING THE NUMERICAL METHOD

An extension and implementation of the penalization method into a pseudo spectral Fourier code solving the MHD equations is presented. This penalization method, which allows the introduction of obstacles and walls in the computational domain, is implemented in different ways with respect to the numerical scheme and definition of the fields within the solid domains.

The numerical code is validated by comparison with several test-cases and theory. First in two dimensions the convergence of the results towards an analytical solution by decreasing the penalization parameter and increasing the resolution are shown. The method converges faster than second order if a regularization technique in the solid domain is applied which removes the discontinuities in the derivatives of the velocity and magnetic field at the solid-fluid boundary.

Then in three dimensions the first instability threshold of the hydrodynamic Taylor-Couette flow is found with good accuracy. Also the nonlinear saturation of this flow is compared and validated with the literature. For the MHD Taylor-Couette flow the current inability to impose non-homogeneous Neumann boundary conditions using the penalization method, makes the comparison of our numerical results with the literature difficult. A more appropriate test-case to validate the three-dimensional implementation of the penalization method to compute MHD flows is the flow induced by a helical magnetic field. This case is correctly reproduced. The linear threshold of the transition between an axisymmetric and a helical state is found. Also the evolution of the average axial current and the total dissipation rate as a function of the average electric field are compared with the literature and are in good agreement.

All these test-cases allowed us to validate the numerical method to solve correctly the MHD equations in a confined domain. The limitations are the restricted magnetic boundary conditions that can be applied. Presently, the current density can only be imposed indirectly via the magnetic field. A modified volume penalization method that allows the introduction of non-homogeneous three-dimensional Neumann boundary conditions is currently being developed, preliminary one-dimensional results are presented in Appendix B.

III

MAGNETOHYDRODYNAMICALLY GENERATED VELOCITIES IN CONFINED PLASMA

1 INTRODUCTION

Toroidal magnetic plasma confinement has been under investigation since the 1940s when it was recognized as a promising geometry for controlled thermonuclear fusion. Despite all the attention devoted to the idea, there are aspects of it that must be regarded as incomplete, even in theory. The difficulties in many cases reduce to the fact that there is no mathematical description of a magnetically active, dissipative plasma that is tractable, by use of even the fastest supercomputers. Time dependent electromagnetic fields combined with the particle kinetics of plasmas having the range of mass ratios represented among the various charges is simply a too large system to be susceptible to a complete treatment. Enormous simplifying assumptions have to be made to achieve any analytical/numerical progress. A common assumption has been that of an unstable ideal equilibrium whose numerous linear instabilities may reveal insight into the nonlinear dynamical behavior that is observed. It must be conceded that any description that is manageable at a detailed level will omit certain important features of a real plasma and at this stage it is to some extent a matter of taste as to which incomplete theoretical description is adopted for study.

In the following pages, we report the investigation of one such description: a voltage driven, dissipative magnetohydrodynamic (MHD) fluid with non-ideal toroidal boundaries. We omit some features that would be desirable and which seem reasonable to inject, at a later date, one at a time, into the numerical recipe we use. The principal unrealistic

assumptions we make are those of uniform mass density and incompressibility, a scalar valued Newtonian viscosity, a scalar valued electrical conductivity, and the omission of a finite thermal conductivity (it will be seen that in effect an infinite thermal conductivity has been assumed, since no thermal effects are allowed to develop except those associated with the incompressible velocity field). Despite what appear to be these gross oversimplifications, what remains is at the very perimeter of what is computable if we intend to stay with arbitrary initial configurations which are not in equilibrium, and to follow through with enforcing viscous and resistive boundary conditions.

What is of particular interest is the spontaneous development of both toroidal and poloidal rotation of the bulk magnetofluid as a whole. It is not physically obvious that this should happen, even though it has been known for some time to occur in toroidal laboratory devices [94]. The importance of non-zero velocities in the MHD description of toroidally confined plasma was realized by Pfirsch and Schlüter [83], however without taking into account all the different terms in the force balance. We will take into account all these terms. The resulting flow pattern is presented here as a computational fact. The degree of the two types of rotation are seen to depend upon several things, such as the Reynolds-like dimensionless numbers assumed for the magnetofluid; the geometry of the toroid, which is allowed to have variable cross sections; the safety factor of the magnetofluid; and perhaps others.

The pseudo-spectral algorithm combined with the volume penalization method are used. This numerical method was presented in detail in the Chap. II. In this chapter a toroidal geometry is carved out within the periodic volume.

In Sec. 2, we fix the geometry of the confined magnetofluid and write down the system of equations and boundary conditions that will govern the dynamics. An external forcing of the magnetic field provides the toroidal electric field which initiates and drives the current. A vacuum toroidal dc magnetic field, regarded as externally supported from outside the system, is also assumed to be present. In addition another toroidal component of the magnetic field is allowed to develop in time if the dynamics so dictate.

In Sec. 3, the results are presented. They are divided in four different parts. The first discusses the generation of toroidal velocities for a dissipative system. The second exposes the results where the nonlinear term is dominant and a comparison is made between different toroidal geometries. In the third section we study the effect of the variation of the safety factor and in the last part, how the system evolves if the imposed toroidal magnetic field is inverted. We illustrate in detail the development of the driven magnetofluid configurations and the development of spontaneous toroidal rotation.

2 GEOMETRY AND GOVERNING EQUATIONS

In the MHD approximation the plasma is described as a charge-neutral conducting fluid. Despite its low complexity compared to kinetic descriptions it can give rise to a wealth of intricate phenomena and its analytical treatment is only possible in some simplified cases,

either in the absence of velocity fields [7, 99] or in the absence of non-linear interactions [6]. If one considers the complete problem one necessarily needs to consider a discretized numerical approximation of the full nonlinear system. Here we recall the equations we consider for the reader's convenience: the dimensionless incompressible viscoresistive MHD equations for the velocity field $\boldsymbol{u}$ and for the magnetic field $\boldsymbol{B}$, in 'Alfvénic' units [51].

$$\frac{\partial \boldsymbol{u}}{\partial t} - M^{-1}\nabla^2 \boldsymbol{u} = -\nabla\left(P + \frac{1}{2}\boldsymbol{u}^2\right) + \boldsymbol{u}\times\boldsymbol{\omega} + \boldsymbol{j}\times\boldsymbol{B}, \tag{3.1}$$

$$\frac{\partial \boldsymbol{B}}{\partial t} = -\nabla\times\boldsymbol{E}, \tag{3.2}$$

$$\boldsymbol{E} = S^{-1}\boldsymbol{j} - \boldsymbol{u}\times\boldsymbol{B}, \tag{3.3}$$

$$\nabla\cdot\boldsymbol{u} = 0, \qquad \nabla\cdot\boldsymbol{B} = 0, \tag{3.4}$$

with the current density $\boldsymbol{j} = \nabla\times\boldsymbol{B}$, the vorticity $\boldsymbol{\omega} = \nabla\times\boldsymbol{u}$, the pressure P and the electric field $\boldsymbol{E}$. These equations are non-dimensionalized using the toroidal Alfvén speed $C_A = B_{ref}/\sqrt{\rho\mu_0}$ as typical velocity, with $B_{ref} = 1.2$ the reference toroidal magnetic field at the center of the torus ($R = R_0 = 0.55\pi \approx 1.73$ and $Z = 0$ for both considered geometries), ρ the density and μ_0 the magnetic constant. We will exclusively consider two toroidal geometries with differently shaped cross-sections (see Fig. 3.1). The reference length L is the diameter of the cross section for the circular case and is the minor diameter for the asymmetric 'D' shape ($L = 0.6\pi \approx 1.88$ for both geometries). The 'D' shape parametric equation is a modified version of the formula given by Manickam [59],

$$R(t) = R_0 + \frac{L}{2}\left[\cos(t - \alpha + \delta\sin(t))\cos(\zeta) - \kappa\sin(t)\sin(\zeta)\right], \tag{3.5}$$

$$Z(t) = \frac{L}{2}\left[\cos(t - \alpha + \delta\sin(t))\sin(\zeta) + \kappa\sin(t)\cos(\zeta)\right], \tag{3.6}$$

with $t \in [0, 2\pi]$, δ the triangularity, κ the ellipticity, α the asymmetry and ζ the rotation angle. For the considered asymmetric cross section the following values of these parameters are chosen: $\delta = 0.5$, $\kappa = 2.1$, $\alpha = 0.4$ and $\zeta = 0.15$.

The MHD equations are completed by the initial and boundary conditions of the problem, and two dimensionless quantities: the viscous Lundquist number (M) and the Lundquist number (S) defined as

$$M = \frac{C_A L}{\nu}, \qquad S = \frac{C_A L}{\lambda}, \tag{3.7}$$

with λ the magnetic diffusivity and ν the kinematic viscosity. The ratio of these two quantities is the magnetic Prandtl number $Pr = \nu/\lambda$, which we have chosen unity in the present study, thereby reducing the number of free parameters, which characterize the magnetofluid, to one, the viscous Lundquist number, M. Previous investigations indicate that it is the geometric mean of the viscosity and the magnetic diffusivity which is important to the dynamics [21, 101]. In setting the Prandtl number to one, a change in the viscous Lundquist numbers, M or S, is equivalent to a change in the Hartmann number.

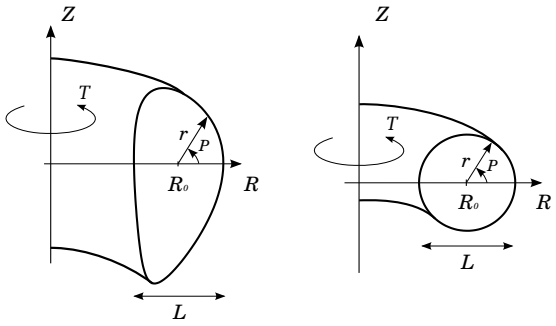

Asymmetric 'D' Circular

Figure 3.1: Cross-sections of the toroidal geometries considered in the present work. The toroidal direction is labelled T and the poloidal P.

In the ideal MHD framework a scalar-pressure equilibrium state is assumed in which $\boldsymbol{u} = 0$,

$$\boldsymbol{j} \times \boldsymbol{B} = \nabla P. \tag{3.8}$$

This equilibrium is possible in a cylindrical geometry, for instance in z- and θ-pinches. It is shown in [72, 5] that in the case of finite conductivity such an equilibrium is not possible in a toroidal geometry if irrotational toroidal magnetic and electric fields are applied. A steady state in Faraday's law imposes the toroidal electric field to be irrotational in the region of interest. The chosen spatial dependence for $\boldsymbol{E}_{0_T}$ is $\propto 1/R$. In the simple case of a space-uniform conductivity, which we consider in the present study, the current density has the same dependence. The form for the imposed toroidal magnetic field, which is also proportional to $1/R$, comes from the integration of Ampère's law on a toroidal loop. So the externally imposed magnetic field and toroidal, laminar, voltage-driven current density are given by,

$$\boldsymbol{B}_{0_T}(R) \propto \frac{R_0}{R}\boldsymbol{e}_T, \qquad \boldsymbol{j}_{0_T}(R) \propto \frac{R_0}{R}\boldsymbol{e}_T. \tag{3.9}$$

The toroidal magnetic and current density profiles give the imposed three-dimensional helical magnetic field $\boldsymbol{B}_0 = \boldsymbol{B}_{0_T} + \boldsymbol{B}_{0_{pol}}$, with $\boldsymbol{B}_{0_{pol}} = B_{0_R}\boldsymbol{e}_R + B_{0_Z}\boldsymbol{e}_Z$. The poloidal magnetic field is calculated from the current density distribution $\boldsymbol{j}_{0_T}(R)$. The reference toroidal current density at the center of the geometry (at $R = R_0$ and $Z = 0$) is $j_{T_{ref}} = 0.5$. For the details of generating the poloidal magnetic field in general geometries numerically we refer to Appendix D. Here $\boldsymbol{e}_T$, $\boldsymbol{e}_R$ and $\boldsymbol{e}_Z$ are unit vectors in the toroidal/azimuthal, radial and vertical directions respectively (Fig. 3.1).

The toroidal magnetic field magnitude is tuned to have an edge safety factor $q = \overline{rB_{0_T}|_{wall}}/R_0\overline{B_{0_P}|_{wall}} = 5.7$ for the asymmetric geometry and $q = 3.3$ for the symmetric cross section. A bar over a symbol indicates an average over the entire boundary. These safety factor values will be used for the majority of studied cases. The pinch-ratio associated to these values of q, defined as the ratio between the wall-averaged poloidal and the

volume-averaged toroidal imposed magnetic field, $\Theta_0 = \overline{B_{0_P}}/\langle B_{0_T}\rangle = 0.16$, is the same for both geometries. The resulting three-dimensional magnetic field lines are visualized for both geometries in Fig. 3.2.

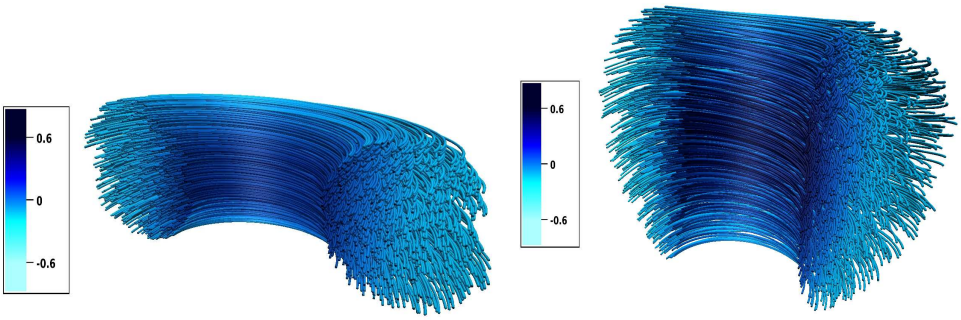

Figure 3.2: Three-dimensional magnetic field lines colored with the vertical magnetic field (B_Z). For the symmetric (left) and asymmetric (right) cross sections.

The Lorentz force resulting from the calculated poloidal field $\boldsymbol{B}_{0_{pol}}$ and the imposed toroidal current density $\boldsymbol{j}_{0_T}$ is not curl-free [72, 5]. Since the curl of a pressure gradient is necessarily zero, the equilibrium described by (3.8) becomes impossible and additional terms of Eq. (3.1) need to be taken into account to balance the equation. Since all other terms in (3.1) are proportional to (or quadratic in) the velocity, the resulting state must be dynamic. In other words if we take the curl of Eq. (3.1) we end with the vorticity equation,

$$\frac{\partial \boldsymbol{\omega}}{\partial t} - M^{-1}\nabla^2\boldsymbol{\omega} - \nabla\times(\boldsymbol{u}\times\boldsymbol{\omega}) = \nabla\times(\boldsymbol{j}\times\boldsymbol{B}) \neq 0, \tag{3.10}$$

we observe that if the Lorentz force term is not curl-free, it acts as a source of vorticity: a toroidal plasma, described by viscoresistive MHD, confined by curl-free toroidal electric and magnetic fields, necessarily moves!

It is true that the rationale described above depends on the choice of the electric conductivity, which was assumed to be uniform. It was however shown [69] that to satisfy Eq. (3.8) in a torus, very unusual profiles of the electrical conductivity must be assumed. The simple case of constant magnetic resistivity is then treated in this study. The case of non-uniform resistivity profiles is one important perspective.

It follows from the foregoing that it is necessary to take into account all other terms in the MHD equations, and analytical treatment becomes impossible unless symmetries are assumed. To study the full dynamics we are obliged to solve numerically the system and this is what is done in the present investigation. Equations (3.1)-(3.4) are discretized with a Fourier pseudo-spectral method on a Cartesian grid. To impose the boundary conditions we use the volume-penalization technique. The method is presented in detail for three-dimensional viscoresistive MHD equations in Chap. II.

The total magnetic field is decomposed into a base component and a perturbation,

$$\boldsymbol{B} = \boldsymbol{B}_0 + \boldsymbol{B}'. \tag{3.11}$$

Numerically only the perturbation of the magnetic field is computed, the base magnetic field, $\boldsymbol{B}_0$, computed from (3.9) is fixed and it is introduced in the Navier-Stokes equation and in the induction equation as follows,

$$\frac{\partial \boldsymbol{u}}{\partial t} - M^{-1}\nabla^2\boldsymbol{u} = -\nabla\left(P + \frac{1}{2}\boldsymbol{u}^2\right) + \boldsymbol{u}\times\boldsymbol{\omega} + \left(\boldsymbol{j}' + \boldsymbol{j}_0\right)\times\left(\boldsymbol{B}' + \boldsymbol{B}_0\right) \tag{3.12}$$

$$\frac{\partial \boldsymbol{B}'}{\partial t} - S^{-1}\nabla^2\boldsymbol{B}' = \nabla\times\left[\boldsymbol{u}\times\left(\boldsymbol{B}' + \boldsymbol{B}_0\right)\right] \tag{3.13}$$

To close the equations we have the incompressibility of the velocity field and the solenoidal constraint on the perturbed part of the magnetic field,

$$\nabla\cdot\boldsymbol{u} = 0, \qquad \nabla\cdot\boldsymbol{B} = 0. \tag{3.14}$$

The boundary conditions are to be no-slip, $\boldsymbol{u}|_{wall} = 0$, for the velocity. For the magnetic perturbation, the poloidal component and the component normal to the wall vanish, $B'_{P_{wall}} = B'_{\perp_{wall}} = 0$, while the toroidal component is free. The normal component $B_\perp$ vanishing at the wall physically corresponds to perfectly conducting boundary conditions. The zero poloidal fluctuations $B'_{P_{wall}}$ are imposed for numerical convenience. Since the perturbed magnetic field remains small compared to the field $\boldsymbol{B}_0$ in the present investigation, we do not think that this simplification significantly influences the results.

The initial condition for the simulations is zero magnetic perturbations and zero velocity. The simulations are carried out on a cubic domain of size $(2\pi)^3$ for the asymmetric and $(2\pi\times 2\pi\times\pi)$ for the symmetric cross section consisting of 256^3 grid points. We fix the penalization parameter to $\eta = 5\cdot 10^{-4}$. The time step is adaptive and the chosen CFL coefficient is 0.1.

3 RESULTS AND DISCUSSION

The results are divided into four different parts. The first shows the solution of the simulations at a low viscous Lundquist number, where an illustration of the generation of toroidal velocities is presented. The second exposes the calculations at higher viscous Lundquist, where the flow behavior of the plasma changes towards a dominantly toroidal flow. In the third section we compare, at fixed transport coefficients, simulations carried out for different safety factors and in the fourth section we show the results when the toroidal magnetic field is reversed.

3.1 GENERATION OF TOROIDAL VELOCITIES AT LOW VISCOUS LUNDQUIST NUMBER

In this section the calculations are performed for a low viscous Lundquist number, $M = 23$, in the geometry with symmetric cross section and $q = 3.3$. All the results are presented when the system has reached a statistically stationary state.

Fig. 3.3 shows the presence of a poloidal flow, a pair of counterrotating vortices in the poloidal plane. In this case the flow topology is almost axisymmetric with respect to the Z-axis. To visualize more clearly the toroidal velocities and the double poloidal recirculation, the azimuthally averaged velocity field is presented in Fig. 3.4. We distinguish four different zones, where the toroidal velocity changes sign, and the already mentioned "double smoke ring". Indeed, in the limit of vanishing nonlinearity, Bates and Montgomery [6] showed analytically that the steady state solution is a pair of poloidally rotating vortices, aligned with the toroidal direction.

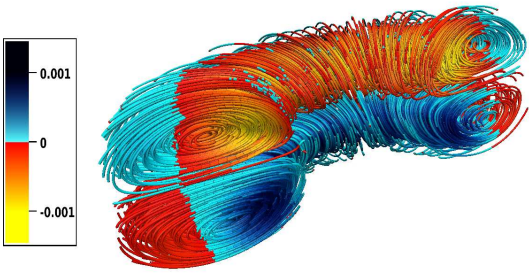

Figure 3.3: Streamlines colored with toroidal velocity (u_T) for $M = 23$.

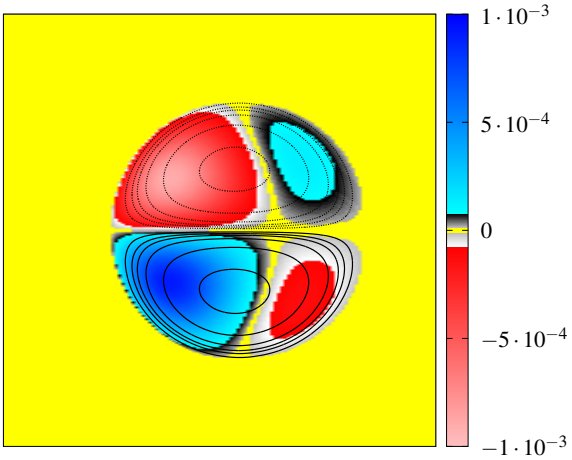

Figure 3.4: Azimuthally averaged toroidal velocity and poloidal stream function contours (solid line positive, dotted line negative contours).

The origin of toroidal velocities was demonstrated for vanishing viscous Lundquist in a rectangular cross section [50]. For a circular cross section and at low M number we will illustrate the generation of this velocity component. First, we illustrate that the forcing appearing in the vorticity equation (3.10) creates a toroidal vorticity with opposite sign

in relation to the mid-plane of the torus (see Fig. 3.5 (a)). This creates automatically a radial velocity that will interact with the imposed toroidal magnetic field (Fig. 3.5 (b)). The interaction will produce a perturbation to the toroidal magnetic field (B'_T). Notice that this magnetic field will have positive and negative areas located in a similar position as the radial velocity (Figs. 3.5 (b) and (c)). It was shown [50] that the equation giving the first order perturbed toroidal magnetic component $B_T^{\prime(1)}$ is,

$$\nabla^2(B_T^{\prime(1)}\boldsymbol{e}_T) \sim -u_R \frac{B_{T_{ref}}}{R^2}\boldsymbol{e}_T. \tag{3.15}$$

The sign of the right hand side, will only depend on the sign of u_R and of the imposed toroidal field $B_{T_{ref}}$.

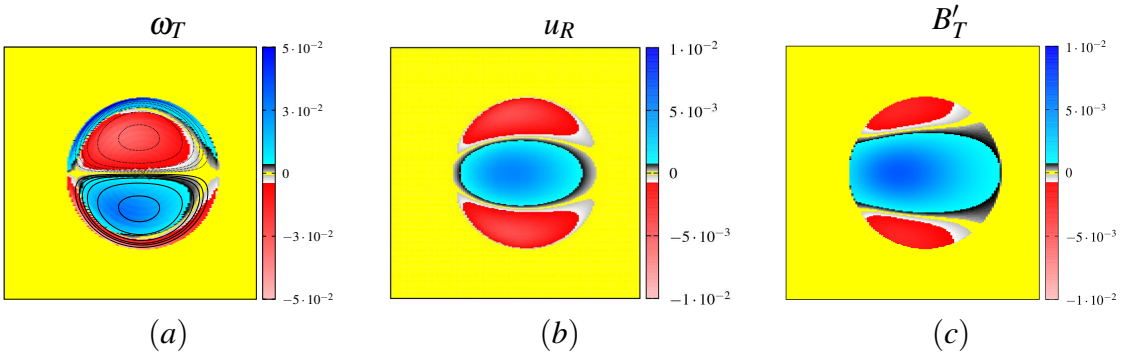

Figure 3.5: Azimuthally averaged: (a) Toroidal vorticity ω_T and poloidal stream function, (b) radial velocity u_R and (c) perturbation of the toroidal magnetic field, B'_T.

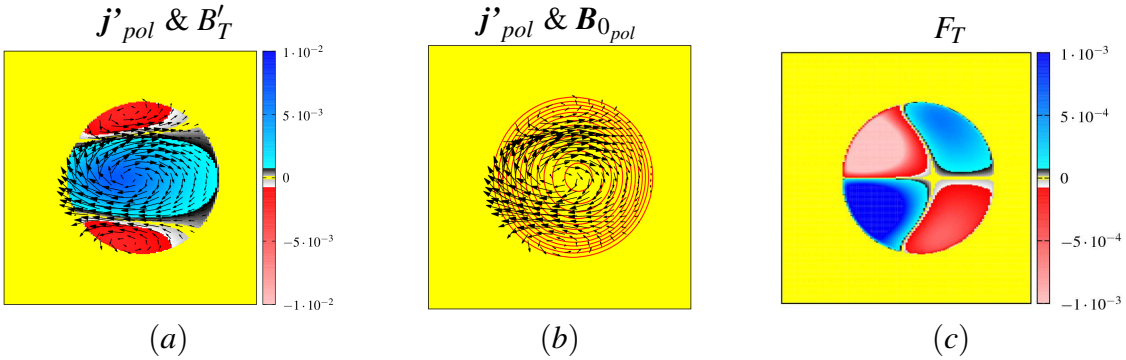

Figure 3.6: Azimuthally averaged: (a) Poloidal current density $\boldsymbol{j'}_{pol}$ (vectors) and perturbation of the toroidal magnetic field B'_T, (b) current density $\boldsymbol{j'}_{pol}$ (vectors) and imposed poloidal magnetic field lines $\boldsymbol{B}_{0_{pol}}$ and (c) toroidal Lorentz force F_T.

It follows that the curl of the perturbed toroidal magnetic field (B'_T) will produce a poloidal current density, $\boldsymbol{j'}_{pol} = \nabla \times B'_T$ (Fig. 3.6 (a)). The imposed poloidal magnetic field $\boldsymbol{B}_{0_{pol}}$ will then interact with the perturbed current density $\boldsymbol{j'}_{pol}$ to create a toroidal Lorentz force (see Figs. 3.6 (b) and (c)). The Lorentz force will finally induce toroidal

velocities. Note that there is a similarity in the negative and positive zones between the toroidal velocity and the toroidal Lorentz force fields (see Figs. 3.4 and 3.6 (c)). We note that the sign in the toroidal Lorentz force depends exclusively on the angle between $\boldsymbol{j'}_{pol}$ and $\boldsymbol{B}_{0_{pol}}$. As a consequence this angle influences directly the toroidal velocity direction.

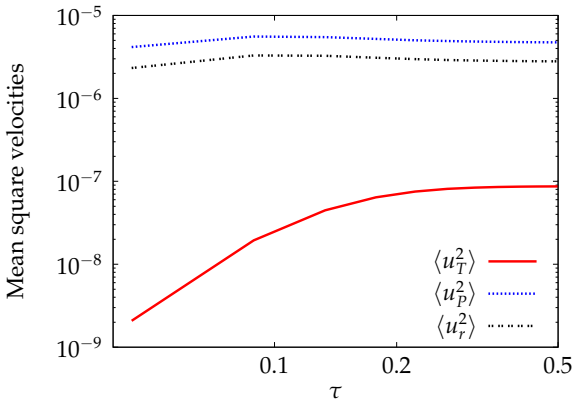

Figure 3.7: Poloidal and toroidal square velocity component evolutions at early times, in toroidal Alfvénic time units (τ).

Another way, to apprehend the fact that the poloidal flow interacts first with the magnetic field creating subsequently toroidal velocities, is to see the time evolution of the different velocity components. The velocities in the poloidal plane (in the poloidal direction P and in the minor radius direction r) grow first. After that the toroidal velocity is generated (see Fig. 3.7).

At low viscous Lundquist number the dominant velocities are in the poloidal plane and form two counterrotating vortices. Small toroidal velocities appear and they form a quadrupole with alternating positive and negative directions. The analytical results published by Bates and Montgomery [6] are in good agreement. Also the numerical generation of toroidal velocities agrees with the calculations made by Kamp *et al.* [50].

3.2 SIMULATIONS FOR HIGHER VISCOUS LUNDQUIST NUMBERS

In this section the calculations are made for the asymmetric cross section with fixed $q = 5.7$ and for the circular cross section, $q = 3.3$. The viscous Lundquist numbers are modified changing the transport coefficients ν and λ (with $Pr = 1$), keeping the geometry and the reference toroidal magnetic field unchanged, $B_{ref} = 1.2$.

With higher viscous Lundquist numbers it takes longer for the system to reach the saturated state. In the first instants an oscillatory behavior is present (see for example the different energy evolutions in Figs. 3.8 and 3.9). The kinetic and the fluctuating magnetic energy oscillate in opposition of phase, but these oscillations are damped out in a finite time. In the following section we will analyse and compare the different simulations when the system has reached this non-oscillatory steady state.

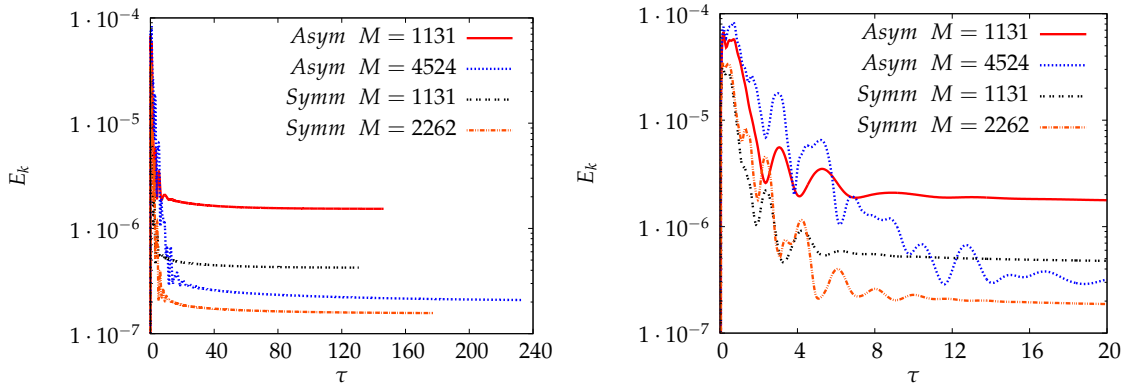

Figure 3.8: Kinetic energy evolution at large times (left) and oscillatory behavior at early time (right) in toroidal Alfvénic time units, for asymmetric and symmetric geometry.

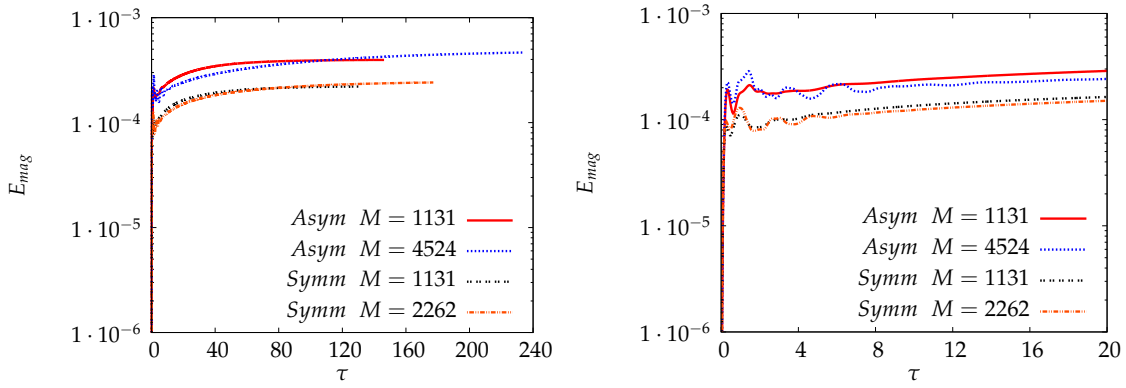

Figure 3.9: Fluctuating magnetic energy evolution at large times (left) and oscillatory behavior at early time (right) in toroidal Alfvénic time units, for asymmetric and symmetric geometry.

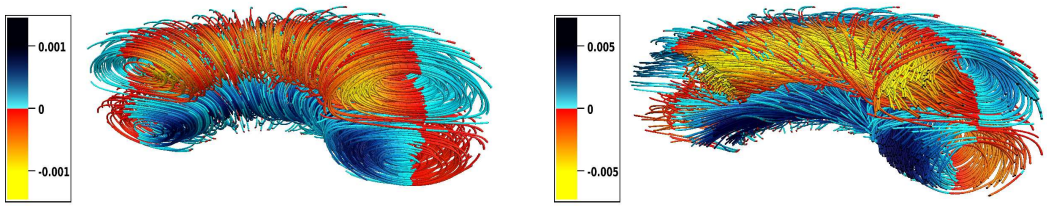

Figure 3.10: Streamlines colored with toroidal velocity (u_T) for $M = 23$ (left) and $M = 226$ (right) for the symmetric torus.

The calculations with increasing viscous Lundquist number show an important change in the fluid flow. The previously small toroidal velocities increase considerably and will

become more important, in magnitude, than the poloidal plane velocities. For nonzero nonlinearity, *i.e.*, by increasing M, the vortices start moving in the toroidal direction. The toroidal velocity increases with M in the two considered geometries. The three dimensional velocity streamlines show a substantial change of topology, from dominantly poloidal to dominantly toroidal flow (see Figs. 3.10 and 3.11).

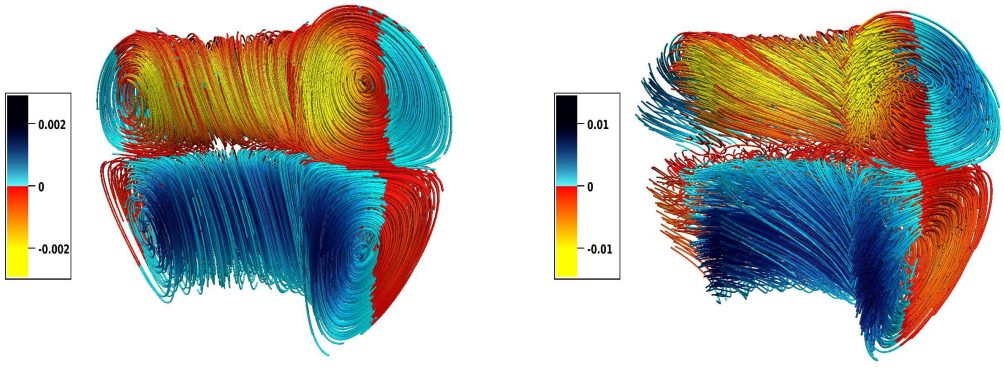

Figure 3.11: Streamlines colored with toroidal velocity (u_T) for $M = 23$ (left) and $M = 226$ (right) for the asymmetric torus.

The flow evolution is quantified in Fig. 3.12, where we observe that the principal direction of the flow is toroidal if M is raised beyond ~ 40. The square toroidal velocity saturates for increasing M at a value of $\sim 80\%$ of the total square velocity for the asymmetric cross section and at $\sim 60\%$ for the circular profile. This toroidal organization of the flow is consistent with the tendency of the velocity field to align with the magnetic field, as is illustrated in Fig. 3.13, where we compute the average (over the toroidal domain) of the absolute value of the cosine of the angle between the velocity and magnetic field. This quantity is equal to one if the velocity and the magnetic field are perfectly aligned or antialigned. The evolution of the ratio $\langle u_T^2 \rangle / \langle |\boldsymbol{u}^2| \rangle$ with M shows the same trend as the alignment between the magnetic and the velocity field.

An important difference is observed between the flows that are generated in the two geometries. The volume averaged toroidal angular momentum is defined by

$$\langle L_T \rangle = \frac{1}{V} \int_V R u_T dV. \tag{3.16}$$

For the torus with circular cross section, this quantity is zero to a good computational approximation ($< 10^{-15}$). The up-down anti-symmetry of the velocity field is responsible for this absence of toroidal angular momentum. However, for the torus with asymmetric cross section this is not the case. There is a symmetry breaking of the flow and the volume integral of the toroidal velocity is nonzero. In our calculations this can be visualized in the azimuthally averaged velocity fields in Fig. 3.14. It is more clear for the last case, at $M = 4524$, that the positive toroidal velocity occupies a larger part of the poloidal plane than the negative toroidal velocity. To quantify the amount of dissymmetry in the

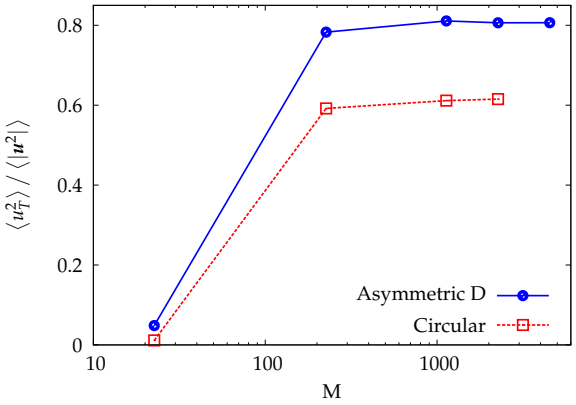

Figure 3.12: The ratio of the mean-square toroidal velocity to the total mean-square $\langle u_T^2 \rangle / \langle |\boldsymbol{u}^2| \rangle$ as a function of M.

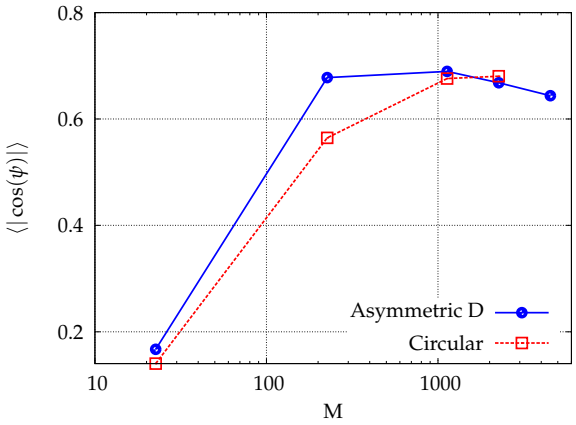

Figure 3.13: Average over the domain of the absolute value of the cosine of the angle between the velocity field and magnetic field.

flow we present the evolution of the normalized toroidal angular momentum with M (see Fig. 3.15). This quantity increases with the viscous Lundquist number. This up-down symmetry effect is in agreement with time-independent computations [51] and also with gyrokinetic simulations and experiments [16, 15].

Furthermore in Fig. 3.14 we can observe the two counterrotating vortices. They are still present at higher viscous Lundquist but undergo a deformation and their center is shifted outwards. The larger toroidal velocities concentrate near the boundaries as well as the poloidal speeds (this can be seen from the stream function isocontours that tend to converge near the boundaries). Nevertheless the velocity magnitude is globally less important for high M. In fact the kinetic energy has a maximum and then decreases if the viscous Lundquist number is raised (see Fig. 3.16). This behavior is explained by the decrease of the magnitude of the Lorentz force with the viscous Lundquist number in the center of the domain. Indeed, the plasma seems to self-organize to a state with a force-free region in the center, a behavior also observed for straight-cylinder computations at

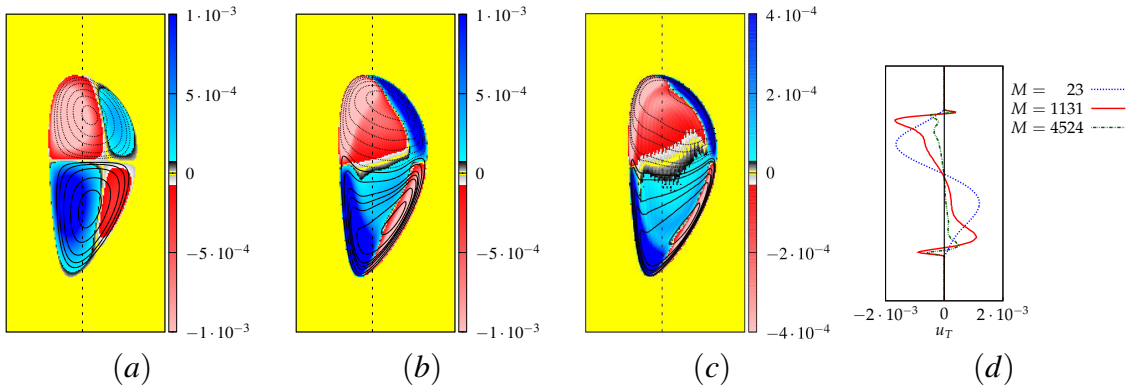

Figure 3.14: Azimuthally averaged flow visualizations: toroidal velocity u_T and poloidal stream function contours (solid line positive, dotted line negative contours) for $M = 23$ (a), $M = 1131$ (b) and $M = 4524$ (c). (d) Toroidal velocity profiles along a vertical cut. The position of these cuts is indicated in (a), (b) and (c) by a dotted vertical line.

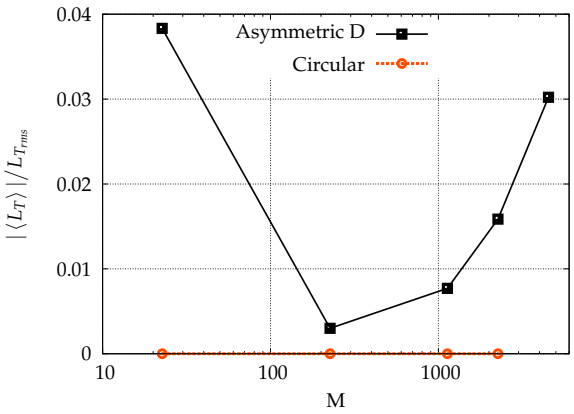

Figure 3.15: Normalized toroidal angular momentum $|\langle L_T \rangle| / L_{T_{rms}}$ as a function of M observed in the tori with asymmetric and symmetric cross section, respectively.

high pinch ratio [26].

The evolution with M of the root mean square (RMS) value of this force is presented in Fig. 3.17. The spatial distribution of the norm of the Lorentz force vector in the poloidal plane is visualized for the asymmetric geometry in Fig. 3.18. The vanishing of the Lorentz force in the core comes from the alignment between the magnetic and current density fields. A measure giving the alignment between these three-dimensional quantities is the volume-averaged current helicity defined as

$$H_j = \left\langle \frac{\boldsymbol{j} \cdot \boldsymbol{B}}{\| \boldsymbol{j} \| \| \boldsymbol{B} \|} \right\rangle . \tag{3.17}$$

We observe (Fig. 3.19) that for increasing viscous Lundquist number the global current density and magnetic field tend to be oriented in the same direction, the quantity in the figure approaches the unit value. This causes the Lorentz force term to decrease for higher

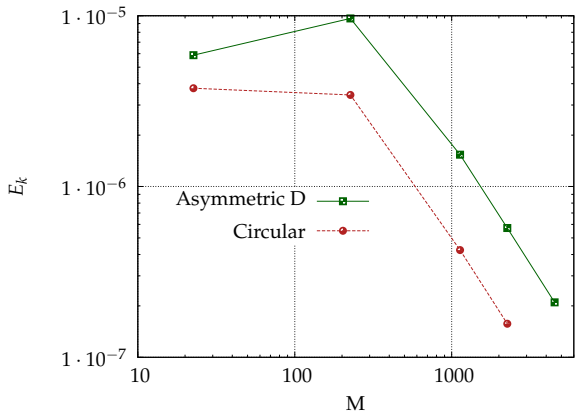

Figure 3.16: Kinetic energy as a function of M for the asymmetric and symmetric cross sections.

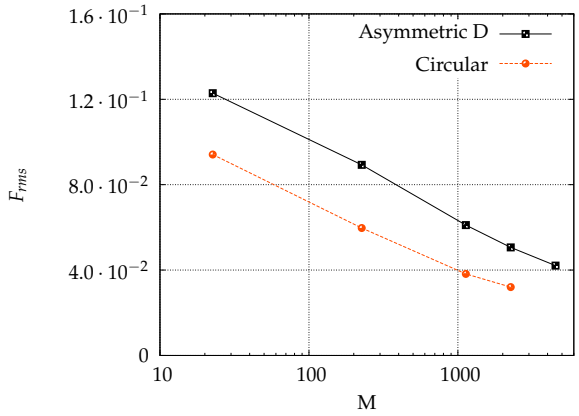

Figure 3.17: Root mean square value of the Lorentz force as a function of the viscous Lundquist number.

M in the center of the domain, the magnitude of the imposed toroidal current density and magnetic fields remaining constant.

Mainly, the variation of the alignment between $\boldsymbol{j}$ and $\boldsymbol{B}$ occurs in the poloidal plane. To quantify the alignment among the poloidal current density and the poloidal magnetic field we compute the volume-averaged absolute value of the cosine of the angle between these two fields,

$$\langle |\cos\Phi| \rangle = \left\langle \frac{\left| \boldsymbol{j}_{pol} \cdot \boldsymbol{B}_{pol} \right|}{\| \boldsymbol{j}_{pol} \| \| \boldsymbol{B}_{pol} \|} \right\rangle, \tag{3.18}$$

where $\boldsymbol{J}_{pol}$ and $\boldsymbol{B}_{pol}$ are the projections of $\boldsymbol{J}$ and $\boldsymbol{B}$ on the poloidal plane. This quantity at low viscous Lundquist is smaller compared to the value of the current helicity at the same M number (see Figs. 3.19 and 3.20). With increasing viscous Lundquist the cosine of this angle grows and approaches unity. There is a stronger change in the alignment between the current density and magnetic field in the poloidal plane. This poloidal alignment makes the toroidal Lorentz force vanish in the core of the domain.

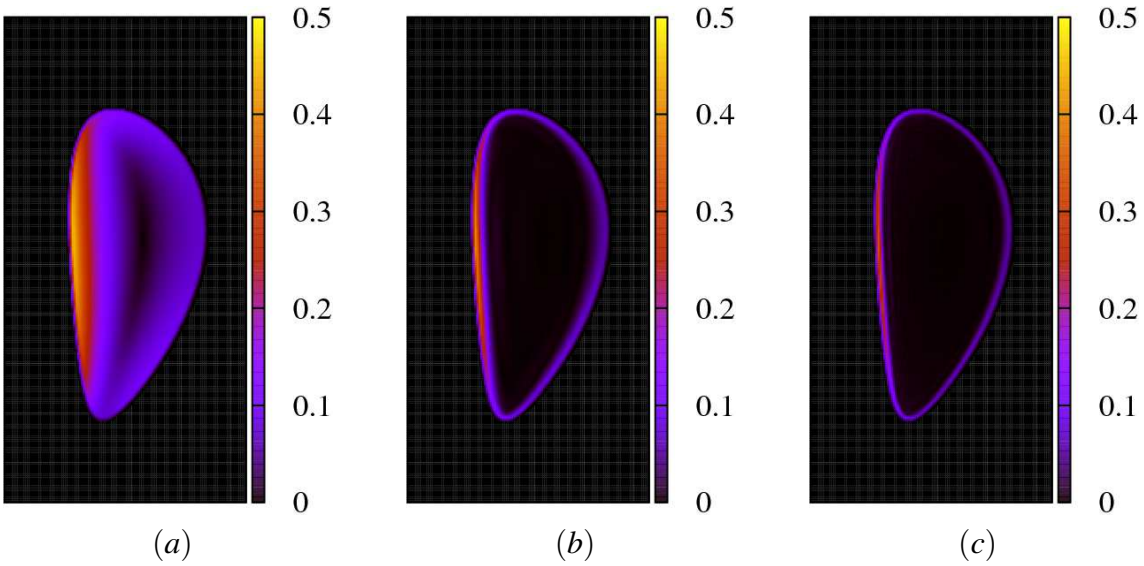

Figure 3.18: Azimuthally averaged vector norm of the Lorentz force for $M = 23$ (a), $M = 1131$ (b) and $M = 4524$ (c).

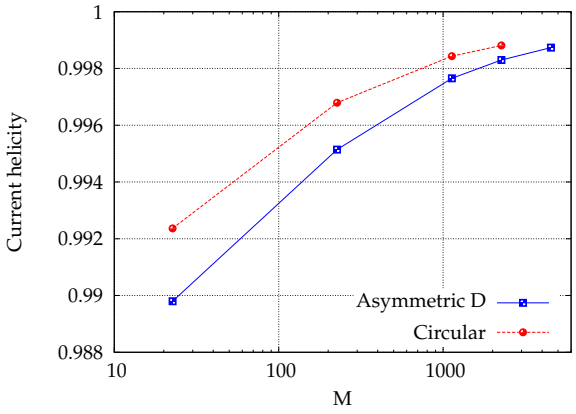

Figure 3.19: Current helicity as a function of M for the asymmetric and symmetric cross sections.

Whether or not the Lorentz force term reaches an asymptote at higher M or if a transition to another state exists remains an open question.

The system is almost axisymmetric around Z but small fluctuations around the toroidally averaged fields exist, defined as

$$\tilde{\boldsymbol{u}} = \boldsymbol{u} - \langle \boldsymbol{u} \rangle_T, \qquad \tilde{\boldsymbol{B}}' = \boldsymbol{B}' - \langle \boldsymbol{B}' \rangle_T. \tag{3.19}$$

The most important normalized fluctuations around the axisymmetric state are in the velocity field (Fig. 3.21), they are localized at the boundaries (see Fig. 3.23). The evolution of the normalized kinetic and magnetic fluctuations as a function of the viscous

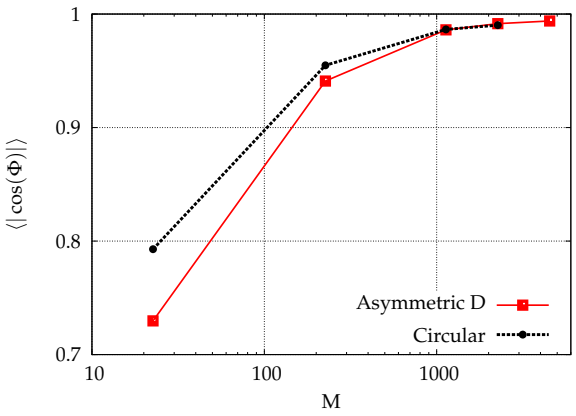

Figure 3.20: Volume-averaged absolute value of the cosine of the angle between the poloidal current density ($\boldsymbol{j}_{pol}$) and the poloidal magnetic field ($\boldsymbol{B}_{pol}$).

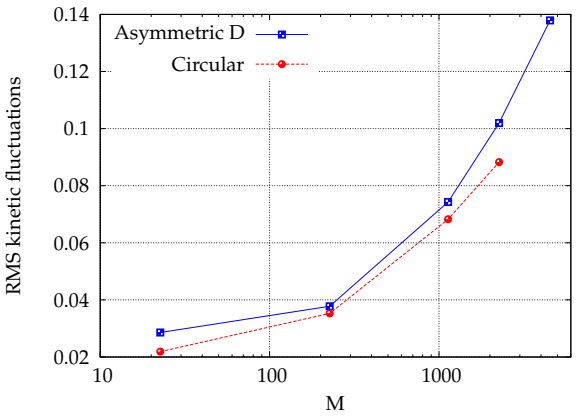

Figure 3.21: RMS value of the non azimuthally symmetric velocity fluctuations, normalized by the total root mean square velocity.

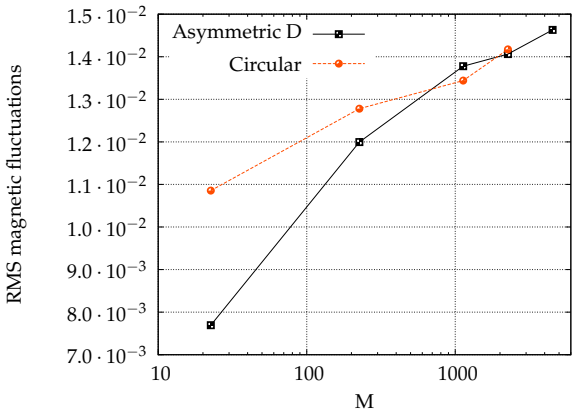

Figure 3.22: RMS value of the non azimuthally symmetric magnetic fluctuations, normalized by the total root mean square perturbed magnetic field.

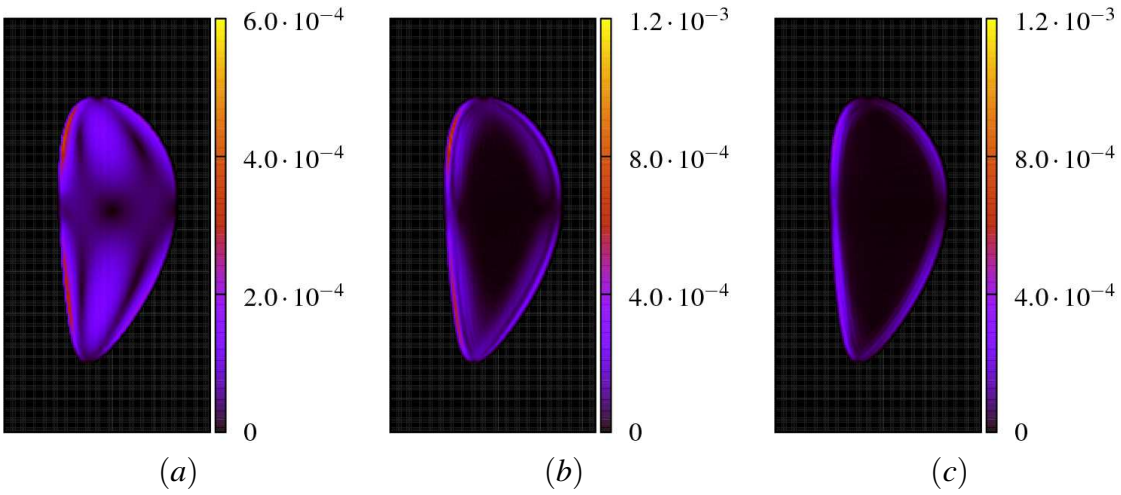

Figure 3.23: Azimuthally averaged square velocity fluctuations around the azimuthal mean value for $M = 23$ (a), $M = 1131$ (b) and $M = 4524$ (c).

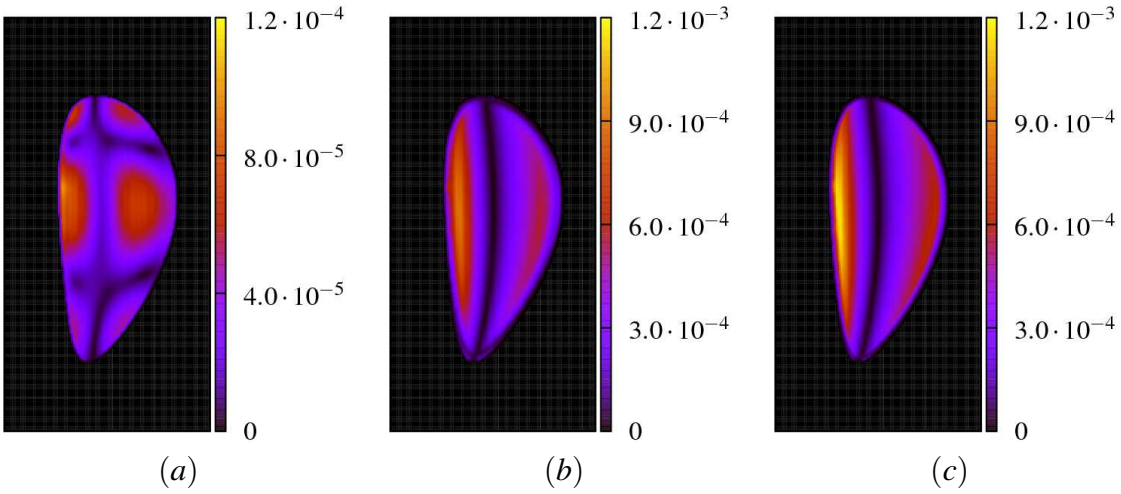

Figure 3.24: Azimuthally averaged square magnetic fluctuations around the azimuthal mean value for $M = 23$ (a), $M = 1131$ (b) and $M = 4524$ (c).

Lundquist number are presented respectively in Figs. 3.21 and 3.22. For the highest viscous Lundquist, $M = 4524$ and asymmetric cross section, we have the maximum ratio $\tilde{\boldsymbol{u}}_{rms}/\boldsymbol{u}_{rms} \sim 0.14$. The greatest normalized departure from axisymmetry for the perturbed magnetic field is also at $M = 4524$ for the 'D' cross section, $\tilde{\boldsymbol{B}}'_{rms}/\boldsymbol{B}'_{rms} \sim 0.015$. In fact for the magnetic field, the fluctuations are of the same order of magnitude as the velocity field, but the magnitude of the perturbed magnetic field is larger, hence the normalized quantities are smaller. The distribution of the perturbations in the two-dimensional plane (Figs. 3.23 and 3.24) show the velocity fluctuations mainly concentrated at the boundaries. These are the areas where the velocity is peaked (see e.g. velocity profiles Fig. 3.14 (d)) and where the velocity gradients are important. For the magnetic field the fluctua-

tions are spread in a larger region, they are more important at the high and low field side of the torus.

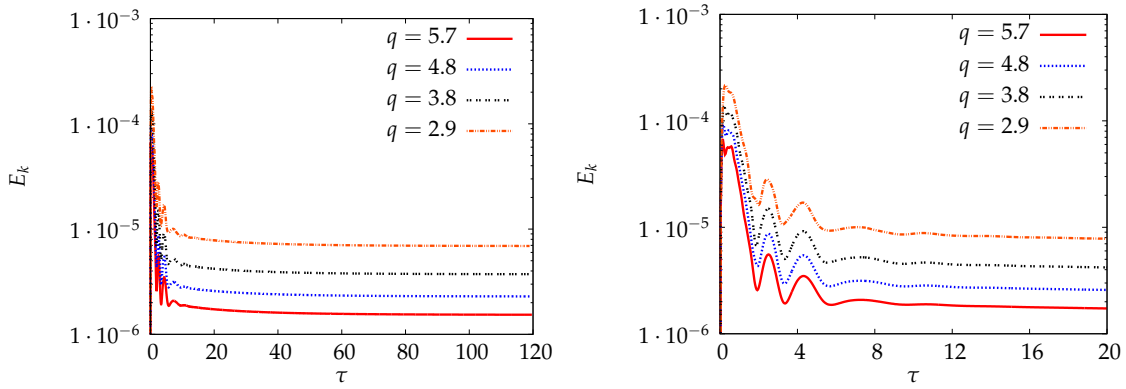

Figure 3.25: Left: kinetic energy evolution. Right: a zoom on the early time instants. Time is given in toroidal Alfvénic time units.

3.3 INFLUENCE OF THE SAFETY FACTOR ON THE DYNAMICS

The study of the influence of the safety factor q is presented in this section where we consider only the asymmetric cross section geometry and the transport coefficients are kept constant ($\nu = \lambda = 2 \cdot 10^{-3}$). We recall that for all the simulations presented in this manuscript the magnetic Prandtl number is equal to one, $Pr = 1$. In this case the viscous Lundquist number varies because the reference magnetic field used for its calculation is the imposed toroidal component and to modify the safety factor the magnitude of this field is changed, as also done in experiments [92, 93]. The parameter q takes four different values. We recall that the safety factor is defined as the ratio between the wall-averaged toroidal and poloidal imposed magnetic fields,

$$q = \frac{\overline{rB_{0_T}|_{wall}}}{R_0\overline{B_{0_P}|_{wall}}}. \tag{3.20}$$

The values of the viscous Lundquist number associated to each safety factor are presented in Tab. 3.1.

q	5.7	4.8	3.8	2.9
M	1131	942	754	565

Table 3.1: Corresponding viscous Lundquist number for each safety factor value.

The evolution of the total kinetic energy and the magnetic energy of the perturbation is similar for all the studied cases (see Figs. 3.25 and 3.26). The main difference is the

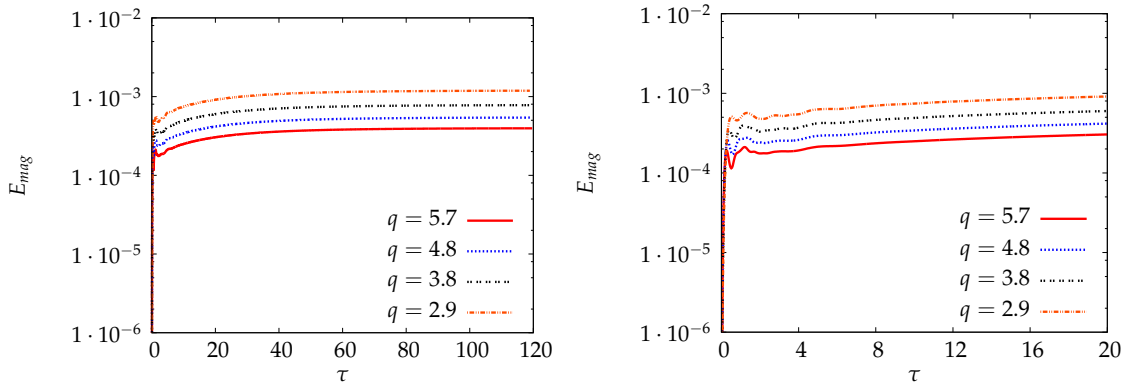

Figure 3.26: Left: perturbed magnetic energy evolution. Right: a zoom on the early time instants. Time is given in toroidal Alfvénic time units.

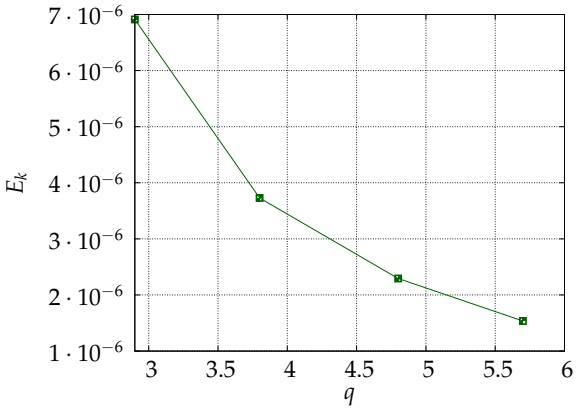

Figure 3.27: Kinetic energy as a function of q.

magnitude of the energies that is higher if the safety factor is small. At the steady state the dependence of the kinetic energy on the safety factor is visualized in Fig. 3.27.

The growth of the kinetic energy with decreasing q is in agreement with the reduction of the current helicity value (Fig. 3.28). Hence the Lorentz force term is stronger for a low safety factor. It is also observed that in the toroidal direction the Lorentz force increases, since the alignment between the poloidal current density and the poloidal magnetic field is less important for small q (Fig. 3.29). This variation is smaller compared to the variation caused by the transport coefficients modification, as shown in Sec. 3.2.

As in the previous section the toroidal velocity dominates, but the ratio $\langle u_T^2 \rangle / \langle |\boldsymbol{u}^2| \rangle$ decreases with decreasing q (Fig. 3.30). Also the alignment between the magnetic and velocity field is less important (inset Fig. 3.30).

An important feature is the change of sign in the volume averaged toroidal angular momentum, found also in experimental observations [92, 93, 97], when the toroidal magnetic field, hence the safety factor, is varied (Fig. 3.31). In our case the averaged angular momentum changes completely in sign, it passes from negative to positive for increasing

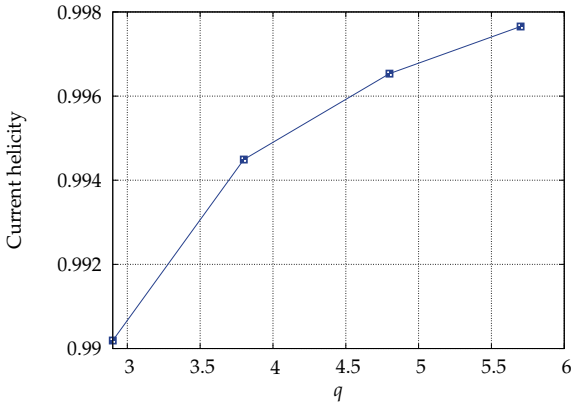

Figure 3.28: Current helicity as a function of the safety factor q.

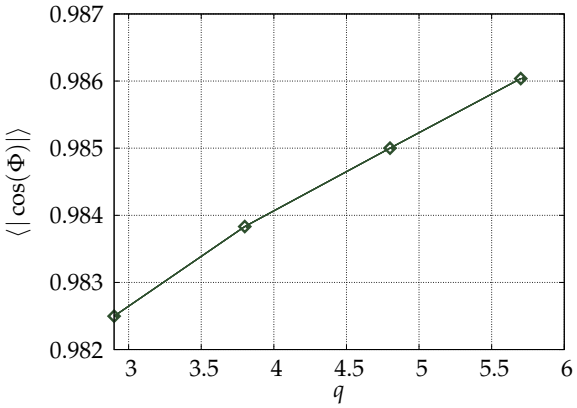

Figure 3.29: Volume-averaged absolute value of the cosine of the angle between the poloidal current density ($\boldsymbol{j}_{pol}$) and the poloidal magnetic field ($\boldsymbol{B}_{pol}$).

q. The two-dimensional azimuthally averaged toroidal velocities (Fig. 3.32) show the increase of the area in which the toroidal velocity is negative when the safety factor is decreased. For the lowest value of q that we consider, the vertical cut (Fig. 3.32 (d)) shows larger velocities and a small downward shift of the position where the toroidal velocity changes sign. This displacement enlarges the negative velocity area. The growth of the negative toroidal velocity is better visualized in the cuts along the direction of the big radius (Fig. 3.33). For decreasing q the velocities tend to be more peaked and near the center of the torus a region appears where the toroidal velocity is negative. We notice that the change of sign of the toroidal velocity mainly occurs in the center of the geometry. Close to the boundaries the toroidal component grows but does not reverse sign.

As presented in the previous section small fluctuations around the azimuthal average exist. We see in Fig. 3.34 that the magnitude of these fluctuations is relatively insensitive to the value of the safety factor. The change is just of a few percent for the normalized

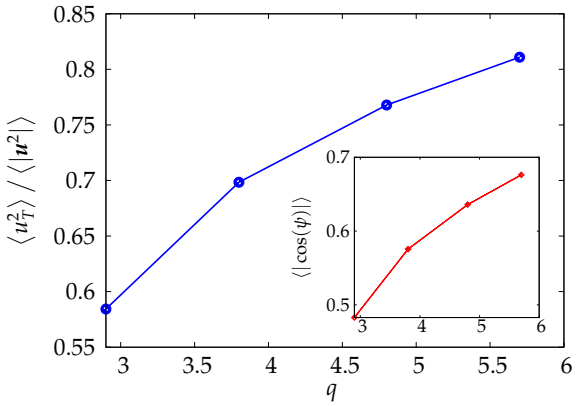

Figure 3.30: The ratio of the mean-square toroidal velocity to the total mean-square $\langle u_T^2 \rangle / \langle |\boldsymbol{u}^2| \rangle$ as a function of q. In the inset we show the average over the domain of the absolute value of the cosine of the angle between the velocity field and magnetic field.

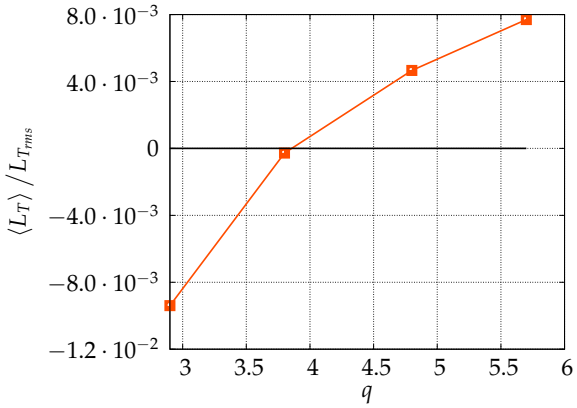

Figure 3.31: Normalized toroidal angular momentum $\langle L_T \rangle / L_{T_{rms}}$ as a function of q.

velocity fluctuations. It is larger for the normalized magnetic fluctuations, but it remains below $\sim 20\%$ (Fig. 3.35). Hence the safety factor variation, in the considered range, does not increase substantially the non-axisymmetric perturbations.

3.4 INFLUENCE OF THE REVERSAL OF THE IMPOSED TOROIDAL MAGNETIC FIELD

The simulation with inverted toroidal magnetic field is performed for $q = 5.7$ and $M = 1131$. The results show that the velocity reverses sign in the whole domain (Fig. 3.36). The counterrotating poloidal vortices are unchanged, only the toroidal velocities are affected. In Fig. 3.36 (c) the profiles are exactly symmetric with respect to the vertical axis. Basically, what happens is that the perturbed toroidal magnetic field reverses its sign and this generates an inverse poloidal current density. The existing poloidal magnetic field associated with the inverted poloidal current density field gives an opposite toroidal Lorentz

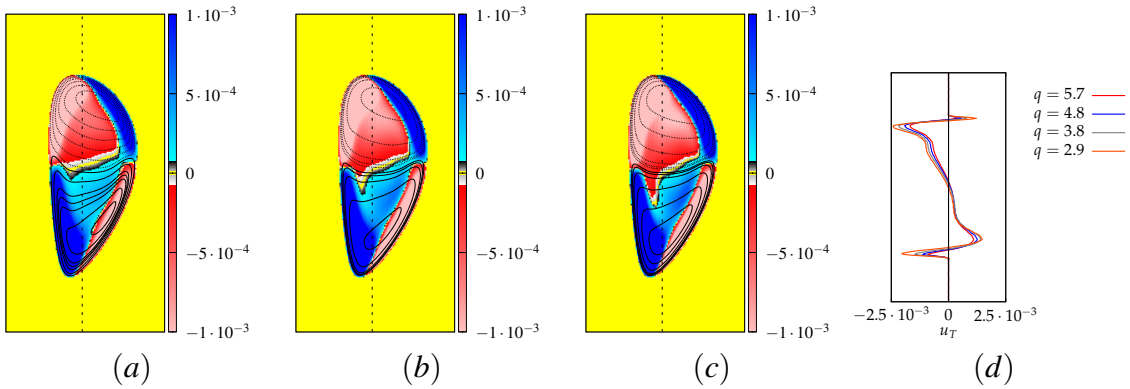

Figure 3.32: Azimuthally averaged flow visualizations: toroidal velocity u_T and poloidal stream function contours (solid line positive, dotted line negative contours) for $q = 5.7$ (a), $q = 3.8$ (b) and $q = 2.9$ (c). (d) Toroidal velocity profiles along a vertical cut. The position of these cuts is indicated in (a), (b) and (c) by a dotted vertical line.

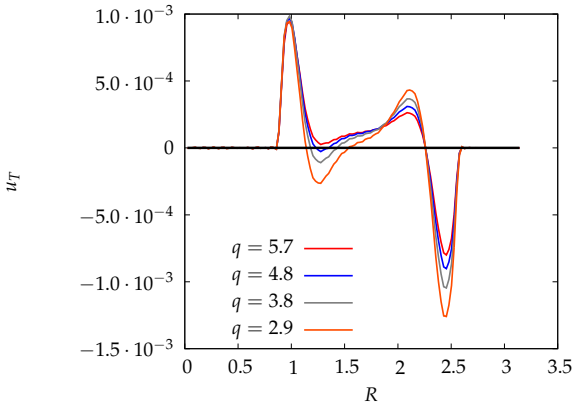

Figure 3.33: Toroidal velocity profiles along a horizontal cut, at the center of the domain.

force. Finally, this Lorentz force will make the toroidal velocities reverse in all the domain. We can write the three components of the Lorentz force in cylindrical coordinates:

$$\begin{cases} F_R = j_T B_Z - \frac{1}{R}\frac{\partial (RB_T)}{\partial R} B_T, \\ F_T = \frac{\partial B_T}{\partial Z} B_Z + \frac{1}{R}\frac{\partial (RB_T)}{\partial R} B_R, \\ F_Z = -\frac{\partial B_T}{\partial Z} B_T + j_T B_R. \end{cases} \tag{3.21}$$

The inversion of the sign of B_T transforms the original Lorentz force vector (F_R, F_T, F_Z) into $(F_R, -F_T, F_Z)$. Only the toroidal component is affected. Hence the poloidal velocities are unchanged but the toroidal velocities are inverted.

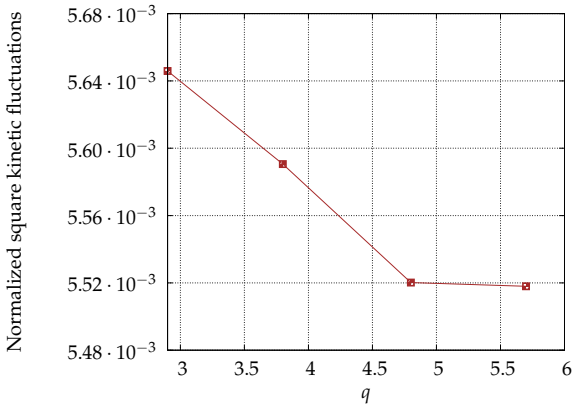

Figure 3.34: Square velocity fluctuations normalized by the total square velocity.

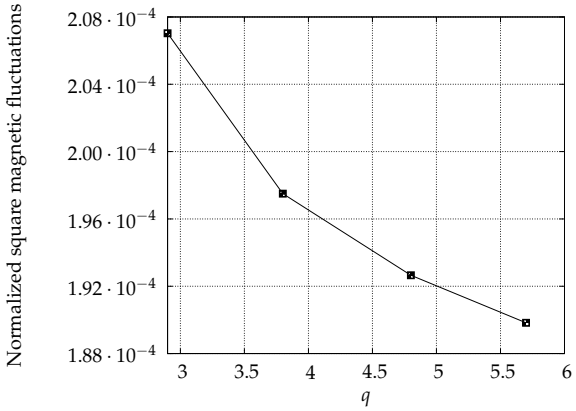

Figure 3.35: Square magnetic fluctuations normalized by the total square perturbed magnetic field.

4 CONCLUDING REMARKS ABOUT THE GENERATION OF VELOCITIES IN TOROIDAL GEOMETRIES

In this chapter it was demonstrated numerically, solving the fully nonlinear time-dependent resistive MHD equations, that in a toroidal geometry, assuming constant transport coefficients, if the imposed toroidal magnetic and toroidal electric fields are irrotational, the conducting flow inside a torus necessarily moves. The reason for this is that the curl of the Lorentz force resulting of the imposed fields is nonzero. It follows that the gradient of a scalar (in this case the pressure) can not balance the equation. Consequently vorticity is created. This vorticity in the toroidal direction creates poloidal velocities. The poloidal velocities interact with the imposed toroidal magnetic field creating a perturbation that gives rise to a poloidal current density. This current density associated with the existing poloidal magnetic field produces a toroidal Lorentz force. As a consequence toroidal velocities appear. The angle between the poloidal current density and poloidal magnetic field plays an important role in the determination of the toroidal velocity direction.

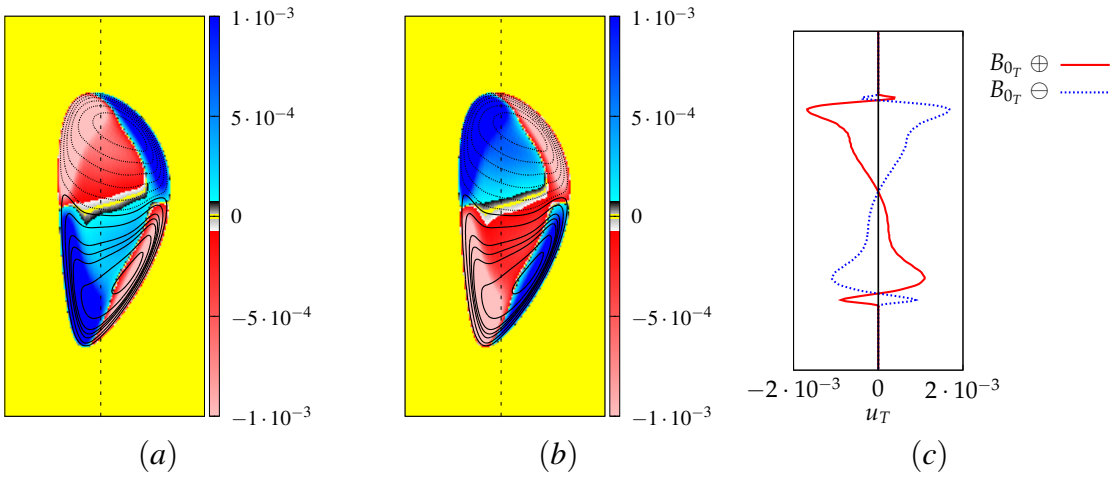

Figure 3.36: Azimuthally averaged flow visualizations: toroidal velocity u_T and poloidal stream function contours (solid line positive, dotted line negative contours) for imposed positive B_{0_T} (a) and negative B_{0_T} (b). (c) Toroidal velocity profiles along a vertical cut. The position of these cuts is indicated in (a) and (b) by a dotted vertical line.

For a low viscous Lundquist number the system tends to produce small toroidal velocities, the dominant flow being a pair of counterrotating vortices in the poloidal plane. A dramatic change occurs when the viscous Lundquist number is increased. There is a transition from a dominantly poloidal to dominantly toroidal flow. This transition is in agreement with the tendency of the velocity field to align with the magnetic field.

Two different toroidal geometries are considered in the present study, one with an up-down symmetric and the other with an asymmetric cross section. A fundamental difference exists between both studied cases: the volume-averaged angular momentum is zero for the symmetric case, while for the asymmetric cross section a finite volume-averaged angular momentum appears. There is a breaking in the up-down symmetry of the flow and a toroidal preferred direction emerges. This volume-averaged normalized angular momentum tends to increase with the viscous Lundquist number.

Nevertheless the kinetic energy decreases with increasing nonlinearity, since the total magnetic and current density fields tend to align in the center of the domain. The limitation in the numerical resources prevents the study of this system for larger viscous Lundquist numbers. It remains an open question if there will be a continuous increase of the alignment between the magnetic and current density field or if a transition exists.

When the safety factor is decreased while maintaining the transport coefficients constant, the kinetic and fluctuating magnetic energy become higher. The main qualitative effect is the influence on the toroidal velocity direction. There is a change in the volume-averaged angular momentum that reverses sign. For low q it is negative and at large safety factor it becomes positive. Mainly in the center of the domain, for decreasing q, the region in which the velocity is negative becomes larger, at expense of the region with positive toroidal velocity. Near the boundaries the toroidal velocity direction remains unchanged.

The last part of the chapter was dedicated to the influence of the reversal of the toroidal magnetic field. It is shown that it plays a role only in the toroidal velocities. The reversal changes the sign of the poloidal current density, that gives rise to the toroidal Lorentz force. In consequence the toroidal force reverses in the whole volume making the toroidal velocities reverse their direction compared to the original case.

IV

MAGNETOHYDRODYNAMICS FOR HIGH PINCH RATIOS IN TOROIDAL AND CYLINDRICAL GEOMETRIES

1 INTRODUCTION

The Reversed Field Pinch (RFP) is characterized by pinch ratios bigger than unity. This device, together with the tokamak and the stellarator, is one of the magnetic fusion configurations that could achieve thermonuclear fusion. A practical advantage of the RFP as compared to the tokamak geometry is that to confine the plasma the RFP needs a smaller externally imposed magnetic field. The toroidal field is enhanced through the self-organization of the plasma in the center, via a dynamo mechanism induced by the plasma itself, and decreases at the plasma edge. The reduction of the toroidal field can be very large and the value at the edge can reverse sign.

The dynamo mechanism can be explained if we consider the following simple example which we adopted from Escande *et al.* [31]. Let us consider a wire placed in the interior of a solenoid (Fig. 4.1). The current in the wire and the magnetic field created by the solenoid are in the same direction. If this wire is exactly at the geometrical center, it is in unstable equilibrium, because the currents in the solenoid attracting the wire radially compensate one another. If this wire is deformed by a small perturbation, it will bend, forming a helical geometry that will follow the original solenoid. As a consequence there is a second 'solenoid' which is created in the interior of the first one. This second winding will produce a magnetic field in the same direction as the original in the center, but it will induce an opposite magnetic field on its exterior. In the center it will therefore enhance

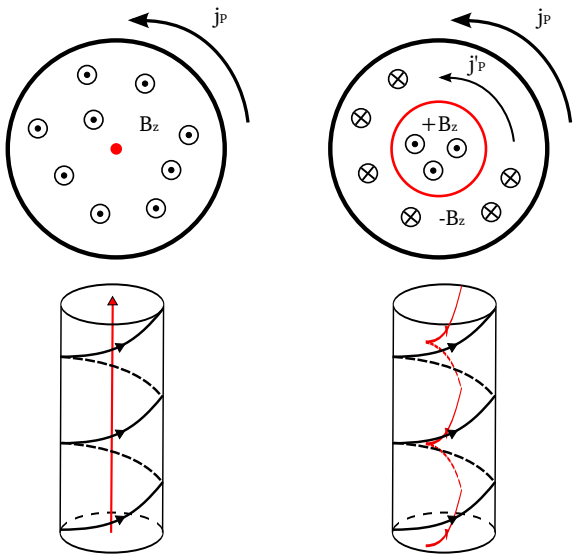

Figure 4.1: Wire model (top view): (left) initial position of the current-carrying wire (red) surrounded by the solenoid with poloidal current j_P and (right) development of the perturbed poloidal current density, j'_P (when the wire in the center is kinked) with enhancement of the axial magnetic field in the center ($+B_z$) and decrease at the edge ($-B_z$).

the magnetic field but near the edges the magnetic field is decreased and can even reverse sign.

As a consequence of the high pinch ratio, magnetohydrodynamic instabilities such as the above discussed kink-instability appear in the RFP, which increase the turbulence and lower the energy confinement performance. Generally this chaotic regime is called multiple-helicity (MH) state because a multitude of helically extended modes interact. However in the last decades quasi-single helicity (QSH) states were observed in experiments where the full turbulent regime is avoided and one helical mode predominates above the others [32, 61, 77, 14, 96]. In the QSH state there is a decrease of magnetic chaos and the formation of a coherent helical structure within the plasma. The reduction of particle transport has been observed in QSH states with respect to MH states [34, 87, 37]. Also it has been found that increasing the toroidal current makes the QSH regime more persistent [62, 57, 56]. The QSH state is responsible for the creation of internal transport barriers (ITB) that improve the confinement time by a factor of two [23, 85]. It has also been discovered relatively recently that external transport barriers (ETB) are created for low plasma densities that increase in 30% the confinement time. The origin of this barrier is not well understood but it could be related to a shear flow [88].

The majority of numerical studies of the RFP, using the MHD approximation, consider periodic cylindrical geometries, ignoring the influence of the curvature of the magnetic field. In the eighties the first MHD calculations were performed using the non-viscous MHD model (see e.g. [26, 4]) and in the nineties viscoresistive calculations were performed [102, 101, 100]. In the last decades the viscoresistive MHD model

has been taken into account using a constant-pressure constant-density approximation (*SpeCyl* code) [21, 18, 8, 108]. Also in a cylinder, but using the full compressible viscoresistive MHD equations, the effect of the compressibility has been studied for a constant uniform [79, 80] and nonuniform resistivity [78].

Three dimensional codes solving the MHD equations exist, but there is not yet, at our knowledge, a complete study of the dynamics of a toroidal magnetofluid in the RFP context. A recent three dimensional code with a toroidal geometry implementation (*PIXIE3D*) has been compared with the cylindrical *SpeCyl* code [9, 20]. Also, a MHD toroidal code (*MIPS*) has been used to study the dynamics of the RFP RELAX [66].

In this chapter we study the helical plasma configurations using the viscoresistive MHD model in a torus and in a periodic cylinder. In general in real experiments the β_P (average ratio of the plasma pressure over the poloidal magnetic pressure, $2\langle P\rangle/B_P^2(a)$) is considerably below unity so it is believed that the toroidal outward shift of the magnetic surfaces is small such that equilibrium and stability are well described in a cylindrical approximation. Here we perform cylindrical and toroidal simulations to find out if there are important changes between these two geometries and if the cylindrical approximation can be justified.

First we discuss, in Sec. 2, the results of simulations in toroidal geometry. We investigate in some detail the transition from an axisymmetric state towards different helical regimes in a toroidal geometry. The pinch ratio of the imposed magnetic field will be varied and we will consider two different viscous Lundquist numbers. For the cylindrical case (Sec. 3) the self-organisation of the magnetofluid is investigated. As for the toroidal geometry, the pinch ratio is varied and two viscous Lundquist numbers are considered. In Sec. 4 a comparison is made between the toroidal and cylindrical results, where it is shown that even if the two configurations share some characteristics, a fundamental difference between the two flows exist, in particular when the torus and cylinder results are compared with experimental data (Sec. 4.2).

2 TOROIDAL SIMULATIONS

In this section we will first briefly illustrate the RFP dynamo effect. Then the transition from an axisymmetric to a helical state with increasing pinch ratio is discussed. The toroidal mode energies at the steady state are presented as well as the velocity field topology and different volume averaged quantities as a function of the pinch ratio. Finally the time evolution of the different toroidal modes for the velocity field are assessed and the diversity of dynamics in this system are underlined.

The toroidal geometry has a minor radius $a = 0.3\pi$ and a big radius $R_0 = 0.55\pi$, the aspect ratio is $\Gamma = R_0/a \approx 1.83$ (Fig. 4.2). The size of the periodic box where the calculations are performed is $(2\pi \times 2\pi \times \pi)$. We fix the penalization parameter to $\eta = 5\cdot 10^{-4}$. The resolution for all the toroidal calculations is 128^3 grid points and we consider constant resistivity and viscosity. The dimensionless numbers characterising the system

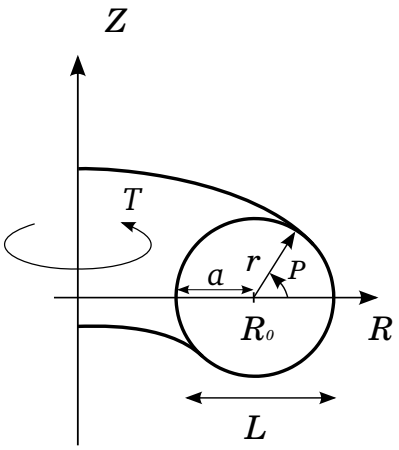

Figure 4.2: Toroidal circular geometry.

are four, two of them are the pinch ratio and the reversal parameter,

$$\Theta = \frac{\overline{B_P(a)}}{\langle B_T \rangle}, \qquad F = \frac{\overline{B_T(a)}}{\langle B_T \rangle}, \tag{4.1}$$

with a the small radius. The remaining two are the viscous Lundquist number and the magnetic Prandtl number,

$$M = \frac{C_A L}{\nu}, \qquad Pr = \frac{\nu}{\lambda}, \tag{4.2}$$

with C_A the poloidal Alfvén velocity, as reference length we take the diameter $L = 0.6\pi$, ν the viscosity and λ the magnetic diffusivity. We vary the viscous Lundquist number (M) with constant magnetic Prandtl number (Pr) and evaluate the system as a function of the pinch ratio at the final state (Θ).

The imposed magnetic field for the toroidal geometry has the same topology as the one in the previous chapter. The imposed current in the center of the domain at $R = R_0$ (Fig. 4.2) is fixed at, $J_0 = 1$. The poloidal magnetic field is calculated with a precalculation as presented in Appendix D.

To vary the pinch parameter (Θ) numerically, we modify the toroidal magnetic field. Here we recall the profile of this quantity,

$$B_{0_T} \propto \frac{R_0}{R} \boldsymbol{e}_T. \tag{4.3}$$

The imposed poloidal component of the magnetic field is kept constant. For the toroidal calculations presented in this chapter the reference magnetic field (B_{ref}) is the surface averaged poloidal magnetic field at the boundaries, $B_{ref} = \overline{B_P(a)} = 0.35$. This value of B_{ref} is invariant for all the toroidal simulations.

2.1 DYNAMO EFFECT AND TRANSITION TO A HELICAL STATE

The toroidal simulations are started with zero velocity field and zero magnetic perturbations, and we fix the magnetic Prandtl number to $Pr = 3$. This value of the Prandtl number is chosen because $Pr > 1$ is expected to be found in fusion plasmas and in previous numerical studies $Pr \in [1, 20]$ [18]. However, since the value of the viscosity in fusion plasmas is not so well defined, this choice should be considered of arbitrary nature and parametric studies on the influence of the Prandtl number constitute a very interesting perspective of the present investigation.

As shown in the previous chapter an axisymmetric flow develops, characterized by two counter-rotating vortices with their vorticity aligned with the toroidal direction. If the pinch ratio is increased an instability appears. This helical instability deforms the pre-existing axisymmetric state. This instability was absent in the previous chapter.

The instability consist in the growth of a helical-kink perturbation [31] with a toroidal mode number n. The value of this mode depends on the considered case: the variation of the diffusion coefficients and the pinch ratio modifies the value of the dominant toroidal mode.

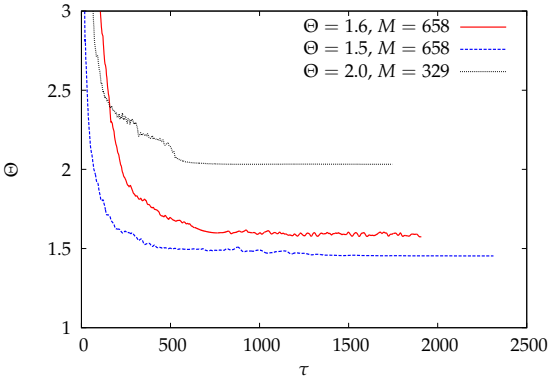

Figure 4.3: Pinch ratio evolution as a function of the poloidal Alfvén time.

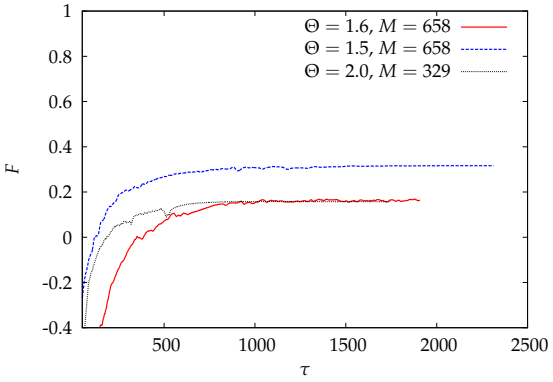

Figure 4.4: Reversal parameter evolution as a function of the poloidal Alfvén time.

After a linear phase the instability saturates through nonlinear effects and different dynamics in the time evolution of the system exist. The mode, that grows at the early stages of the nonlinear phase, can be damped leaving its place to other modes. Oscillatory behavior appears for high values of the viscous Lundquist number and pinch ratios, as will be shown later.

We now present the evolution of the volume averaged quantities for three different simulations. First we show the evolution of the pinch ratio and the reversal parameter, respectively, in Figs 4.3 and 4.4. From the Θ and F time evolution we can see the system reaching a steady state. Fluctuations in this state are present for the highest value of the viscous Lundquist number and pinch ratio. We note in Fig. 4.4 that at the steady state we do not have a complete reversal of the toroidal magnetic field at the edge, *i.e.*,

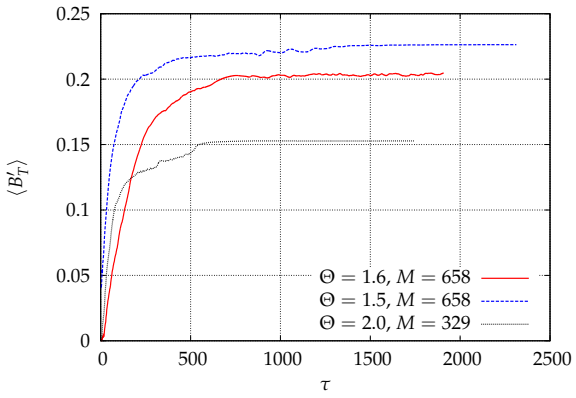

Figure 4.5: Perturbed toroidal component of the magnetic field as a function of the poloidal Alfvén time.

F remains positive. The reversal parameter has a transient period where it is negative but at the final times it grows and becomes positive for the considered cases. Notice that the Θ and F time evolution are similar. We can explain the evolution of these two quantities if we consider the dynamo effect that enhances the toroidal magnetic field. Fig. 4.5 shows the evolution of the perturbed toroidal magnetic field that is enhanced by the dynamo mechanism (phenomenon illustrated in Fig. 4.1). The increase of this self-generated magnetic field decreases the pinch ratio and at the same time increases the F parameter.

The dynamo mechanism will limit the maximum value that can be reached by Θ. Numerically, to rise the pinch parameter we decrease the imposed toroidal magnetic field (B_{0_T}). For B_{0_T} tending to zero, the generated toroidal magnetic field tends to a constant value. The perturbed toroidal component generated by the dynamo mechanism dominates the system if B_{0_T} is sufficiently decreased. As a consequence the steady state pinch ratio reaches an asymptote when the initial pinch ratio tends to infinity[†].

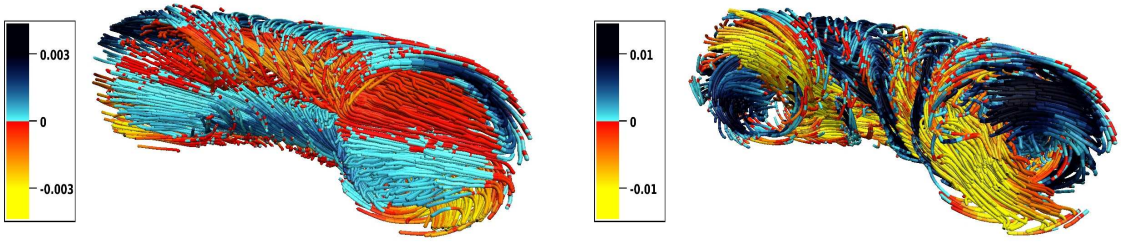

Figure 4.6: Velocity streamlines colored with the toroidal velocity for $M = 329$, $\Theta = 0.32$ (left) and $M = 658$, $\Theta = 1.45$ (right).

[†]An additional effect limiting the reversal of the toroidal magnetic field can be the periodicity condition imposed by our numerical method and we are currently investigating this. The outcome of the test and possible solution to the problem will be presented elsewhere.

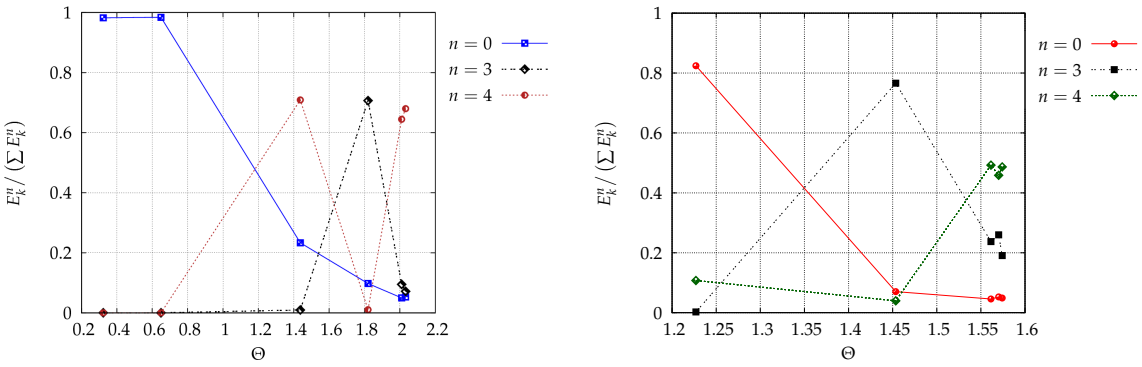

Figure 4.7: Ratio of the kinetic energy of the dominant toroidal modes over the total kinetic energy for the torus geometry, $M = 329$ (left) and $M = 658$ (right) as a function of Θ.

The transition to a dominant helical system appears for a pinch parameter superior to one. This phenomenon is visualized in Fig. 4.6. Here the color of the streamlines, representing the toroidal velocity, is azimuthally invariant (Fig 4.6 (left)). On the other hand, a helical deformation in the streamlines appears in Fig. 4.6 (right). This is a transition from a dominant axisymmetric state to a helical configuration. The streamlines form two helices, one with positive and the other with negative toroidal velocity. The energy contained in the different toroidal modes allows us to highlight this transition. In Fig. 4.7 (left) is presented the ratio of the energy of the 0, 3 and 4 toroidal modes over the total energy, for a viscous Lundquist number $M = 329$. It is shown that for a pinch ratio inferior to unity the energy is contained in the zero toroidal mode (the axisymmetric field). For a value of $\Theta \approx 1.4$ the zero mode is not longer dominant, the energy of the mode $n = 3$ contains $\sim 70\%$ of the total energy. For increasing pinch ratio there are two other states. The first for $\Theta \approx 1.8$ where the dominant mode is not longer $n = 3$ but $n = 4$, with also $\sim 70\%$ of the total energy. And for the highest pinch parameter ($\Theta \approx 2$) there is a regrowth of the $n = 3$ mode ($\sim 70\%$ of the total energy), the energy of the fourth mode being reduced.

For the highest viscous Lundquist number ($M = 658$), we have only considered Θ values larger than one (Fig. 4.7 (right)). As for the previous case we have the toroidal modes three and four that dominate alternatively. In this case for $\Theta \approx 1.45$, the dominant mode is $n = 3$ with $\sim 75\%$ of the total energy. And for the highest values of the pinch ratio, $\Theta \approx 1.57$, we have the $n = 4$ mode dominating with $\sim 50\%$ of the total energy. For this last case the energy is spread over a larger number of modes. Whether a completely turbulent state can be reached at higher values of the viscous Lundquist number remains an open question.

The helical modes, $n = 3$ and $n = 4$, dominating our system are visualized in Fig. 4.8 for different pinch parameter values but constant viscous Lundquist $M = 658$. In this figure a positive and a negative isocontour of the toroidal velocity are presented. Three and four lobes appear respectively, for $\Theta = 1.45$ and $\Theta = 1.57$.

Another visualization is presented in Fig. 4.9, where a perturbed magnetic isocontour

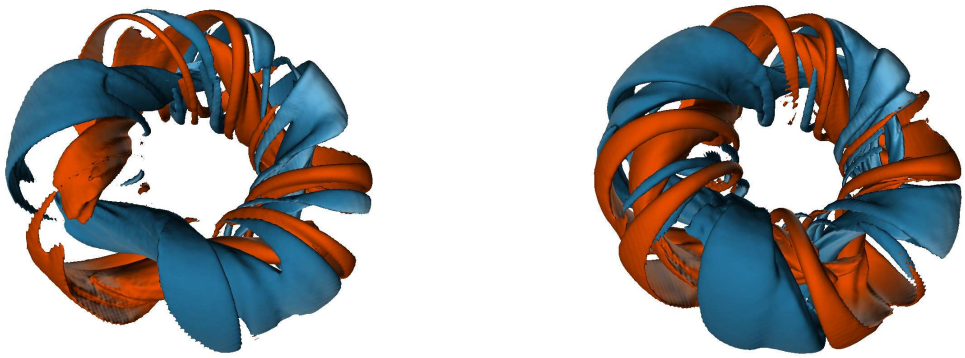

Figure 4.8: Toroidal velocity isocontours +0.01 (blue), -0.01 (orange) for $M = 658$, $\Theta = 1.45$ (left) and $\Theta = 1.57$ (right).

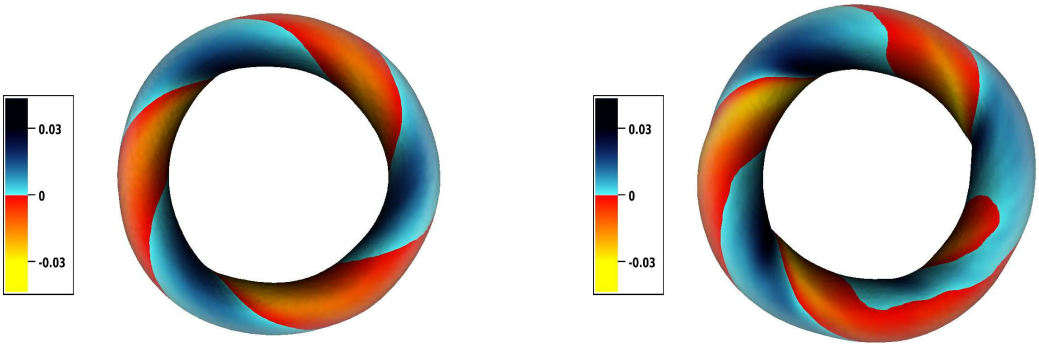

Figure 4.9: Toroidal perturbed magnetic isocontour colored by the toroidal velocity (top view) for $M = 658$, $\Theta = 1.45$ (left) and $\Theta = 1.57$ (right).

in the core is colored by the toroidal velocity. For the first figure (left) two opposite toroidal velocities are clearly visualized as well as the toroidal mode deformation $n = 3$ in the toroidal magnetic isocontour. For increasing pinch ratio (Fig. 4.9 (right)) the mode $n = 4$ dominates the velocity field but with oscillations at the frontier between the positive and negative toroidal velocities. Now if we look at the shape of the magnetic isocontour, a correlation between the toroidal velocity pattern and the deformation of the toroidal magnetic component seems to exist. This isocontour takes a square shape ($n = 4$) that corresponds to the dominant mode in the velocity field. Experimentally (in the RFP MST) similar correlations have been measured between the fluctuation amplitude of the toroidal magnetic field and the velocity field projected in the direction of the experimental measure (chord projected) [84].

Taking into account the spectra at the final state, Fig. 4.10 for $\Theta = 1.45$ and Fig. 4.11 for $\Theta = 1.57$, we see that there is clear correlation between the dominant toroidal modes of the velocity field and the toroidal magnetic field component. The spectrum maximum

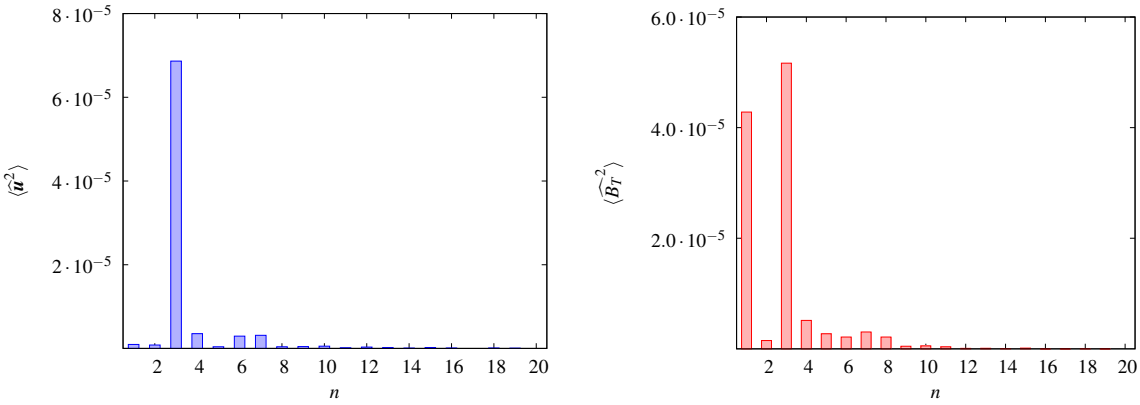

Figure 4.10: Toroidal spectrum of the square velocity (left) and toroidal spectrum of the square toroidal magnetic field component (right) for $M = 658$ and $\Theta = 1.45$.

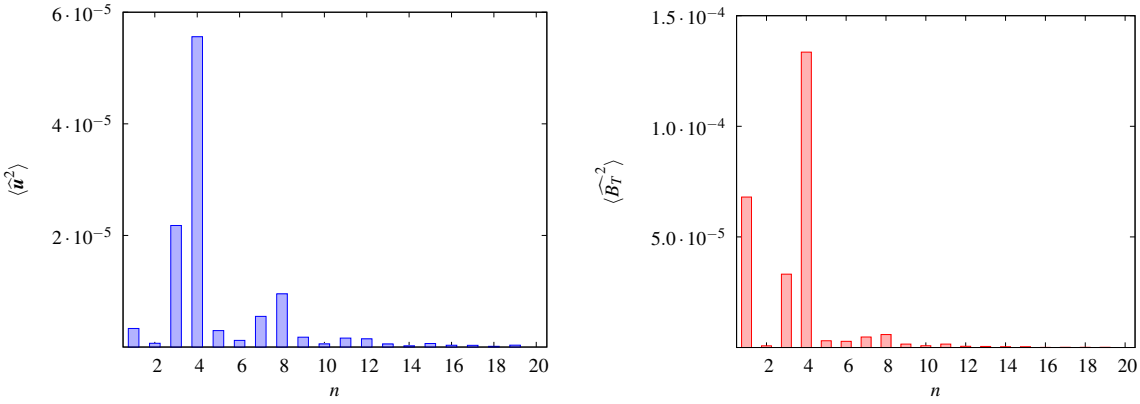

Figure 4.11: Toroidal spectrum of the square velocity (left) and toroidal spectrum of the square toroidal magnetic field component (right) for $M = 658$ and $\Theta = 1.57$.

for the different two quantities is located at the same toroidal mode number, $n = 3$ for the low, and $n = 4$ for the high value of Θ. Notice that in Fig. 4.10 the mode $n = 1$ is important for the toroidal magnetic field, but is not large for the velocity field. It is not clear how the interaction between the two fields generates this $n = 1$ mode. It is probably a complex nonlinear effect composed of a dynamo action and a Lorentz force feedback.

In Fig. 4.12 the azimuthally averaged toroidal and poloidal components of the velocity field are visualized for three different values of the pinch parameter and a constant viscous Lundquist number, $M = 329$. Before the transition, Fig. 4.12 (a), the poloidal flow is composed of the already presented (see Chap. III) pair of counter-rotating vortices, and in the poloidal plane four different zones can be distinguished with positive and negative toroidal velocities. After the transition, Fig. 4.12 (b), the poloidal vortices are considerably enhanced and the toroidal velocity is distributed in just two regions with opposite toroidal directions. For the highest value of the pinch ratio, Fig. 4.12 (c), the 'double smoke ring' is still present and in the center of the poloidal plane a circular zone emerges

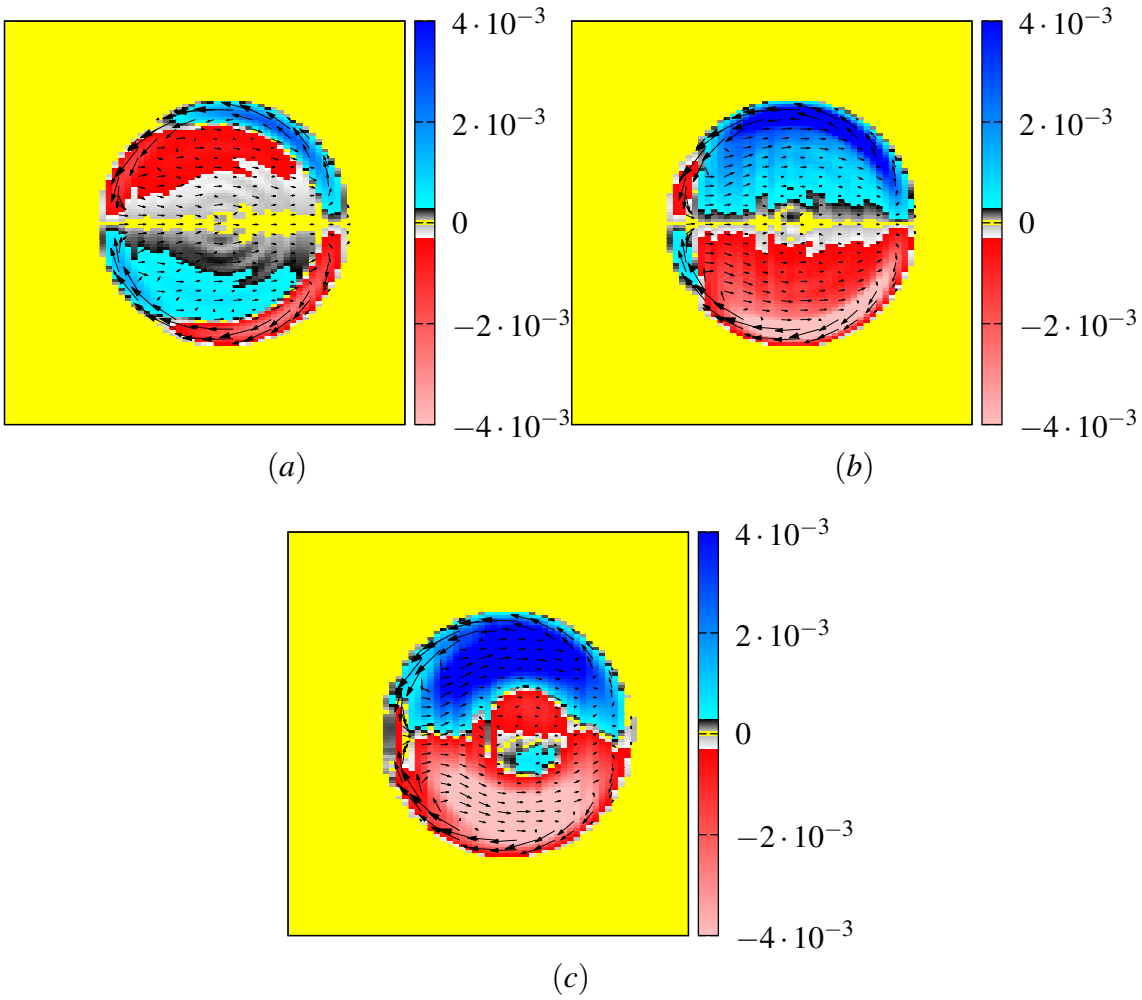

Figure 4.12: Azimuthally averaged toroidal (colour) and poloidal (vectors) components of the velocity field for (a) $\Theta = 0.32$ (here vector norm $\times 10$), (b) $\Theta = 1.44$ and (c) $\Theta = 2.03$, for $M = 329$.

with small toroidal velocity values. This is a consequence of the helical deformation of the magnetofluid. In the poloidal velocities we can notice large values close to the boundaries. There is a steep poloidal velocity gradient in this region. The double vortex flow pattern has been experimentally found in the RFX-mod device [10]. In the literature a flow is shown with poloidal mode number $m = 1$ with the same shear at the plasma edge (for the experiment at $r/a \approx 0.75$). This steep gradient zone could be related to internal transport barriers (ITB) that are observed on a statistical basis in RFX-mod at $r/a \leq 0.7$ [88]. For the toroidal velocity component, recent measurements have been performed in the MST experiment that show the toroidal velocity inversion for $r/a \sim 0.5$ [30].

The azimuthally averaged perturbed toroidal magnetic field is presented in Fig. 4.13 for three different pinch parameters as in the previous paragraph. In this figure we see, with increasing Θ, the enhancement of the toroidal field by the dynamo effect. For the

axisymmetric simulation a very weak toroidal field develops (Fig. 4.13 (a)). For increasing pinch ratio the helical transition occurs and we observe a more important toroidal field (Fig. 4.13 (b)). In the last image (Fig. 4.13 (c)) the toroidal magnetic field continues to grow and becomes more peaked in the center.

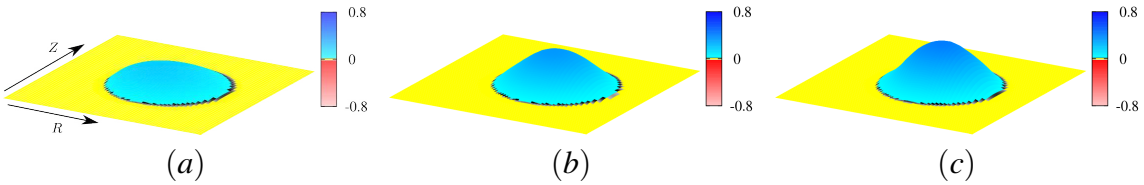

Figure 4.13: Azimuthally averaged perturbed toroidal magnetic field for $\Theta = 0.32$ (a), $\Theta = 1.44$ (b) and $\Theta = 2.03$ (c), for $M = 329$ at the saturated state.

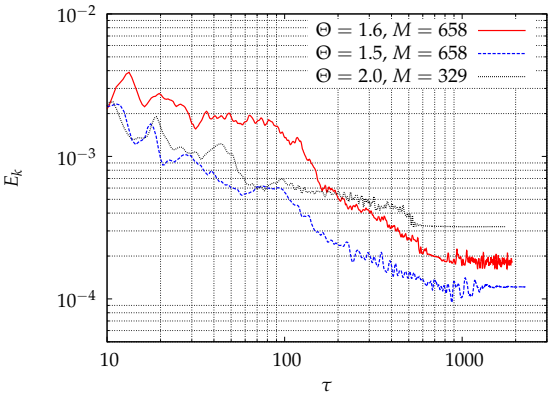

Figure 4.14: Kinetic energy evolution as a function of the poloidal Alfvén time.

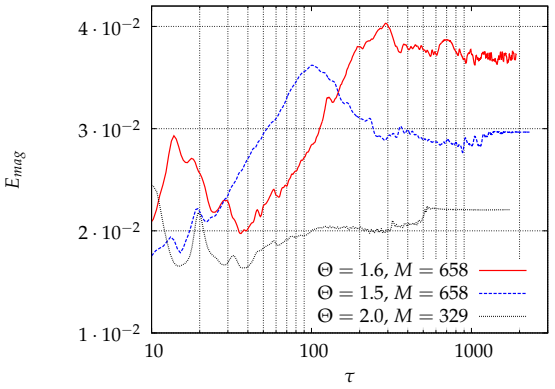

Figure 4.15: Evolution of the magnetic energy of the perturbation as a function of the poloidal Alfvén time.

2.2 EVOLUTION OF GLOBAL QUANTITIES

The kinetic energy and the magnetic energy of the perturbation are presented, respectively, in Figs. 4.14 and 4.15. The saturation, as well as the oscillations for high viscous Lundquist and pinch ratio values are visualized. At the steady state the kinetic energy of the system varies considerably with the pinch ratio (see Fig. 4.16). For increasing values of Θ the kinetic energy grows at the steady state. We observe that for low values of the pinch parameter the kinetic energy is more important if the viscous Lundquist number is low (as also observed in the previous chapter). But for a certain value of Θ (≈ 1.4) the high viscous Lundquist curve crosses the other curve and the system with lower viscosity has a larger kinetic energy. Also we notice that after the transition (between $\Theta = 0.65$ and $\Theta = 1.44$) the kinetic energy increases by a factor of ten (Fig. 4.16, curve $M = 329$).

The magnetic energy of the fluctuation is calculated at the steady state, and its evolution with the pinch parameter is presented in Fig. 4.17. This energy increases with the

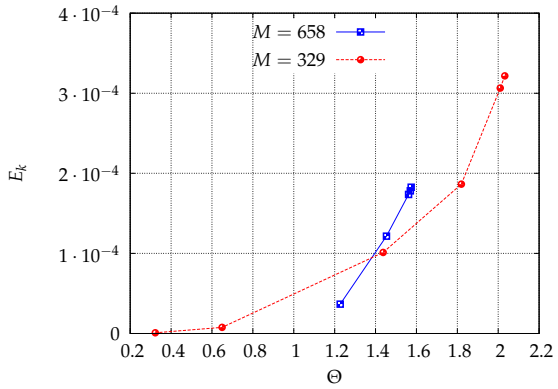

Figure 4.16: Kinetic energy as a function of the pinch ratio.

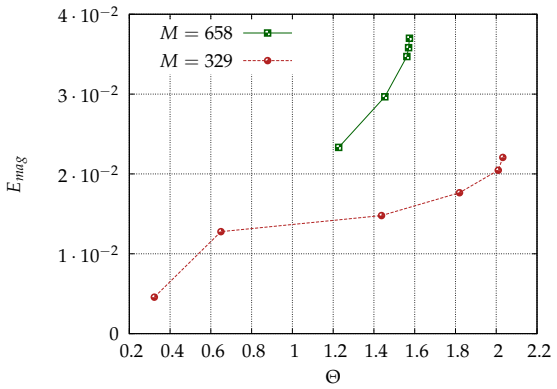

Figure 4.17: Fluctuating magnetic energy as a function of the pinch ratio.

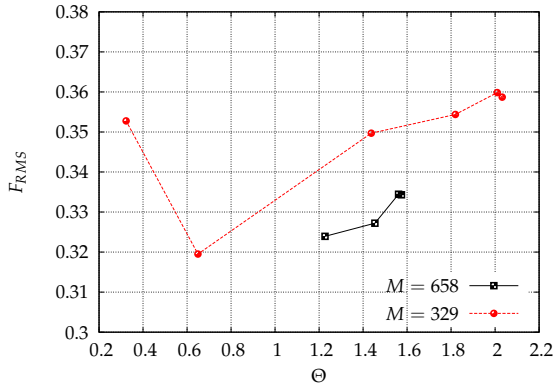

Figure 4.18: RMS Lorentz force as a function of the pinch ratio.

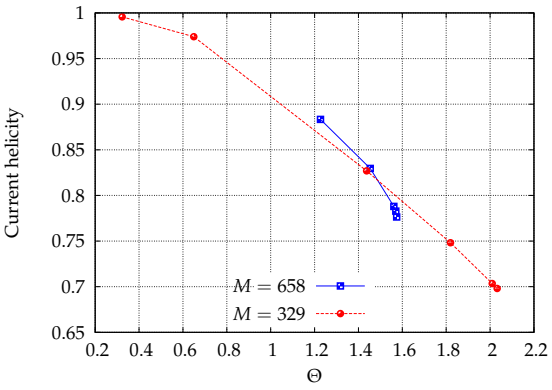

Figure 4.19: Volume averaged current helicity as a function of the pinch ratio.

pinch ratio. Its magnitude and its growth rate with Θ are large for the higher viscous Lundquist simulations.

For the case $M = 329$ we note a large increase of the perturbed magnetic energy between the first two Θ values.

The root mean square value of the Lorentz force is shown in Fig. 4.18. We observe that there is not a significant change in its value for increasing pinch ratio and for the considered viscous Lundquist numbers. There is a slight increase of the magnitude of the Lorentz force with the pinch parameter. This is compatible with the decrease of the alignment between the current density and magnetic field with Θ. This misalignment is stressed in Fig. 4.19 where the current helicity is presented. It is shown that for increasing pinch ratio the alignment between the magnetic and current density field is less important.

The spatial distribution of the norm of the Lorentz force (Fig. 4.20) shows that for increasing pinch ratio the central region of the torus becomes force free, as also observed in the previous chapter. But as stated above the root mean square of this quantity slightly

grows, and this is because at the boundaries the magnitude of the Lorentz force strongly increases.

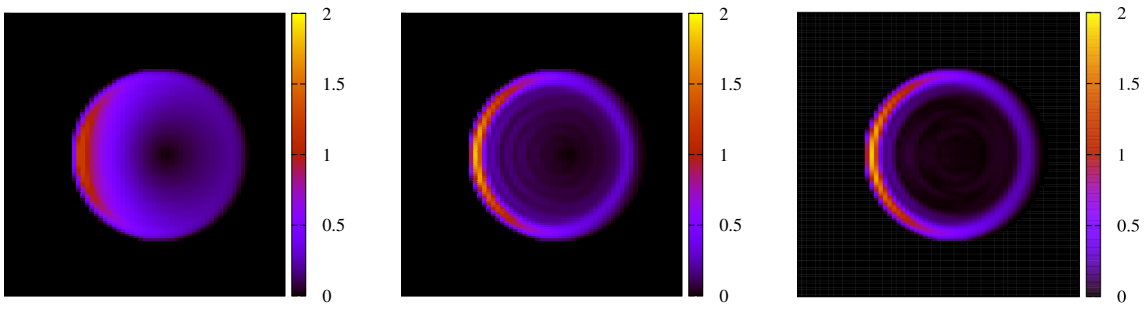

(a) (b) (c)

Figure 4.20: Azimuthally averaged vector norm of the Lorentz force for $\Theta = 0.32$ (a), $\Theta = 1.44$ (b) and $\Theta = 2.03$ (c), for $M = 329$ at the saturated state.

2.3 TIME EVOLUTION OF THE DIFFERENT TOROIDAL MODES

In the present study we have seen that the energy is distributed over a relatively small number of modes. In this section we will focus on the analysis of the system when it has arrived at the saturated state. Generally the simulations show a large variety of behaviors depending on the choice of the parameters. Small changes in the imposed parameters can generate significant modifications in the magnetofluid dynamics. With the evolution of the kinetic energy contained in the different toroidal modes, we want to illustrate the diversity in the dynamics and the sensibility of the magnetofluid to the variation of the pinch parameter and the viscous Lundquist number.

The evolution of different mean square toroidal spectra is presented in Fig. 4.21 for different pinch ratios and fixed $M = 329$. Here the transition is clearly visible, it occurs between the cases $\Theta = 0.649$ and $\Theta = 1.437$. The first two figures (at the top) show no fluctuations and the zero toroidal mode is at least two orders of magnitude bigger than the second largest. For $\Theta = 1.437$ the zero mode is not longer dominant. If we look at this figure the axisymmetric mode ($n = 0$) shows a non oscillatory behavior unlike the other modes that oscillate with a large time period. The dominant mode $n = 4$ alternates with others and at the final time a steady state can be suspected.

The dynamics of the magnetofluid for a higher pinch parameter ($\Theta = 1.820$) are quite different. For the early times the system oscillates importantly and then for a time $\tau \approx 700$ (in poloidal Alfvén times) the system is completely steady, all the temporal oscillations are damped. A similar phenomenon appears for the two highest values of Θ presented in Fig. 4.21. The system oscillates strongly and then settles into a quiet steady state.

For increasing viscous Lundquist number ($M = 658$) a different behavior is present (see Fig. 4.22). After the transition to a helical state between $\Theta = 1.227$ and $\Theta = 1.454$ the system starts to strongly oscillate. Only for the case $\Theta = 1.454$ we have a similar

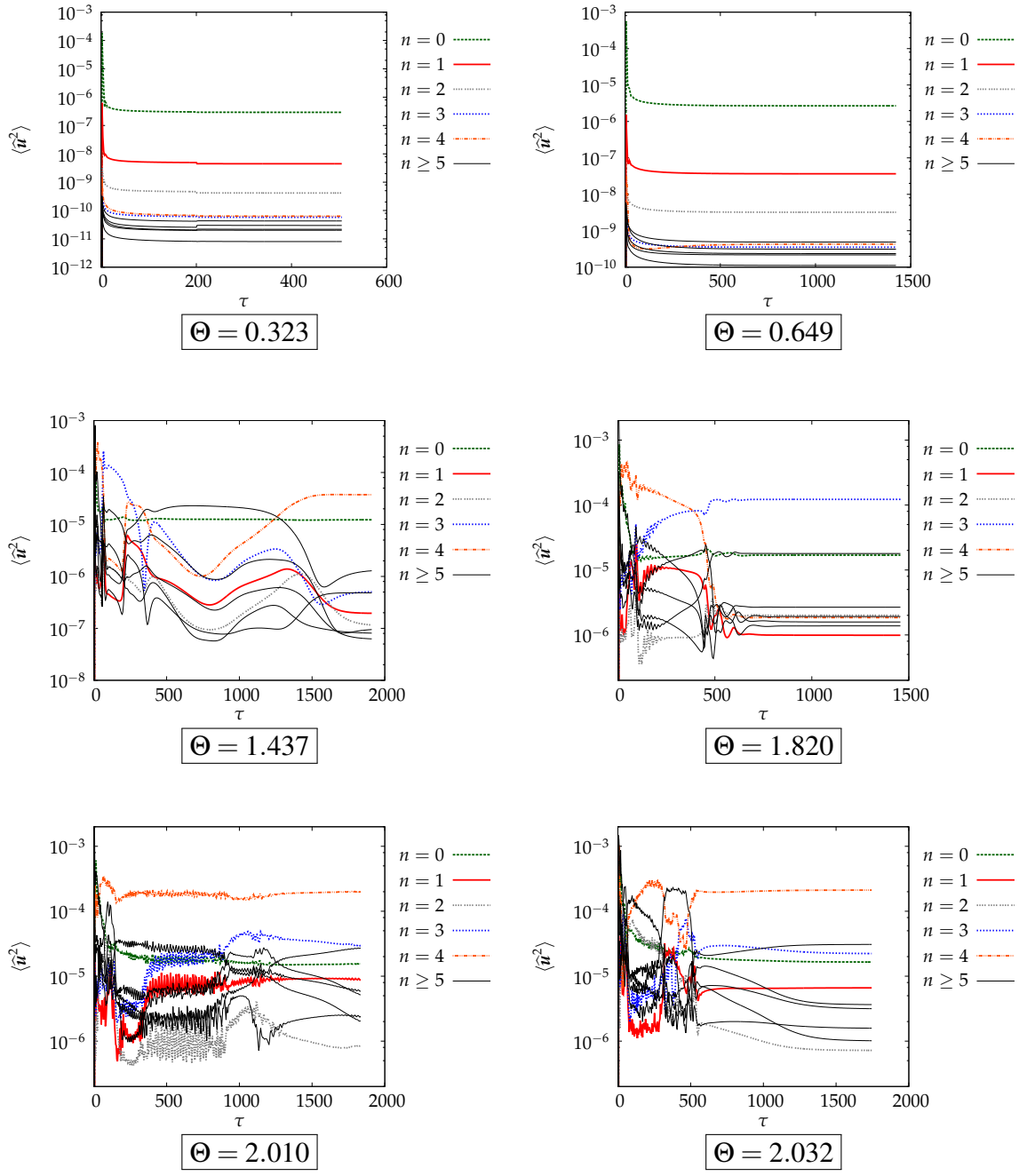

Figure 4.21: Time evolution of the kinetic energy contained in the first toroidal modes for $M = 329$ and $Pr = 3$.

behavior as presented previously: at early times we have strong oscillations followed by a relatively calm stationary state. For the rest of the cases, with large Θ, the oscillations that started in the early times are not damped and a strongly fluctuating steady state develops.

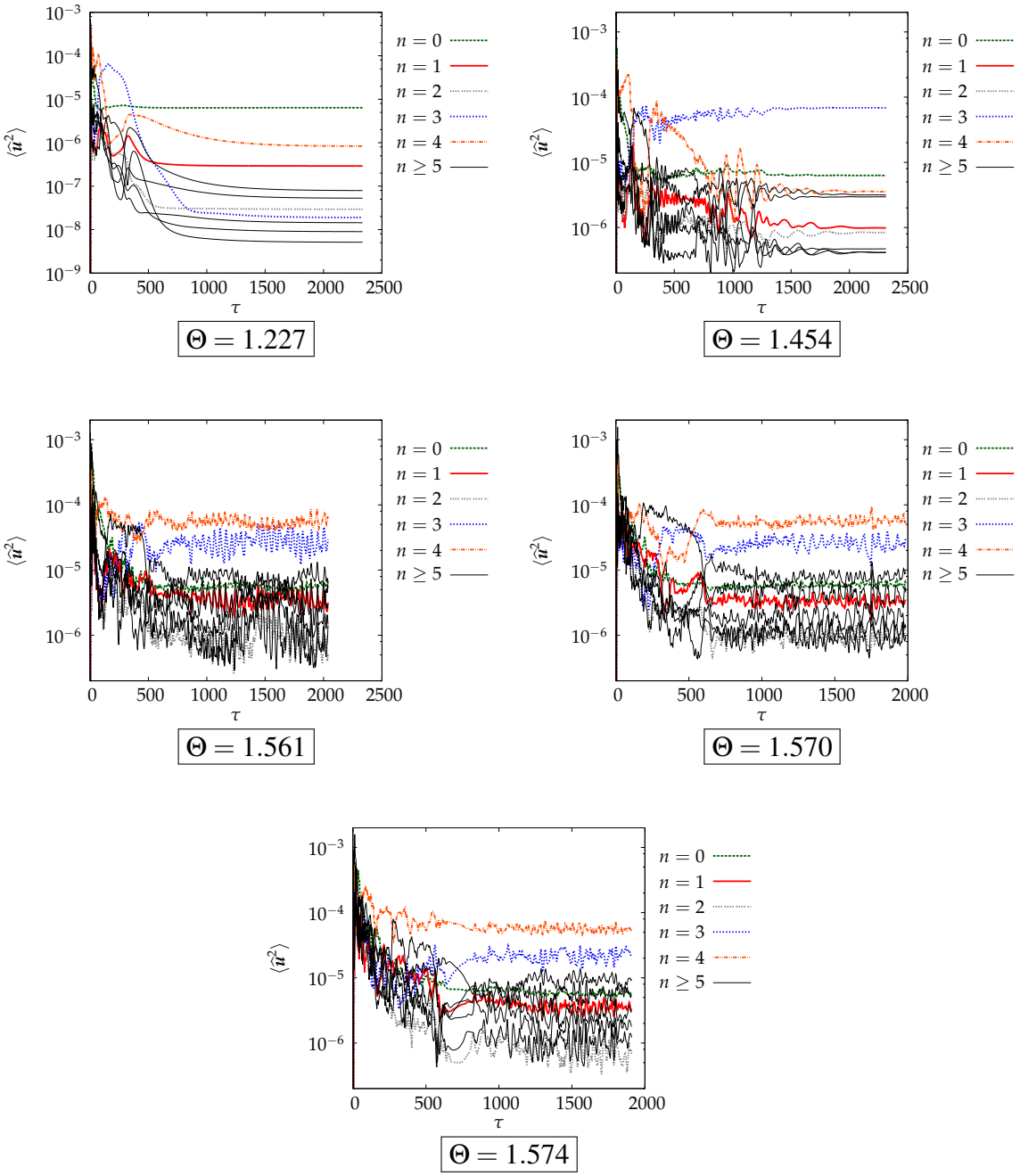

Figure 4.22: Time evolution of the kinetic energy contained in the first toroidal modes for $M = 658$ and $Pr = 3$.

Notice also the change in the dominant toroidal mode: after the instability the $n = 3$ mode holds the highest energy value but for the last oscillating three cases the dominant mode is $n = 4$.

To quantify and compare the oscillations in the system we compute the standard deviation of the kinetic and magnetic energies in the saturated state (see Fig. 4.23). For both energies the standard deviation for the biggest viscous Lundquist number is one or two orders of magnitude bigger than for the low viscous Lundquist number. The figure also shows a transition with increasing pinch ratio. For a particular value of Θ there is a strong increase in the value of the standard deviation (at least one order of magnitude). This threshold is at the same position for the kinetic and magnetic energies. Its value is $\Theta \approx 1.9$ for $M = 329$ and $\Theta \approx 1.55$ for $M = 658$.

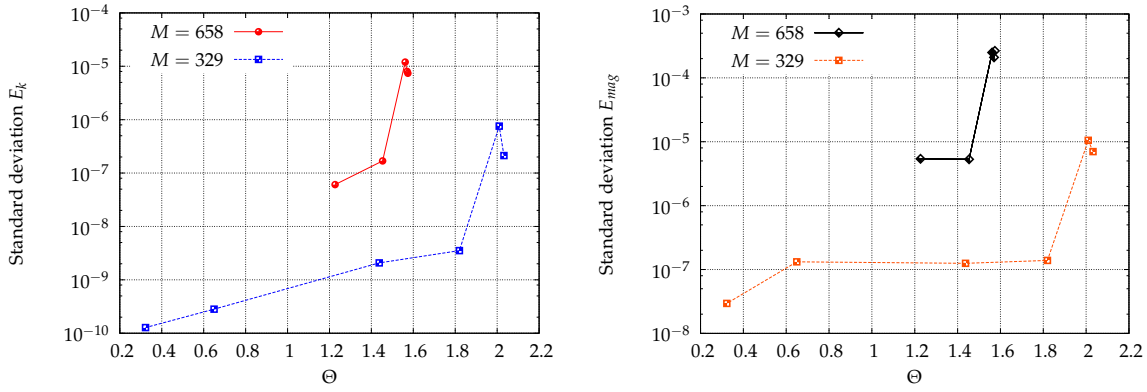

Figure 4.23: Temporal standard deviation of the kinetic (left) and perturbed magnetic energy (right) at the saturated state for the torus geometry.

2.4 SUMMARY OF THE TOROIDAL SIMULATIONS

In this section we have presented the transition of the toroidal magnetohydrodynamic flow between an axisymmetric and a helical state. This transition appears for increasing pinch ratio and sufficiently large viscous Lundquist and Prandtl numbers. The helical state is characterized by different toroidal modes that dominate the system depending on the considered parameters. The kinetic and perturbed magnetic energies increase considerably when the instability is triggered. The root mean square average of the Lorentz force is almost invariant but its spatial distribution changes considerably. For increasing pinch ratio at the center of the domain a force free region appears but at the edge of the torus the magnitude of this force is considerably enhanced.

The analysis of the time evolution of the mean square velocity for each toroidal mode displays a complex behavior. Depending on the Θ parameter and the viscous Lundquist number the dynamics change dramatically. For a low M a non oscillatory steady state is obtained at the final times. On the other hand for the biggest viscous Lundquist numbers, strong oscillatory dynamics appear. This state is turbulent in the sense that we observe chaotic spatio-temporal fluctuations involving different modes, but the dynamics is still dominated by a single toroidal mode. It is therefore a quasi-single helicity state [32]. It is

still an open question if multiple helicity states will be obtained with increasing viscous Lundquist number.

3 CYLINDRICAL SIMULATIONS

In this section the helical states of a cylindrical magnetofluid are presented. We will roughly consider the same quantities as in the preceding section on the toroidal simulations. This will allow us to highlight the differences and similarities between the dynamics in the two geometries. First the analysis of the dominant axial modes and the study of the flow topology as a function of the pinch ratio are carried out. Then the global quantities varying with Θ are shown. Finally the time evolution of the axial modes is analysed.

The imposed magnetic field for the cylinder is helical. It is composed of a poloidal linear magnetic field ($B_{0_P}(r)$) and a constant axial magnetic component (B_{0_z}) (Fig. 4.24). The linear profile for the poloidal magnetic field comes from an imposed axial constant electric field in a system with constant resistivity (see Chap. II Sec. 5.2 and [102]). The profile of the poloidal magnetic field is the following,

$$B_{0_P}(r) = \frac{\sigma E_{0_z} r}{2}. \tag{4.4}$$

The value of this field is fixed at the boundary of the cylinder and it is kept constant, $B_{0_P}(a) = 0.32$ (we recall that a is the cylinder radius). The reference magnetic field for the cylindrical calculations is fixed to $B_{ref} = B_{0_P}(a) = 0.32$.

To vary the pinch ratio we modify the value of the axial magnetic field (B_{0_z}) and the poloidal component is constant for the considered simulations. The initial velocity field is a small perturbation. It is a white noise with kinetic energy $\approx 4.3 \cdot 10^{-7}$. This perturbation is necessary to trigger the helical instability. The perturbed initial magnetic field is zero. Note that no perturbation was needed in the toroidal geometry where the spontaneous appearance of the $n = 0$ mode allowed to trigger the transition.

The cylinder has a radius $a = 1$ and height $L_z = 4\pi$, the curvature effects are neglected which is the major difference with the toroidal case. This corresponds to a "straight torus" where the aspect ratio, major radius over minor radius is $\Gamma = 2$. The size of the periodic box where the calculations are performed is $(0.8\pi \times 0.8\pi \times 4\pi)$. We fix the penalization parameter to $\eta = 5 \cdot 10^{-4}$. The resolution for all the cylindrical calculations is 128^3 and we consider for both cases constant resistivity and viscosity. We vary the viscous Lundquist number (M) and we consider two Prandtl numbers (Pr). We evaluate the system as a function of the pinch ratio at the final state (Θ). The dimensionless numbers characterizing the dynamical system are defined as follows,

$$M = \frac{C_A L}{\nu}, \qquad Pr = \frac{\nu}{\lambda}, \qquad \Theta = \frac{\overline{B_P(a)}}{\langle B_z \rangle}, \qquad F = \frac{\overline{B_z(a)}}{\langle B_z \rangle}, \tag{4.5}$$

with C_A the poloidal Alfvén velocity. With respect to the toroidal simulations the main difference is the toroidal magnetic field which has been replaced by the axial magnetic field B_z. As a reference length we take the diameter $L = 2$, ν is the viscosity, λ the magnetic diffusivity and a is the radius of the cylinder.

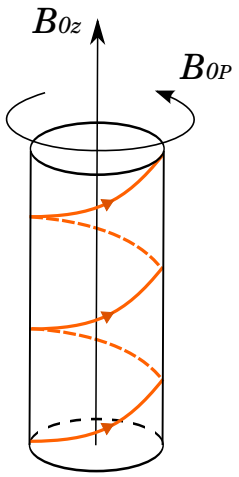

Figure 4.24: Scheme of the helical magnetic field imposed for the cylindrical simulations.

The periodic cylindrical simulations are performed for various pinch ratios and two viscous Lundquist numbers, as in the previous section. We take into account the following dimensionless numbers $M = 634$ with a magnetic Prandtl number $Pr = 3$ and $M = 1902$ with $Pr = 2$. As in the previous section this choice is physically quite arbitrary but allows for a numerical investigation of a wide range of different pinch ratios.

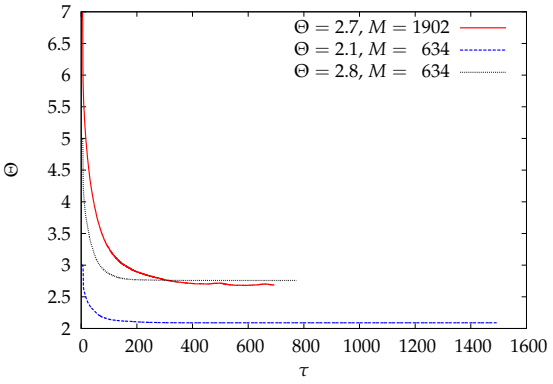

Figure 4.25: Pinch ratio evolution for the cylindrical geometry as a function of the poloidal Alfvén time.

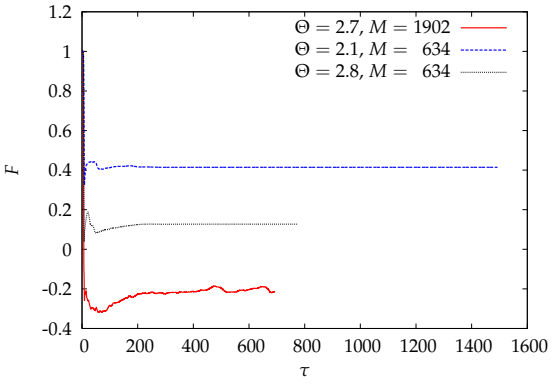

Figure 4.26: Reversal parameter evolution for the cylindrical geometry as a function of the poloidal Alfvén time.

3.1 HELICAL FLOWS

The time evolution of the reversal parameter and the pinch ratio are presented in Figs. 4.25 and 4.26 respectively. The two quantities reach an asymptote, and there is a final steady state. For the highest viscous Lundquist number ($M = 1902$) there exist oscillations in the saturated state. This effect is quite similar as the one found in the toroidal simulations. The F parameter evolution shows a decrease for the early times followed by a regrowth. This is linked to the dynamo action that enhances the axial magnetic field (see Fig. 4.27). For the cylindrical case a bigger viscous Lundquist number value ($M = 1902$) is considered than for the study of the toroidal geometry. For this large M a reversal of the toroidal magnetic field is found if the the pinch ratio is increased sufficiently (see Fig. 4.26). The increase of the viscous Lundquist number seems to be important to make the toroidal magnetic field reverse at the edge.

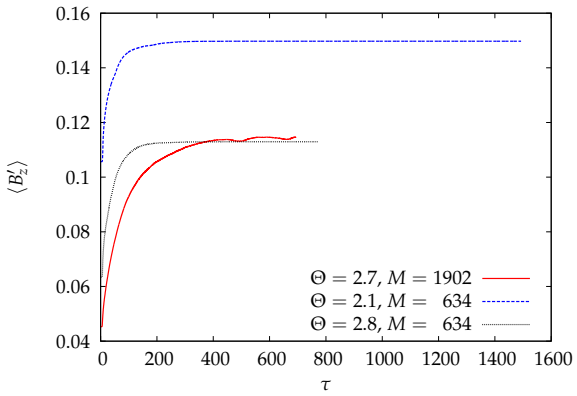

Figure 4.27: Perturbed toroidal component of the magnetic field as a function of the poloidal Alfvén time.

As in the previous toroidal study, the flow in the cylinder has a transition towards a helical configuration. The difference is that the state preceding the transition is not longer a toroidally invariant state (in the case of a cylinder we would say z-invariant or axially invariant state) but it is a zero velocity field, also called 'copper wire' solution [102]. After the transition a helical deformation of the magnetofluid appears. It is characterized by different axial mode numbers (k_z). For the majority of studied cases the dominant axial mode is $k_z = 4$. For some cases higher dominant modes are present such as, $k_z = 5$ and $k_z = 7$.

In Fig. 4.28 the ratio of the energy contained in the axial modes 0, 4, 5 and 7 over the total energy is presented as a function of the pinch ratio and for two different viscous Lundquist numbers. In both cases the zero axial mode has a negligible fraction of the total energy for all the pinch ratio values considered.

For the low viscous Lundquist number, $M = 634$ (Fig. 4.28 (left)) there are always one or two modes that possess more than 30% of the total energy. Therefore this system is dominated by a few helical modes. If $M = 1902$ (Fig. 4.28 (right)) at low pinch ratio

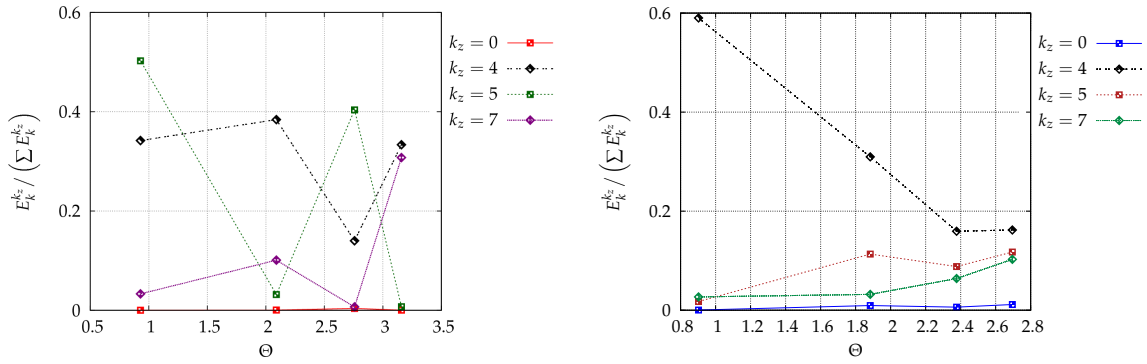

Figure 4.28: Ratio of the kinetic energy of the dominant modes over the total kinetic energy for the cylindrical geometry as a function of Θ, $M = 634$ (left) and $M = 1902$ (right).

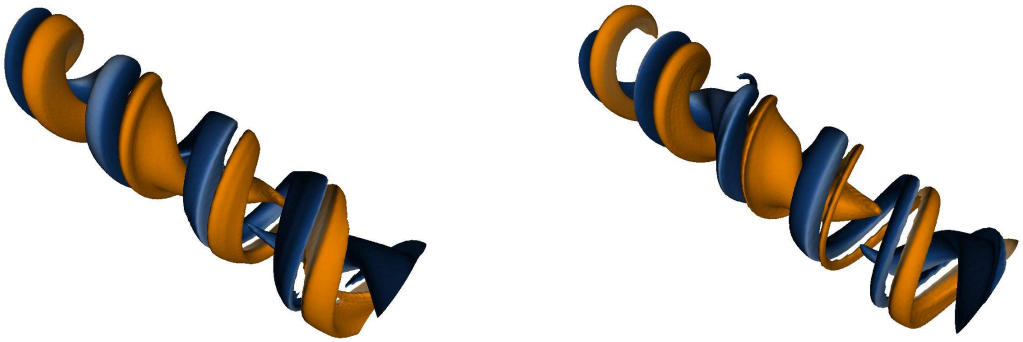

Figure 4.29: Axial velocity isocontours +0.011 (blue) and -0.011 (orange) for $\Theta = 2.1$ (left) and $\Theta = 2.8$ (right), for both cases $M = 634$.

($\Theta = 0.9$) the mode $k_z = 4$ dominates clearly with more than 50% of the total energy. Then, for a pinch ratio greater than 2.2, the energy of the considered modes converges, in each mode the energy is below 20% of the total kinetic energy. This means that the energy spectrum is more flat and we have a state that could be described as a multiple helicity state.

To illustrate these helical states we show in figure 4.29 a positive and a negative isocontour of axial velocity for two different values of the pinch parameter. For the case with $\Theta = 2.1$ the fourth axial mode dominates the final state. On the other hand for $\Theta = 2.8$ the dominant mode is $k_z = 5$. The two axial velocity isocontours share the same magnitude but are in opposite directions. These oppositely signed isocontours have a similar topology, and they are separated by a short axial distance.

As for the toroidal simulations there is a correlation between the helical deformation of the perturbed axial magnetic field and the dominant toroidal velocity modes. This is visualized in Fig. 4.30 where we present a perturbed toroidal magnetic isocontour colored by the axial velocity. In this figure the deformation of the magnetic field (the shape of the

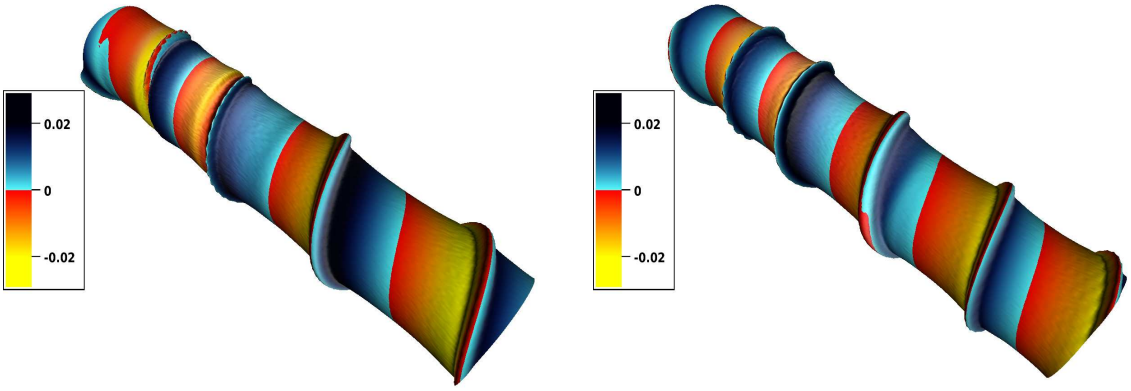

Figure 4.30: Axial perturbed magnetic field isocontour colored by the axial velocity for $M = 634$, $\Theta = 2.1$ (left) and $\Theta = 2.8$ (right).

isocontours) is well correlated with the change of sign of the axial velocity (indicated by the color of the isocontours).

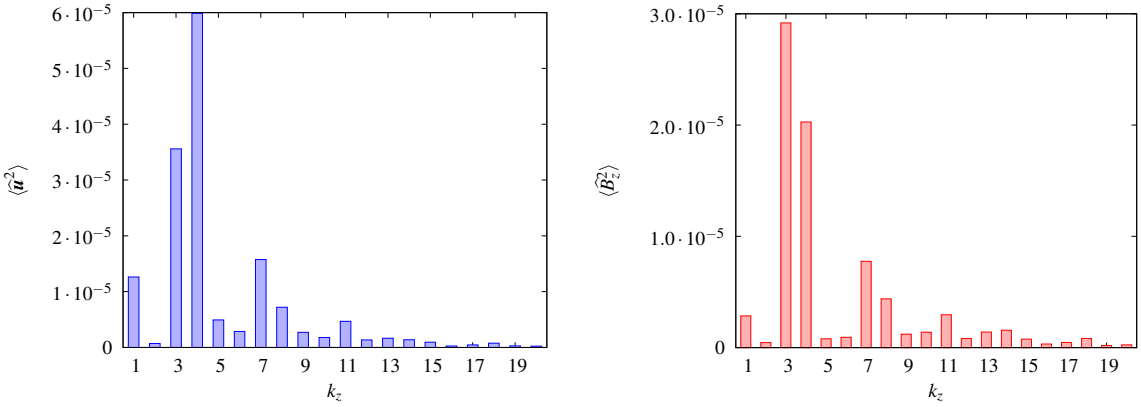

Figure 4.31: Axial spectra of the square velocity field (left) and of the axial component of the perturbed magnetic field (right) for $M = 634$ and $\Theta = 2.1$.

If we now look at the kinetic and axial magnetic spectra (Figs. 4.31 and 4.32) we notice that the maximum values are located at the same axial mode numbers. In the case with $\Theta = 2.1$ (Fig. 4.31 (left)) the dominant mode for the kinetic field is $k_z = 4$ followed by the third mode $k_z = 3$. For the axial magnetic field (Fig. 4.31 (right)) the dominant mode is $k_z = 3$ but the second in magnitude is $k_z = 4$. The same two dominant modes in the system appear both in the kinetic and in the axial magnetic fields spectra.

For a larger value of the pinch ratio ($\Theta = 2.8$) the similarity between the kinetic and magnetic spectra is more pronounced (see Fig. 4.32). The dominant and the secondary modes are similar. The biggest axial modes correspond to small values of k_z, varying from $k_z = 3$ to $k_z = 5$, with a strong predominance of the fifth mode for the two considered fields.

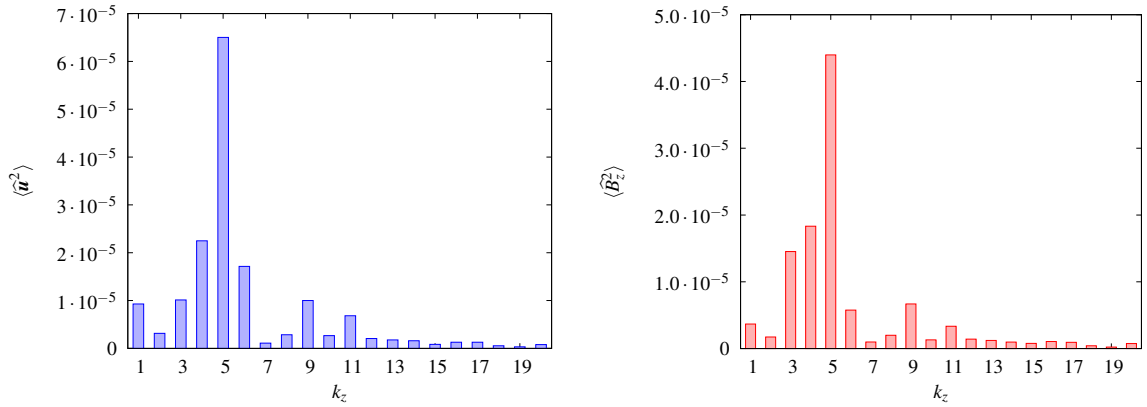

Figure 4.32: Axial spectra of the square velocity field (left) and of the axial component of the perturbed magnetic field (right) for $M = 634$ and $\Theta = 2.8$.

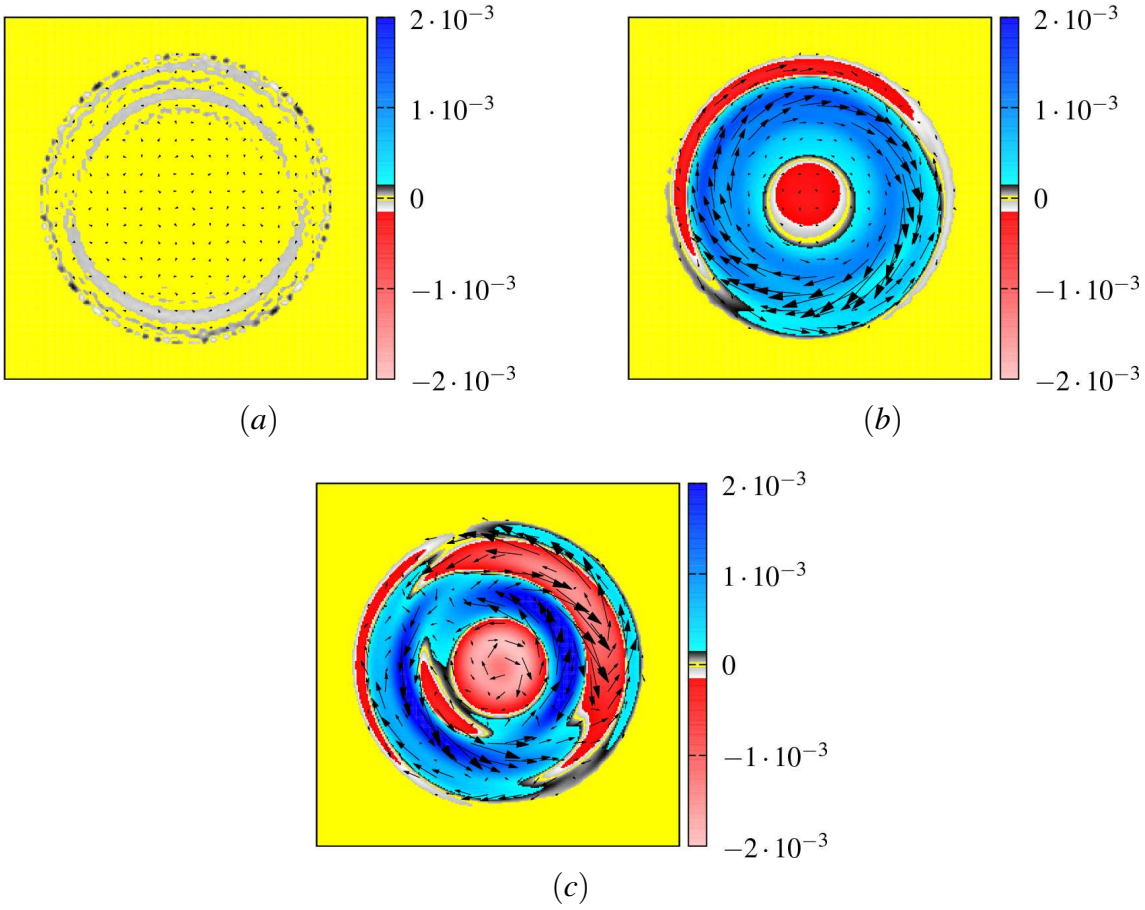

Figure 4.33: Axially averaged axial (colour) and poloidal (vectors) components of the velocity field for (a) $\Theta = 0.90$, (b) $\Theta = 1.88$ and (c) $\Theta = 2.70$, for $M = 1902$ at the saturated state.

The velocity field has helical perturbations and varies as a function of the pinch ratio. To illustrate this variation we take at one instant, in the steady state, the average in the z direction of the axial and poloidal plane velocities. The Fig. 4.33 shows this velocity average, two distinct flow topologies as a function of Θ can be distinguished. For the lowest value of the pinch parameter (Fig. 4.33 (a)) the axial average shows small velocities compared to the others two figures ((b) and (c)). This is a consequence of the strong dominance of the axial mode $k_z = 4$ for the case (a). It was shown in Fig. 4.28 that the energy contained in the fourth mode for the pinch ratio $\Theta = 0.9$ is almost 60% of the total energy, so that we have a laminar quasi-single helicity state. Previously we saw that a positive axial velocity with a helical structure comes along with a negative one (Fig. 4.29). In this laminar helical state, the axial averaging adds both contributions up to zero.

The flow topology of the cases (b) and (c) in Fig. 4.33 is similar but its axially average is qualitatively different. There exist positive and negative axial velocity regions, but the flow is more chaotic for the largest value of the pinch ratio ($\Theta = 2.7$). A central circular zone can be distinguished where the flow is oriented in one axial direction and where the poloidal velocities are relatively small.

3.2 EVOLUTION OF GLOBAL QUANTITIES

The time evolution of the kinetic and perturbed magnetic energy are presented in Fig. 4.34 for a viscous Lundquist number $M = 1902$. There is a similar growth in both quantities when the instability is triggered. The increase in the pinch parameter make the two energies oscillate. At the saturated state there are fluctuations for the calculations with $\Theta = 1.88$ and $\Theta = 2.70$.

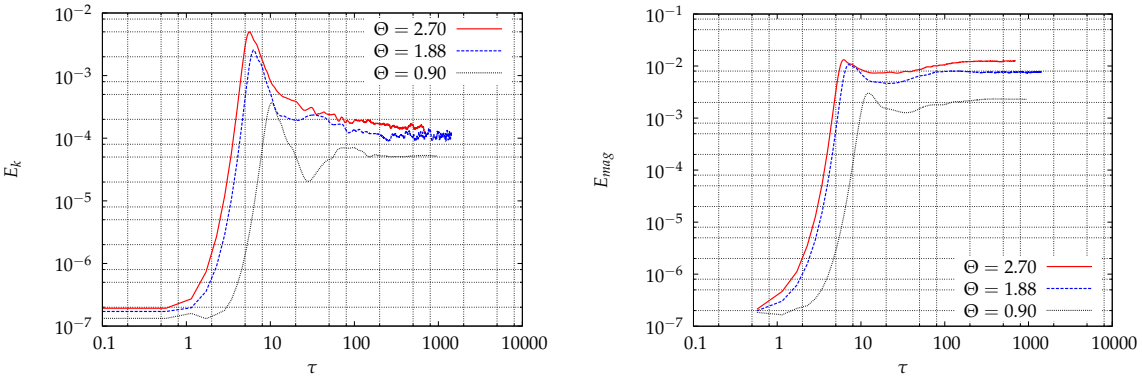

Figure 4.34: Evolution of the kinetic energy (left) and of the perturbed magnetic energy (right) for the cylindrical geometry as a function of the poloidal Alfvén time, $M = 1902$ and $Pr = 2$.

The evolution of the kinetic and perturbed magnetic energy with the pinch parameter for the two considered M numbers is almost linear (Fig. 4.35). The kinetic energy for the largest value of Θ is four times bigger than for the lowest. The influence of the viscous Lundquist number is not very important in the evolution of the kinetic energy. On the

other hand in the perturbed magnetic energy the computations show different evolutions depending on the considered M number. There is a linear evolution but at high pinch ratio the energy for $M = 1902$ is twice as big as for $M = 634$. The dynamo action seems to be stronger for large viscous Lundquist values. Given that the kinetic energy is comparable, this seems logical since the magnetic perturbation will be more smoothened out by higher diffusion at lower viscous Lundquist number.

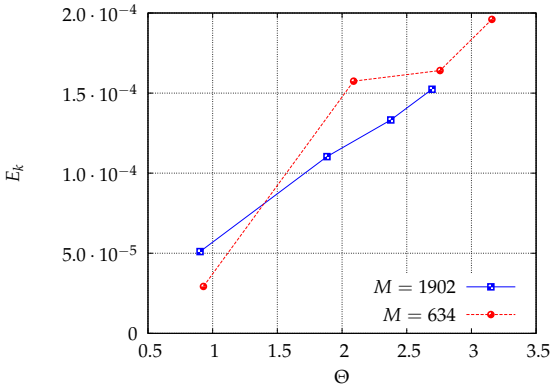

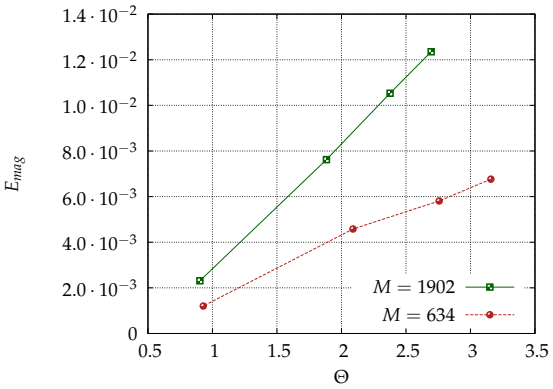

Figure 4.35: Evolution of the kinetic energy (left) and of the perturbed magnetic energy (right) for the cylindrical geometry as a function of the pinch ratio.

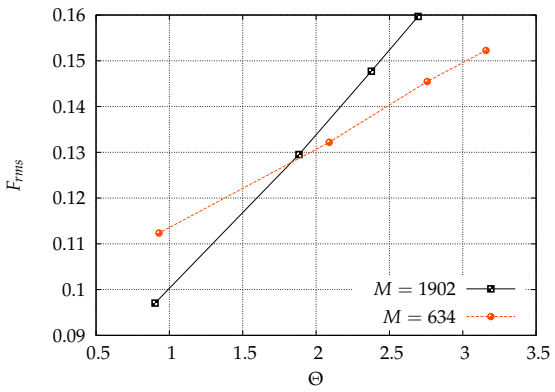

Figure 4.36: Root mean square of the Lorentz force as a function of Θ.

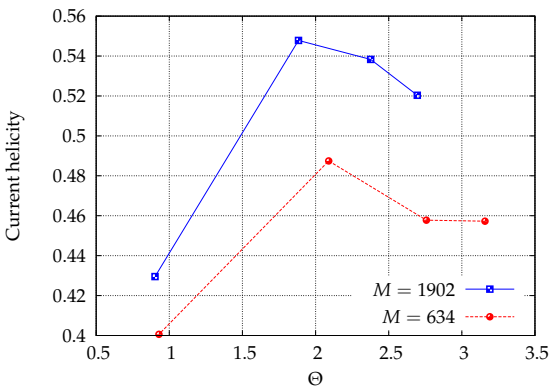

Figure 4.37: Current helicity as a function of Θ.

The evolution in the kinetic and perturbed magnetic energies shows the same tendency as the evolution of the root mean square of the total Lorentz force in the volume (see Fig. 4.36). The Lorentz force has a linear evolution with Θ, and there is a growth of $\sim 50\%$ between the lowest and the highest pinch parameter value.

The current helicity is presented in Fig. 4.37. This quantity is far from unity, indicating the absence of alignment between the total magnetic and current density fields. Both fields have a tendency to align with increasing pinch ratio, as indicated by the current helicity value that grows, but this change is relatively small.

The spatial distribution of the norm of the Lorentz force is presented in Fig. 4.38 for three different pinch ratios and constant viscous Lundquist number ($M = 1902$). As for the toroidal simulations the field tends to be force free in the center of the geometry. There is also an important increase of the value of its magnitude near the boundaries. Notice also that for the case with $\Theta = 2.7$ helical perturbations in the center of the domain are visualized. These will probably average out if in addition to the axial average a time average would be applied.

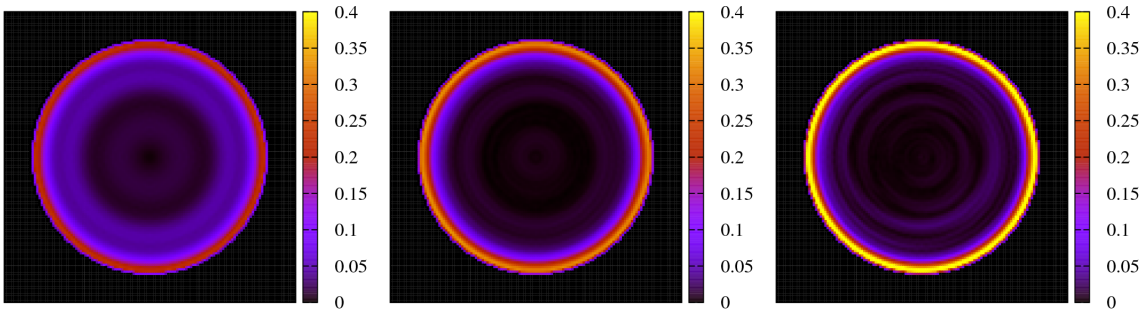

Figure 4.38: Axially averaged vector norm of the Lorentz force for $\Theta = 0.90$ (a), $\Theta = 1.88$ (b) and $\Theta = 2.70$ (c), for $M = 1902$ at the saturated state.

3.3 TIME EVOLUTION OF THE DIFFERENT AXIAL MODES

The evolution of the square velocity for the different axial mode numbers is presented in Fig. 4.39 for $M = 634$ and in Fig. 4.40 for $M = 1902$. The axial mode $k_z = 0$ is not presented because for all the considered simulations the square velocity magnitudes for this mode are several orders of magnitude smaller than for the other modes exposed here.

In the first figure ($\Theta = 0.93$) there is clear temporal frequency that dominates the system with a constant period of ~ 100 poloidal Alfvén unit times. The dominant modes in this case are: $k_z = 4$ and $k_z = 5$. For increasing pinch ratio the temporal frequency vanishes and there is a steady predominance of the fourth axial mode ($\Theta = 2.09$).

With a further increase in the pinch ratio ($\Theta = 2.76$) the dominant mode changes, it is not longer $k_z = 4$ but $k_z = 5$. For the largest value, $\Theta = 3.16$, a higher mode ($k_z = 7$) starts dominating the system together with the lower mode, $k_z = 4$.

The system at this viscous Lundquist number shows dynamics different from the toroidal geometry. The mode $k_z = 4$ is only one of the dominant modes. A difference with the torus case is the appearance of higher mode numbers such as $k_z = 5$ and $k_z = 7$. For the present viscous Lundquist number and pinch ratios there are no chaotic temporal oscillations.

Now if we look at the time evolution of the axial modes for the highest viscous Lundquist number ($M = 1902$) completely different dynamics appear (Fig. 4.40). For

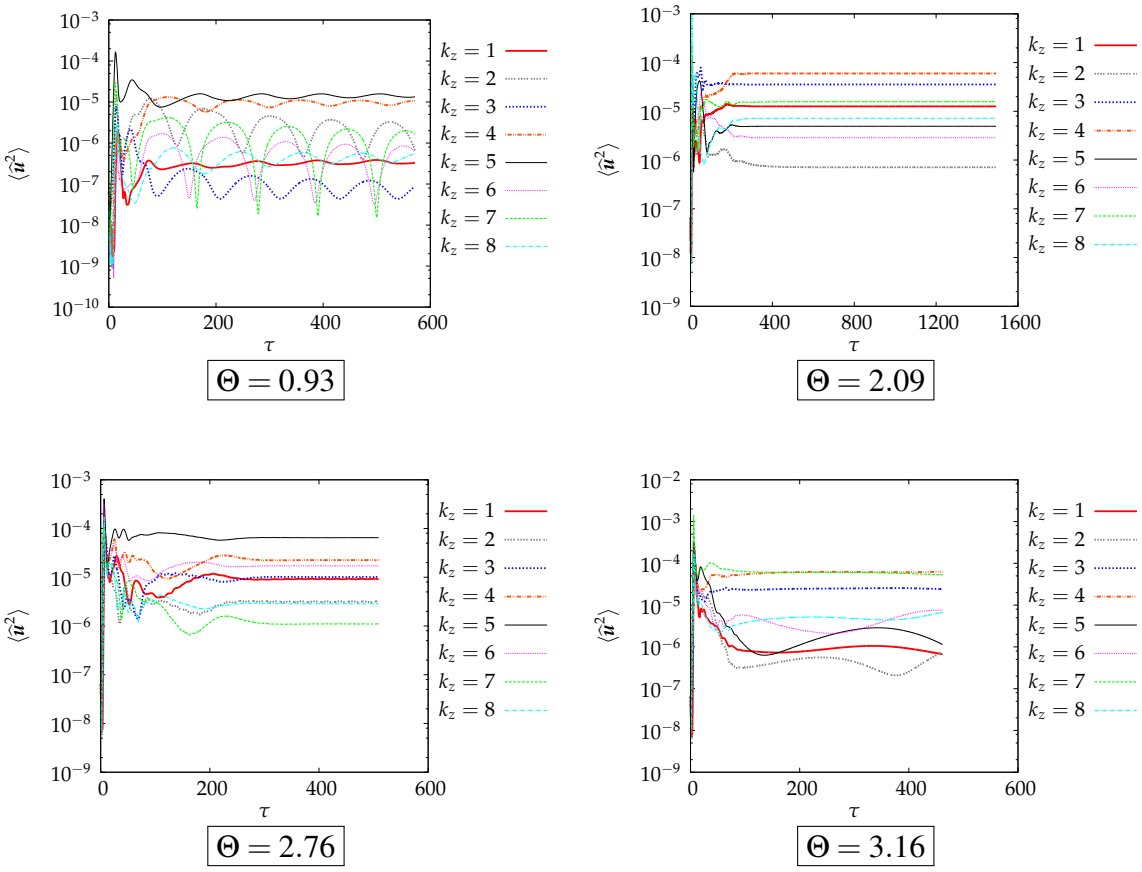

Figure 4.39: Time evolution of the kinetic energy contained in the first axial modes for $M = 634$ and $Pr = 3$.

the low pinch parameter considered ($\Theta = 0.90$) the dynamics are dominated by the fourth mode. However if the pinch ratio is increased oscillations around the saturated state appear ($\Theta = 1.88$). For this case the dominant mode is still $k_z = 4$, but it has an oscillatory behavior along with the others toroidal modes.

For the highest pinch ratios ($\Theta = 2.38$ and $\Theta = 2.70$), oscillations are presented for a large spectrum of modes. The difference is that the dominant mode is not unique anymore, the amplitudes of the oscillations are larger and, in time, different modes possess the biggest kinetic energy. The dominant axial modes are 4, 5, 6 and 8 for the case with $\Theta = 2.38$. For the greatest pinch parameter ($\Theta = 2.70$) the dominant ones are 4, 5 and 7. The kinetic spectrum becomes flatter and we can say that a fully turbulent state starts to emerge.

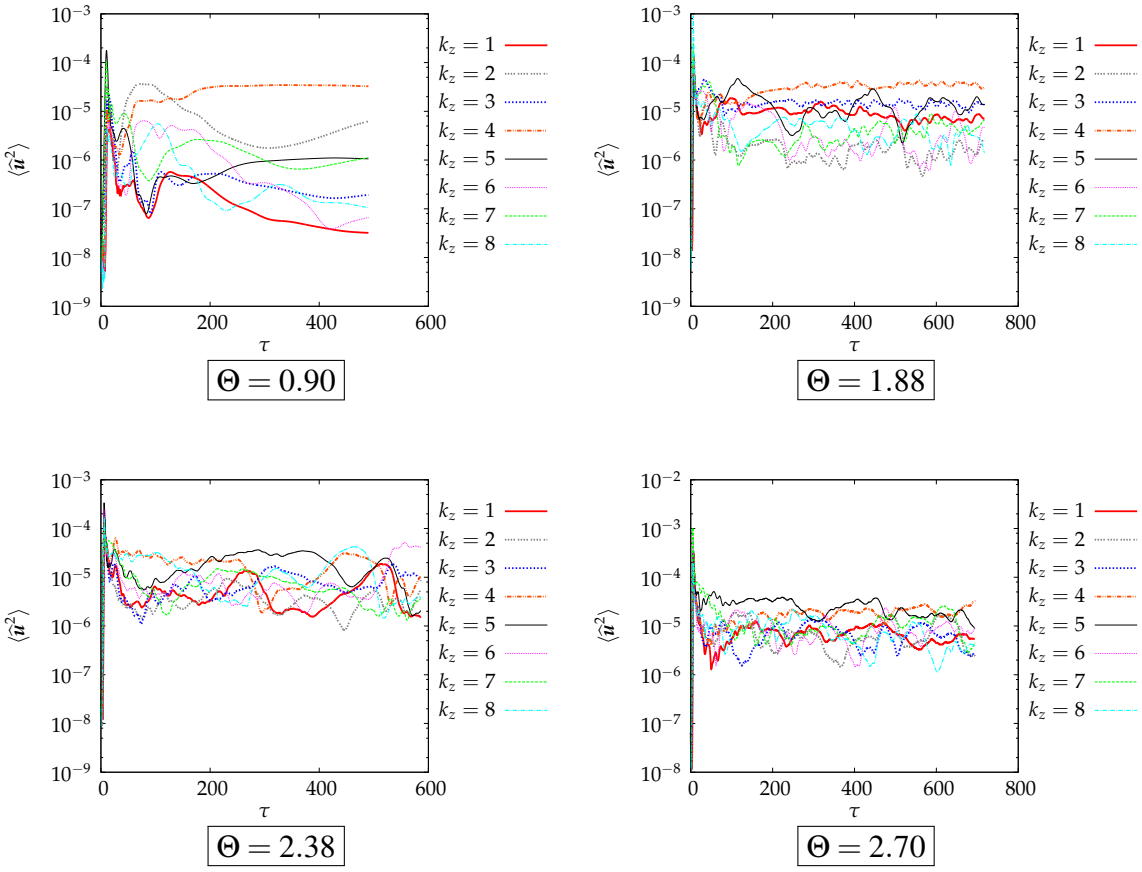

Figure 4.40: Time evolution of the kinetic energy contained in the first axial modes for $M = 1902$ and $Pr = 2$.

4 COMPARISON BETWEEN THE RESULTS IN TOROIDAL AND CYLINDRICAL GEOMETRY

4.1 INTERCOMPARISON OF THE SIMULATIONS

The two studied geometries show similarities in the final dynamics of the magnetofluid. Both cases at the final times develop helical configurations if the pinch ratio is sufficiently increased, and the fourth toroidal (or axial) mode prevails in the majority of computed helical cases.

The fundamental difference appearing between the two geometries is the absence of the zero mode for the cylindrical cases. For the toroidal geometry, at low pinch parameter, the flow is an axisymmetric velocity field that with increasing Θ has a transition to a state, where a dominant helical flow is superposed on the original axisymmetric field.

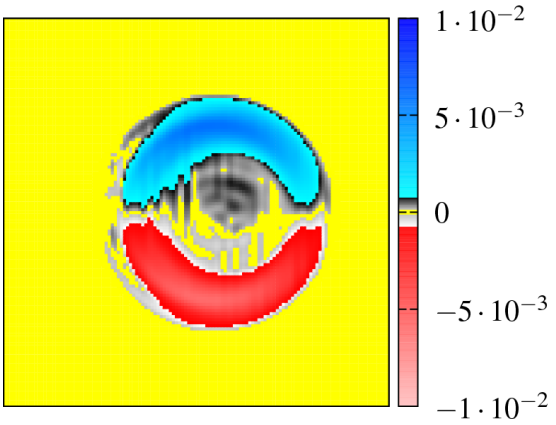

Figure 4.41: Torus: time and azimuthally averaged toroidal velocity for $M = 658$, $Pr = 3$ and $\Theta = 1.57$.

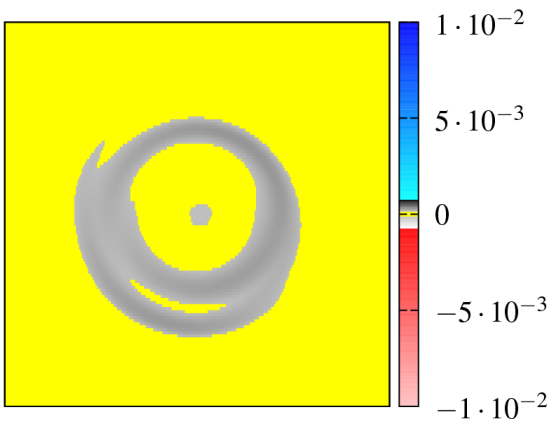

Figure 4.42: Cylinder: time and axially averaged axial velocity for $M = 1902$, $Pr = 2$ and $\Theta = 1.88$.

To illustrate the difference between the flow in the cylinder and the torus we take one simulation in each geometry. For the velocity field we perform a time average at the steady state and then a second spatial average in the azimuthal direction for the toroidal geometry and in the axial direction for the cylindrical case. A time average is performed because for both considered cases at the steady state we have an oscillatory evolution of the magnetofluid. The image resulting of this average is presented in Fig. 4.41 for the toroidal geometry ($M = 658$, $Pr = 3$ and $\Theta = 1.57$) and in Fig. 4.42 for the cylinder ($M = 1902$, $Pr = 2$ and $\Theta = 1.88$). In the toroidal result we can visualize clearly the two axisymmetric regions with opposite toroidal velocity. The maxima are located near the boundaries and surround a circular region with small toroidal velocity. On the other hand, in the cylindrical case, the time and axial average give an axial velocity field which is negligible compared to the toroidal case.

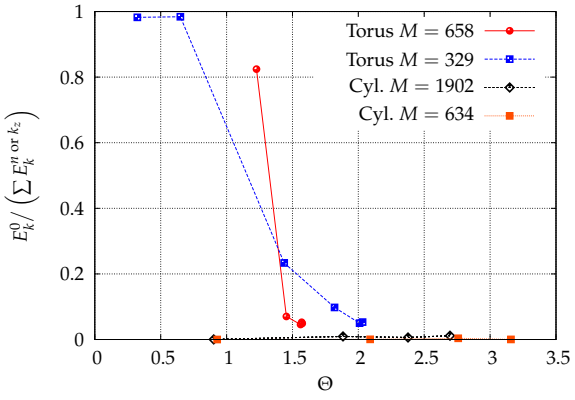

Figure 4.43: Ratio of the zero (toroidal or axial) mode kinetic energy over the total kinetic energy for the toroidal and cylindrical geometries as a function of Θ.

Another way to apprehend this difference between the toroidal and cylindrical flow is

to see the ratio of the kinetic energy of the zero mode over the total kinetic energy (see Fig. 4.43). For $M = 329$ in the toroidal configuration the energy is mainly concentrated in the zero toroidal mode at low pinch ratio, after the transition between $\Theta = 0.65$ and $\Theta = 1.44$ the zero mode energy falls but does not reach a negligible value. The same behavior is observed for the toroidal case with $M = 658$, where for the greatest Θ the energy in the zero toroidal mode is small, but still constitutes several percent of the total kinetic energy. For the cylindrical case for all the considered pinch ratios the energy of the zero axial mode is always negligible compared the other modes of the spectrum. It is always inferior to 1.2% of the total energy.

The time evolution of the kinetic energy also shows a different trend. For the toroidal case rapidly a kinetic energy appears at the poloidal Alfvén time $\tau = 1$ when the axisymmetric velocity field emerges. Subsequently the helical instability arises and makes the kinetic energy increase around $\tau = 5$. For the cylinder case we have also the instability that develops after $\tau = 5$ but before that there is no increase of the kinetic energy, the energy remains below 10^{-5}. This is the energy of the initial perturbation that decays to zero if the threshold of the helical instability is not reached.

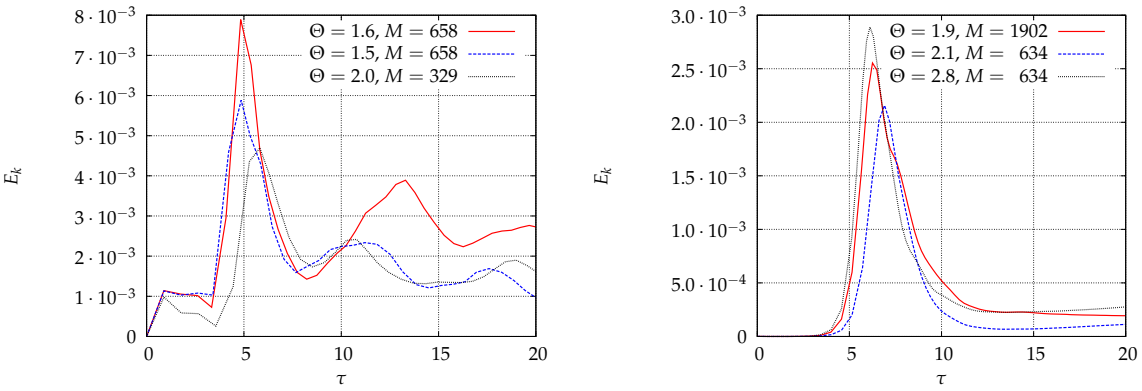

Figure 4.44: Kinetic energy evolution at the early times for the toroidal (left) and the cylindrical geometry (right).

4.2 COMPARISON WITH EXPERIMENTAL DATA

The numerical results are compared to experimental data of three different RFP devices. The first experimental data comes from the REPUTE experiment, that is described in [106, 107], the second set of data is the RFP ZT-40M [106, 29] and the third is from the device RELAX [43]. This last experiment has a low aspect ratio, $\Gamma = 2$, close to the aspect ratio used in the present simulations. This device has the particularity to allow Θ to be greater than two, whereas for the majority of RFP experiments the pinch ratio is around 1.5. In RELAX a distinctive deep-reversal configuration of the toroidal magnetic field is found where the flow is characterized by a low level of fluctuations [43, 44]. In Fig. 4.45 the numerical and the experimental results are presented in the $\Theta - F$ plane. We also show

the theoretical curve found by Taylor [105] that has been recently critically reviewed in [19] with respect to its relevance to the RFP dynamics.

From the figure we can see that the numerical calculations give similar results compared to the RFP experiments in the $\Theta - F$ plane: we have the decrease of the F parameter with the increase of the pinch ratio (Figs. 4.45 and 4.46). The reversal of the toroidal magnetic field B_T for the considered experiments occurs around the same value, for $\Theta \approx 1.5$. The numerical calculation that fits the best the experiments is the one performed for a toroidal geometry with $Pr = 3$ and viscous Lundquist number $M = 658$. In this figure we note that the geometry and the viscous Lundquist number play an important role in the evolution of the reversal parameter F with Θ. We see that increasing the viscous Lundquist number, the value of Θ, that corresponds to $F = 0$, decreases.

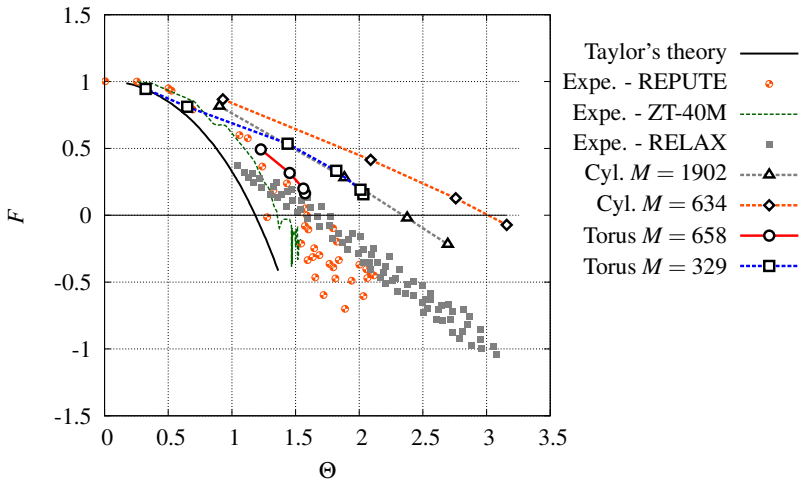

Figure 4.45: Field reversal parameter F as a function of the pinch parameter Θ for different viscous Lundquist numbers, $Pr = 3$ for the toroidal simulations and for the cylindrical case with $M = 634$ and $Pr = 2$ for the cylindrical calculation with $M = 1902$. Also experimental data of three RFP devices.

It seems that, using the toroidal geometry and increasing sufficiently the viscous Lundquist number as well as the magnetic Prandtl number, we fit better the experimental data. We do not know at present whether we could get a magnetic toroidal reversal at the torus edge for high enough values of M. In this study the computational resources were not sufficient to carry out higher resolution computations in order to investigate higher values of the Lundquist and Prandtl numbers. It will be possible in a close future to perform such simulations and to check if we can reach the region, in parameter space, where the toroidal magnetic field reverses.

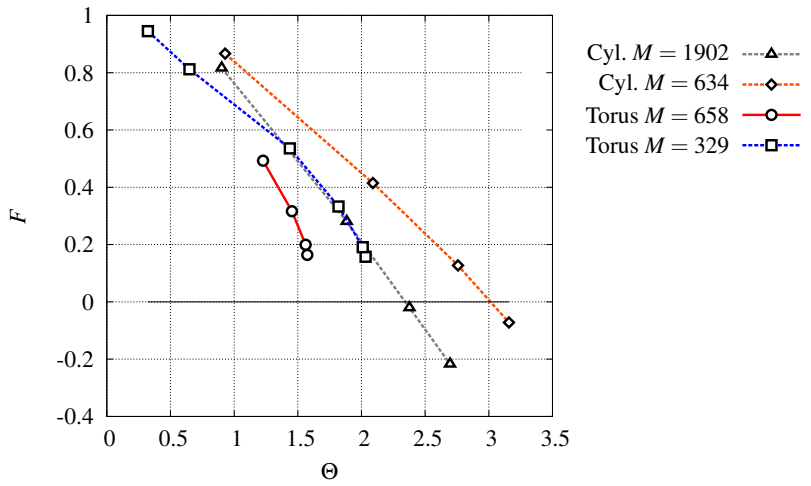

Figure 4.46: Field reversal parameter F as a function of the pinch parameter Θ for different viscous Lundquist numbers, $Pr = 3$ for the toroidal simulations and for the cylindrical case with $M = 634$ and $Pr = 2$ for the cylindrical calculation with $M = 1902$.

5 CONCLUDING REMARKS ABOUT THE TOROIDAL AND CYLINDRICAL SIMULATIONS

The toroidal and cylindrical simulations carried out in the present study help to understand the similarities and differences that appear between these two geometries. The helical instability appearing for increasing pinch ratio is quite similar for both cases. Generally, if the viscous Lundquist number is not too important, a single helical mode dominates the system, so that we are close to the quasi-single helicity state found in experiments. For increasing viscous Lundquist number an oscillatory steady state is found in both geometries. A turbulent state appears for the cylindrical case at large M number and pinch ratio. It can be expected that a similar turbulent state will appear in the toroidal configuration if the viscous Lundquist number is sufficiently increased.

The fundamental qualitative difference between the cylinder and the torus is the axisymmetric or axially invariant flow that disappears in the cylindrical configuration. The toroidally invariant poloidal flow is composed of two counterotating vortices. This flow topology has been found experimentally [10], and in a straight cylinder this important characteristic of the plasma dynamics is lost.

In summary, despite some qualitative similarities between the dynamics in the two geometries, we stress that quantitatively the differences are quite large. We believe that the curvature of the toroidal geometry needs to be taken into account to correctly reproduce the experimental flow measurements.

V

CONCLUSION

The objective of this thesis project was to study the dynamics of a magnetofluid in a toroidal geometry by the means of the incompressible, isothermal, viscoresistive magnetohydrodynamic model with constant transport coefficients. Using this simplified model many characteristics of a real fusion plasma are not taken into account. Hence we study the dynamics of a plasma without many of its complexities. The advantage of this approach is that basic phenomena can be easily identified. Naturally more realistic characteristics could be introduced later on, one at a time, and a separation of the different phenomena that influence a more realistic plasma dynamics could then be highlighted. We believe that, in this way, a better understanding of the dynamical system can be achieved.

First, in Chap. II, a novel numerical method to solve the MHD equations in toroidal geometries is presented, where a forcing term, added to the Navier-Stokes and the magnetic induction equations, allows to take into account Dirichlet boundary conditions in a pseudo-spectral algorithm. The advantage of the method is that the considered geometry can easily be modified. As an example, in this manuscript the MHD equations were solved in different toroidal and cylindrical configurations.

In Chap. III, where we applied this method to investigate the behavior of MHD in toroidal geometry, we showed that the presence of an irrotational toroidal electric and magnetic field in a toroidal configuration automatically produces velocities even in the absence of MHD instabilities. Therefore under the assumptions we used, no static equilibrium is possible. If one would like to describe toroidal plasma dynamics as perturbations around an equilibrium state, this state must therefore be necessarily dynamic. The velocities for high values of the viscosity and resistivity are mainly located in the poloidal plane, but for increasing nonlinearity and for a large safety factor the toroidal velocity component considerably increases and dominates the dynamics. Also it is observed that if an up-down asymmetric cross section of the torus is considered, a net toroidal angular

momentum appears, a feature which is also observed in experiments.

For a toroidal magnetofluid, where the imposed helical magnetic field is characterized by a small safety factor (or large pinch ratio), more complex dynamics are found. In this case a transition from an axisymmetric flow field to a helical configuration is observed. This helical topology resembles the quasi-single helicity state found in RFP experiments. For increasing nonlinearity and pinch ratio a transition to a fully turbulent system can be achieved. It is shown, that even though some similar features are present in both, the cylindrical and toroidal geometry, important differences exist between the flow topology observed in them, both qualitatively and quantitatively. Also the comparison with experimental data shows a better agreement if the toroidal geometry is considered.

PERSPECTIVES

The physics of toroidally confined fusion plasmas is very rich and almost every aspect of it can constitute a research field on its own. The MHD model we use can be improved in many ways to approach reality. However, one should be careful not to exaggerate this complexification. Indeed the goal of a description such as MHD is not, in our opinion, to build a numerical fusion reactor but to isolate key physical mechanisms that can help to better understand the plasma dynamics. This understanding can then guide experimentalists in interpreting experimental results in order to improve magnetic fusion configurations. Considering too many features at once can perhaps diminish the gap between numerical and experimental observations, but does not necessarily lead to better understanding. With this in mind we propose here several perspectives, favouring the ones which are most simple to consider and which, possibly, have the biggest impact on the observed plasma behavior.

In the present manuscript, the magnetic Prandtl number was kept close to unity. Experimentally it is difficult to assess the real viscosity value of a plasma, so it seems interesting to perform a parametric study varying the Prandtl number over several orders of magnitude to quantify its influence on the dynamics of the system. This is one of the practically most simple perspectives since it does not need any modification of the numerical code, as long as sufficient numerical resources are available.

The influence of the shape of the domain on the RFP dynamics and in particular on the appearance of quasi-single helicity states deserves definitely further investigation.

The model considered in the present study can further be developed. The first step could be the introduction of a profile for the resistivity. In this way, the dependence of the resistivity on the temperature can be taken into account. A more realistic way to include the influence of non-uniform transport coefficients is to include an evolution equation for the temperature. This, and including the effects of finite compressibility, will necessitate a non negligible effort, notably with respect to the introduction of the penalization term in the energy and in the continuity equations [55].

Another perspective, which is not directly related to the field of magnetic fusion, is the use of the numerical code to study less complex plasma experiments that can be used for a more fundamental understanding of the plasma physics. An example is the preliminary study of a plasma dynamo presented in Appendix F.

A

THEORETICAL ANALYSIS OF THE HERMITE REGULARIZATION

1 ANALYSIS OF A MODEL PROBLEM

In this section a theoretical analysis of the one-dimensional penalized Poisson equation imposing Dirichlet boundary condition is conducted, and the order of convergence yielded by the Hermite regularization method will be characterized and compared to the classical penalization.
The unpenalized problem in [-1;0] reads:

$$\begin{cases} -u'' = 0 \\ u(-1) = 0,\ u(0) = \frac{1}{2} \end{cases}$$

The penalized problem is solved in the interval [-1;1]:

$$\begin{cases} -u'' = -\frac{\chi}{\eta}(u - u_{wall}) \\ u(-1) = 0,\ u(1) = u_{wall}(1) \end{cases} \quad \text{with } \chi = \begin{cases} 0 \text{ in } \Omega_f = [-1;0[\\ 1 \text{ in } \Omega_s = [\,0;1] \end{cases} \tag{A.1}$$

At the fluid-solid interface we impose the continuity condition $u_s(x) = u_f(x),\ u_s'(x) = u_f'(x)$ for $x = 0$.
For the classical penalization, we set $u_{wall} = \frac{1}{2}$ and thus $u_{wall}(1) = \frac{1}{2}$. The solutions are

$$\begin{cases} u_f(x) = a(x+1),\ u_s(x) = K_1 e^{\frac{x}{\sqrt{\eta}}} + K_2 e^{\frac{-x}{\sqrt{\eta}}} + \frac{1}{2} \\ \text{with } a = \frac{\alpha(e_*^2-1)}{2(\alpha-1-e_*^2-e_*^2\alpha)} + \frac{1}{2} \\ \text{and } K_1 = \frac{-\alpha}{2(\alpha-1-e_*^2-e_*^2\alpha)},\ K_2 = \frac{\alpha e_*^2}{2(\alpha-1-e_*^2-e_*^2\alpha)} \end{cases}$$

where $\alpha = \sqrt{\eta}$ and $e_* = e^{\frac{1}{\sqrt{\eta}}}$. The subscripts 's' and 'f' stand for the solid and the fluid domain, respectively.

For the penalization with the regularization method, the interpolating polynomial must be defined first. An Hermite interpolation consists in finding a polynomial which fits two separate points where the values of the function and of a chosen number of derivatives are imposed. In our case the Hermite polynomial $H(x)$ must match the values of u and its first derivative at $x = 0$ and yields $H(1) = H'(1) = 0$ at $x = 1$. As the exact solution of the unpenalized problem is $u(x) = \frac{x+1}{2}$, the expression of the third degree Hermite polynomial can be easily derived:

$$\begin{cases} H(0) = \frac{1}{2},\ H'(0) = \frac{1}{2},\ H(1) = 0,\ H'(1) = 0 \\ H(x) = \frac{3x^3}{2} - \frac{5x^2}{2} + \frac{x}{2} + \frac{1}{2} \end{cases}$$

In equation (A.1), $H(x)$ is set as u_{wall} and, with the same notations as before, the solutions are

$$\begin{cases} u_f(x) = a(x+1),\ u_s(x) = K_1 e^{\frac{x}{\sqrt{\eta}}} + K_2 e^{\frac{-x}{\sqrt{\eta}}} + H(x) + (9x-5)\eta \\ \text{with } a = \frac{14\alpha^3(1-e_*^2)+8\alpha^2 e}{\alpha-1-e_*^2-e_*^2\alpha} + \frac{1}{2} - 5\alpha^2 \\ \text{and } K_1 = \frac{14\alpha^3+4\alpha^2 e_*(\alpha+1)}{\alpha-1-e_*^2-e_*^2\alpha},\ K_2 = \frac{-14\alpha^3 e_*^2-4\alpha^2 e_*(\alpha-1)}{\alpha-1-e_*^2-e_*^2\alpha} \end{cases}$$

Figure A.1 shows the exact profiles of the solution of the Poisson equation in [-1,0[and the penalization term in [0,1]. The solution of the penalized problem should converge to these profiles when $\eta \to 0$.

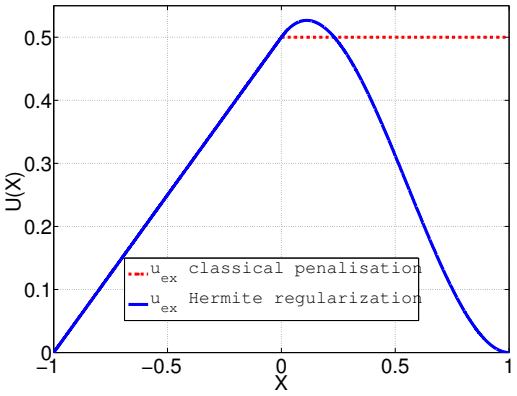

Figure A.1: Exact solution with the different penalization methods. With the regularization method, the solution is C^1 on the whole domain.

These solutions are compared to the exact solutions $u_f = \frac{x+1}{2}$ and $u_s = \frac{1}{2}$ in Fig. A.2 for different values of the penalization parameter η. It can be seen that both converge rapidly to the theoretical solutions when η becomes smaller.

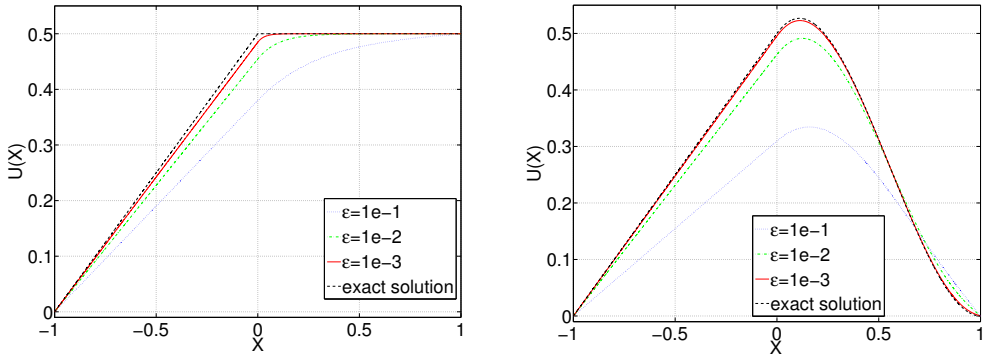

Figure A.2: Solutions of the penalized problem for various values of η for the classical (left) and regularized penalization method (right).

From Fig. A.3, the same can be observed for the first derivative (top). The second derivatives (bottom) do not fit very well but the results are smoother in the case of the Hermite interpolation. Eventually the class of the function is increased with the second method, as expected.

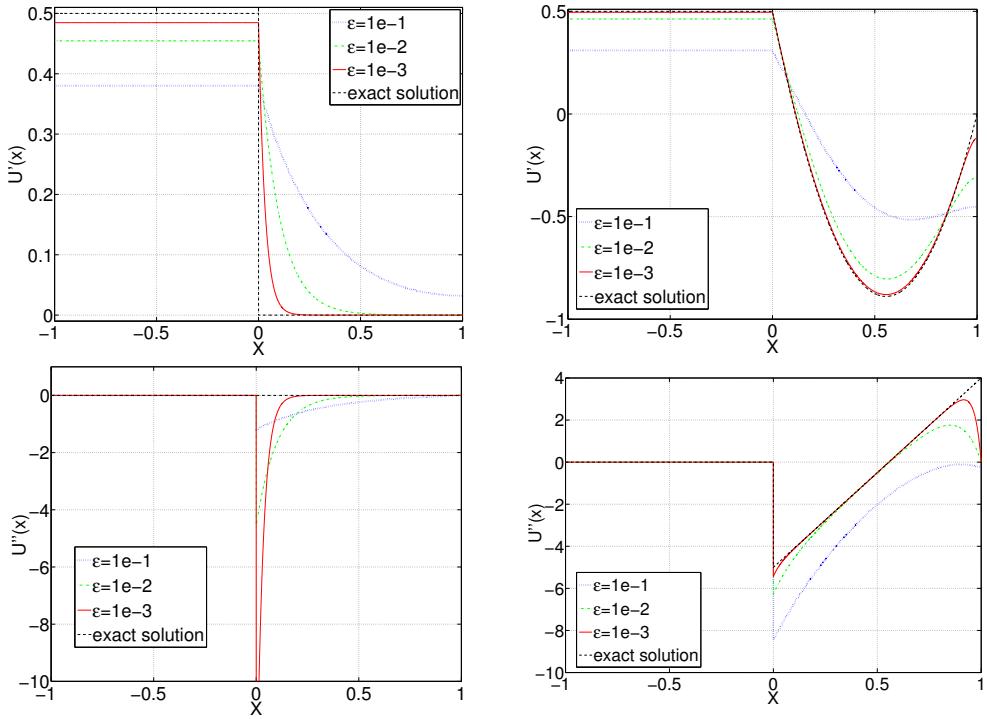

Figure A.3: First (top) and second derivative (bottom) of the solution of the penalized problem for the classical (left) and regularized penalization method (right).

2 EVALUATION OF THE ERROR

The penalization error in the L_2 norm can be computed directly as

$$||\varepsilon||_2^2 = \int_{-1}^{0} (u_\eta - u_{exact})^2 dx = \int_{-1}^{0} (a(x+1) - \frac{x+1}{2})^2 dx = \frac{(1-2a)^2}{12}$$

Then the coefficient a is replaced by the corresponding expressions obtained above in the two cases and the error becomes :

$$\begin{cases} ||\varepsilon||_2 = |\frac{(1-2a)}{\sqrt{12}}| \\ \text{classical penalization} : ||\varepsilon||_2 = \frac{\sqrt{\eta}}{\sqrt{12}} \\ \text{hermite penalization} : ||\varepsilon||_2 = \frac{10\eta}{\sqrt{12}} \end{cases}$$

The convergence results are confirmed by the numerical experiments shown in Fig. A.4. The penalized solutions are plotted for several values of $\eta = [10^{-1}, 10^{-2}, 10^{-3}, 10^{-4}, 10^{-5}]$ and the errors with respect to the exact profiles are computed in the L_2 and L_∞ norms. The order of convergence is indeed improved to η for the regularization method instead of $\sqrt{\eta}$ with the classical penalization.

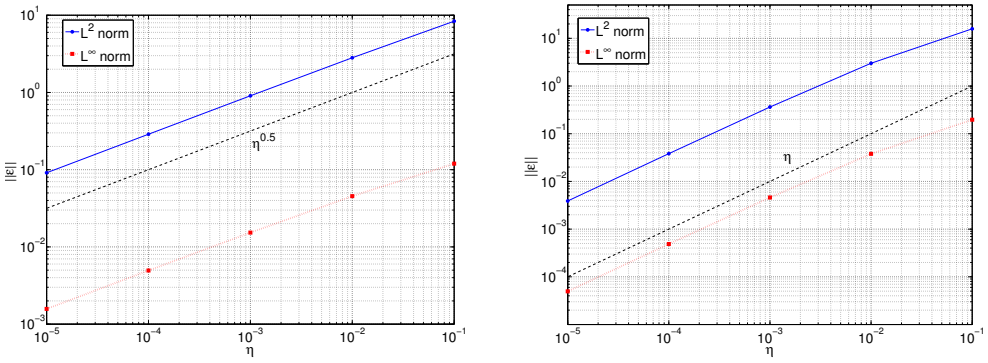

Figure A.4: Penalization errors of u_η as a function of η for classical (left) and regularized penalization method (right).

The errors are also presented for the first and second derivative (Fig.A.5). It must be noticed that the error for the second derivative in the case of the regularized penalization method still improves when η decreases, whereas it increases for the classical method.

The order of convergence obtained in Chap. II sections 5.1 and 5.2 is higher than the one obtained here. This could result from the dissipative terms in the Navier–Stokes and induction equations, which are not present here. This term smoothens the remaining discontinuities and improves the order of convergence. The principal drawback of this method is that a baseflow must be known to precompute the regularization term.

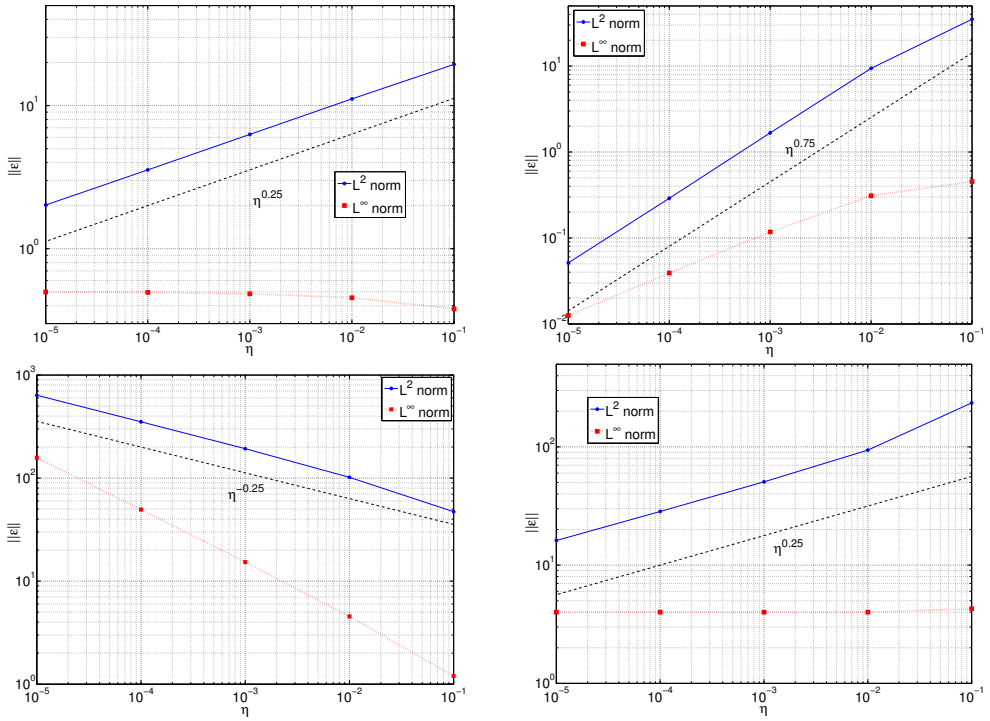

Figure A.5: Penalization errors of u'_η (top) and u''_η (bottom) as a function of η for classical (left) and regularized penalization method (right).

Moreover, it is possible that this baseflow is not continuous if in the numerical solution instabilities appear. As further perspective, this method should be implemented actively so that the regularization term fits the numerical solution as closely as possible at each time-step.

B

IMPOSING NON HOMOGENEOUS NEUMANN BOUNDARY CONDITIONS WITH A PENALIZATION METHOD

1 FORMULATION

A generalization of the volume penalization method to impose non homogeneous Neumann boundary conditions (BC) will be explained in the following.

The advection-diffusion equation of a scalar field $\theta(t,\boldsymbol{x})$ is considered in a domain Ω,

$$\frac{\partial \theta}{\partial t} + u_j \partial_j \theta = \alpha \Delta \theta, \tag{B.1}$$

$$\nabla \theta|_{\partial\Omega} = \gamma_{wall}, \quad \theta(t=0,\boldsymbol{x}) = f_0(\boldsymbol{x}). \tag{B.2}$$

Taking the gradient of this equation we can obtain a system of advection-diffusion equations for the different components of the gradient of θ, denoted by $\gamma_i = \partial_i \theta$. The penalization term is added and inhomogeneous Dirichlet conditions are imposed on γ_i,

$$\frac{\partial \gamma_i}{\partial t} + \partial_i (u_j \partial_j \theta) = \alpha \Delta \gamma_i - \frac{\chi(\boldsymbol{x})}{\eta} (\gamma_i - \gamma_{i_{wall}}). \tag{B.3}$$

We use a Fourier pseudo-spectral method and thus periodic boundary conditions are applied at the edge of the computational domain for the imposed $\gamma_{i_{wall}}$.

The next step is to integrate this last equation in space to recover the equation for θ. To do so we apply the divergence operator to the system of equations (B.3). Using the

relation $\nabla \cdot (\nabla f) = \Delta f$, the Laplace operator appears in the equation. Thus to recover the equation for θ a Poisson equation has to be solved. In spectral space this is equivalent to multiply the equation (B.3) by the operator $\imath k_i / k^2$,

$$\hat{\theta}(\boldsymbol{k}) = \frac{-\imath k_i}{k^2} \hat{\gamma}_i(\boldsymbol{k}). \tag{B.4}$$

with $k \neq 0$. In consequence, in physical space, the advection-diffusion equation with the penalization term for the gradient, can be written:

$$\frac{\partial \theta}{\partial t} + u_j \partial_j \theta = \alpha \Delta \theta + \mathscr{F}^{-1} \left[\frac{\imath k_i}{k^2} \mathscr{F} \left\{ \frac{\chi(\boldsymbol{x})}{\eta} (\gamma_i - \gamma_{i_{wall}}) \right\} \right]. \tag{B.5}$$

This last equation can be solved numerically with a pseudo-spectral method and the solution of the advection-diffusion equation with non homogeneous Neumann boundary conditions can thus be obtained.

To verify this numerical method a one-dimensional test case is presented in the next section considering an instationary diffusion problem with non homogeneous Neumann boundary conditions. A different numerical method to take into account homogeneous boundary conditions using spectral methods is presented in [49].

2 TEST CASE: ONE-DIMENSIONAL INSTATIONARY DIFFUSION PROBLEM

We consider the instationary diffusion equation for the temperature $\theta(x,t)$, with a positive heat flux on the left and right boundaries (see Fig.B.1). The equation to be solved is the following,

$$\frac{\partial \theta(x,t)}{\partial t} = \nabla^2 \theta(x,t), \tag{B.6}$$

with non homogeneous Neumann boundary conditions at $x = a$ and $x = b$,

$$\left. \frac{\partial \theta}{\partial x} \right|_{x=a} = -q \quad \text{and} \quad \left. \frac{\partial \theta}{\partial x} \right|_{x=b} = q. \tag{B.7}$$

The solution of this system is a combination of a parabolic function in space and a linear time evolution,

$$\theta(x,t) = q(x-a) \left(\frac{(x-a)}{(b-a)} - 1 \right) + \frac{2q}{(b-a)} t. \tag{B.8}$$

The initial condition chosen for the simulation is the parabolic function that respects the inhomogeneous boundary conditions,

$$\theta(x,0) = q(x-a) \left(\frac{(x-a)}{(b-a)} - 1 \right). \tag{B.9}$$

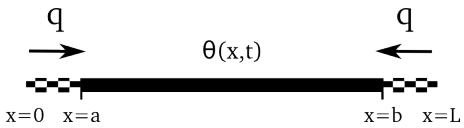

Figure B.1: One dimensional diffusion problem scheme for positive heat fluxes at the boundaries.

Numerically the diffusion equation is advanced in time and the two non homogeneous Neumann boundary conditions are taken into account with a penalization term,

$$\frac{\partial \theta(x,t)}{\partial t} = \Delta\theta(x,t) + \underbrace{\mathscr{F}^{-1}\left[\frac{\imath k_i}{k^2}\mathscr{F}\left\{\frac{\chi(x)}{\eta}\left(\gamma_i(x)-\gamma_{i_{wall}}(x)\right)\right\}\right]}_{\text{Non homogeneous Neumann BC term}}. \tag{B.10}$$

In Fig. B.1 the external region (small rectangles) and the internal region (black line) are visualized. On the border of the domain the periodicity must be ensured and therefore a zero gradient of θ is imposed at $x = 0$ and $x = L$. For this reason we impose a linear evolution of the gradient ($\gamma_{i_{wall}}(x)$) in the solid region,

$$\gamma_{i_{wall}}(x)\big|_{x\in[0,a]} = \frac{-q}{a}x, \qquad \gamma_{i_{wall}}(x)\big|_{x\in[b,L]} = \frac{q}{L-b}(L-x). \tag{B.11}$$

Hence we verify the Neumann boundary conditions at $x = a$ and $x = b$, as well as the periodicity at the edge of the computational domain.

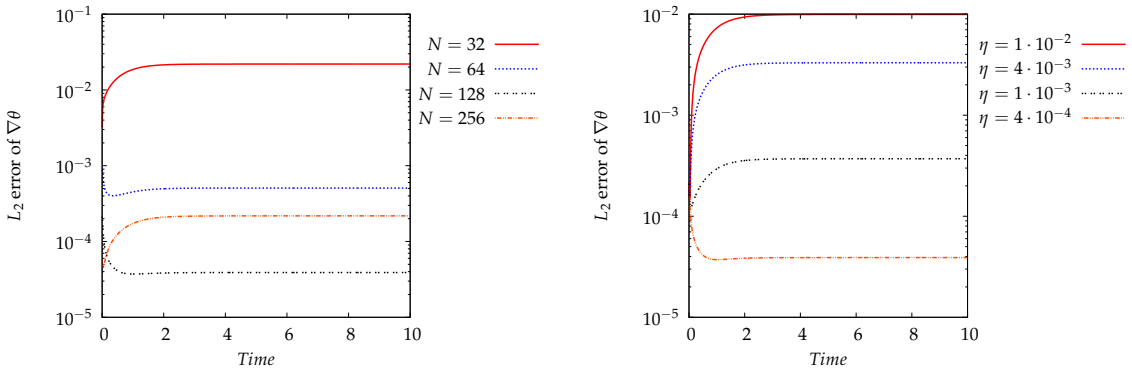

Figure B.2: Time evolution of the L_2 error for the gradient of θ, between the numerical results and the exact solution, for different resolutions, N (left) and penalization parameters, η (right).

We obtain numerically the solution of the Laplace equation (B.6) with the imposed Neumann boundary conditions. The computations are performed in a domain size $L = 2\pi$ taking into account different resolutions (N) and penalization parameters (η). The numerical error for the gradient of the temperature ($\nabla\theta$) is calculated. The time evolution of the L_2-norm error is presented, for different values of N and η, in Fig. B.2. There is a convergence of the error on a finite time. The computations with varying N are performed with $\eta = 4\cdot10^{-4}$ and those with varying η have a constant resolution $N = 128$.

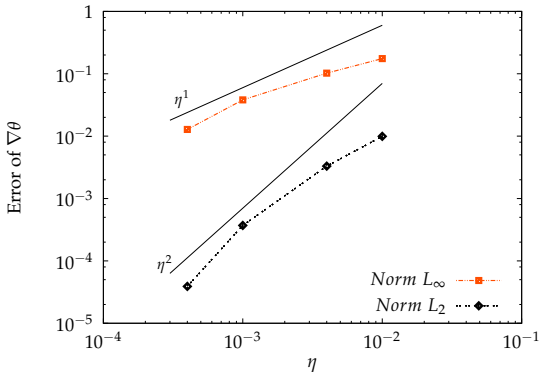

Figure B.3: Evolution of the L_∞ and L_2 errors for the gradient of θ as a function of the penalization parameters (η).

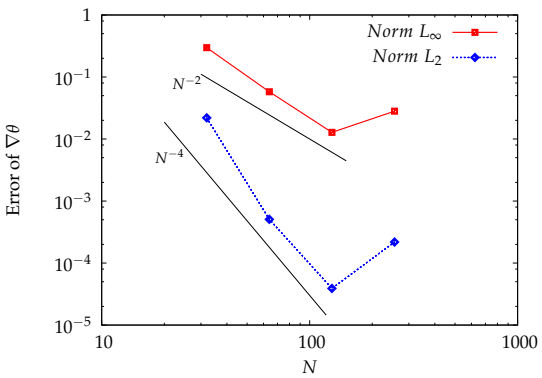

Figure B.4: Evolution of the L_∞ and L_2 errors for the gradient of θ as a function of the grid points (N).

At the steady state (when the error between the numerical results and the exact solution is constant in time) we can evaluate the different error norm and compute their convergence as a function of the penalization parameter and the resolution. The Fig. B.3 presents the convergence of two error norms with η. With the penalization parameter second order convergence for the L_2 error and a first order for the norm L_∞ are obtained. With the resolution (Fig. B.4) we have a fourth order convergence for L_2 and a second order for the L_∞ error.

C

CORRESPONDING EXPLICIT SCHEME OF THE SEMI-IMPLICIT PENALIZATION METHOD

Jause-Labert *et al.* [47] extended an implicit formulation for the time-integration scheme for Dirichlet conditions, originally proposed by Kolomenskiy and Schneider [52] for Burgers' equation, to relax the constraint on the choice of the time-step. Their approach is discussed in some detail in this section. We use the following form of the penalized Navier–Stokes equation:

$$\partial_t u = \xi - \partial_x P - \frac{\chi}{\eta} u, \tag{C.1}$$

in this equation $u_{wall} = 0$, $P + u^2/2 \to P$ and ξ represents the nonlinear term. The viscous term can simply be added in the integral form, $u \exp(-\nu k^2 t) \to u$. In Fourier space we can write

$$\partial_t \hat{u} = P_\perp \left(\hat{\xi} - \frac{1}{\eta} \widehat{\chi u} \right). \tag{C.2}$$

with $P_\perp$ the Riesz projection-operator. The implicit treatment for the penalization term at the first order implies

$$\frac{\hat{u}^{n+1} - \hat{u}^n}{\Delta t} = P_\perp \left(\hat{\xi}^n - \frac{1}{\eta} \widehat{\chi u}^{n+1} \right), \tag{C.3}$$

the fact that in the last term the $\hat{\chi}$ is convoluted with $\hat{u}^{n+1}$ makes it non-trivial to write the implicit formulation. The following formulation is proposed [47]:

$$\hat{u}^{n+1} = P_\perp \mathscr{F} \left(\frac{u^n + \Delta t \, \mathscr{F}^{-1} \left[P_\perp \hat{\xi}^n \right]}{1 + \frac{\chi^{n+1}}{\eta} \Delta t} \right). \tag{C.4}$$

We know that the χ function takes only the values 0 and 1 depending if we are in the fluid or in the solid region respectively,

$$\chi(\boldsymbol{x},t) = \begin{cases} 0 & \text{for } \boldsymbol{x} \in \Omega_f, \text{the fluid domain} \\ 1 & \text{for } \boldsymbol{x} \in \Omega_s, \text{the solid domain.} \end{cases} \tag{C.5}$$

An equivalent form of the Eq. (C.4) can be written as follows

$$\hat{u}^{n+1} = P_\perp \mathscr{F}\left[\left(u^n + \Delta t\, \mathscr{F}^{-1}\left[P_\perp \hat{\xi}^n\right]\right)\left(1 - \chi^{n+1}\frac{\Delta t}{\eta + \Delta t}\right)\right]. \tag{C.6}$$

We recover the Navier–Stokes equation in the fluid domain and the implicit penalized equation (C.4) in the solid region. Using the following relations

$$\begin{aligned} P_\perp P_\perp \hat{a} &= P_\perp \hat{a} \\ P_\perp \hat{u} &= \hat{u}, \end{aligned} \tag{C.7}$$

the differential form of Eq. (C.6) can be written

$$\partial_t \hat{u} = P_\perp\left(P_\perp \hat{\xi} - \frac{\widehat{\chi u}}{\eta + \Delta t} - \frac{\Delta t}{\eta + \Delta t}\mathscr{F}\left\{\chi\, \mathscr{F}^{-1}\left[P_\perp \hat{\xi}\right]\right\}\right). \tag{C.8}$$

Here we can identify two extreme cases. If $\Delta t << \eta$ the equation (C.8) converges towards the equation (C.2), we recover the classical penalized Navier–Stokes equation. On the other hand if $\eta << \Delta t$ we recover the following equation:

$$\partial_t \hat{u} = P_\perp\left(\mathscr{F}\left\{(1-\chi)\,\mathscr{F}^{-1}\left[P_\perp \hat{\xi}\right]\right\} - \frac{\widehat{\chi u}}{\Delta t}\right). \tag{C.9}$$

This equation is very close to the classical penalized Navier–Stokes equation. Here the time step (Δt) replaces the penalization parameter (η) and the nonlinear term vanishes in the solid region.

The semi-implicit penalization method is in this limit analogous to an explicit formulation. The difference is that, if the penalization parameter is small enough, the porosity of the solid walls is given by the value of the time step.

D

CALCULATION OF THE IMPOSED POLOIDAL MAGNETIC FIELD

We construct the magnetic field satisfying the following properties: (i) it corresponds to a current density profile $\propto 1/R$, (ii) it is parallel to the wall and (iii) it is solenoidal. With respect to our previous investigation [73] the magnetic topology is changed. In fact in that investigation the imposed poloidal magnetic field satisfied the imposed toroidal current density profile $\boldsymbol{j}_{0_T}$ and the solenoidal constraint, but the normal component did not vanish (as is shown in Fig. D.1 (c)). To solve this problem and to satisfy the three desired conditions we obtain $\boldsymbol{B}_{0_{pol}}$ from the current density by writing in terms of a vector potential $\boldsymbol{B}_{0_{pol}} = \nabla \times \boldsymbol{A}_0|_{pol}$, where $\boldsymbol{A}_0 = A_{0_T}\boldsymbol{e}_T$.

The poloidal magnetic field is calculated from the imposed toroidal current density distribution $\boldsymbol{j}_{0_T}$. It can be obtained using the vector potential, $\boldsymbol{B}_{0_{pol}} = \nabla \times \boldsymbol{A}_0|_{pol}$, where $\boldsymbol{A}_0 = A_{0_T}\boldsymbol{e}_T$. Using the Coulomb Gauge we have the following Poisson equation [70],

$$\nabla^2(A_{0_T}\boldsymbol{e}_T) = -\boldsymbol{j}_{0_T}. \tag{D.1}$$

The associated boundary condition is the normal component of the magnetic field vanishing at the boundary of the torus.

It is equivalent and more convenient to work with the magnetic flux function $\chi(R,Z) = RA_{0_T}$, directly. The axisymmetric poloidal magnetic field is easily derived from the flux function $\chi(R,Z)$,

$$\boldsymbol{B}_{0_{pol}} = \nabla\chi \times \nabla T \tag{D.2}$$

with $\nabla T = (1/R)\boldsymbol{e}_T$. Substituting this into Ampère's law, $\nabla \times \boldsymbol{B}_{0_{pol}} = j_{0_T}\boldsymbol{e}_T$ yields

$$\Delta^*\chi = \frac{\partial}{\partial R}\left(\frac{1}{R}\frac{\partial\chi}{\partial R}\right) + \frac{1}{R}\frac{\partial^2\chi}{\partial Z^2} = -j_{0_T}. \tag{D.3}$$

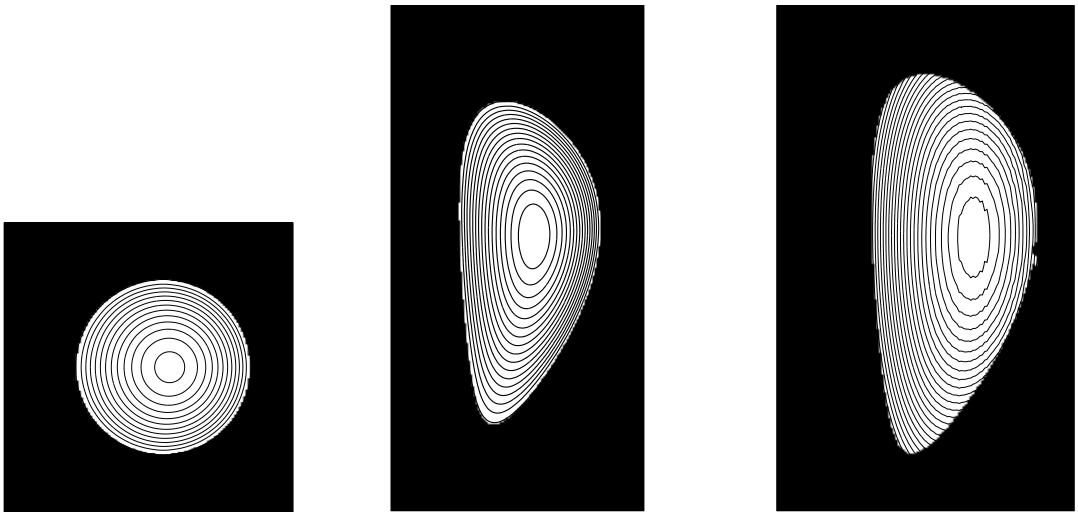

(a) (b) (c)

Figure D.1: Poloidal magnetic field lines ($\chi = RA_{0_T} = constant$) for the different cross sections: (a) symmetric, (b) asymmetric. In (c) we show the field lines for the asymmetric geometry used in Ref. [73].

The boundary condition $\boldsymbol{B}_{0_{pol}} \cdot \boldsymbol{n}\Big|_{wall} = 0$ implies a Dirichlet boundary condition on the magnetic flux function $\chi|_{wall} = constant$.

Numerically the calculation of the poloidal magnetic field $\boldsymbol{B}_{0_{pol}}$ is performed solving the previous Poisson equation for the magnetic flux function χ. This equation is solved with a Fourier spectral method and the volume-penalization technique is used to impose the Dirichlet boundary condition at the wall [75]. The resulting computed equation is the following,

$$\frac{\partial \chi}{\partial t} = \lambda \Delta^* \chi + \lambda j_{0_T} - \underbrace{\frac{\Xi(\boldsymbol{x})}{\eta}(\chi - \chi_{wall})}_{Penalisation\ term}. \tag{D.4}$$

Here λ is a diffusion coefficient ($\lambda = 1$), Ξ is the mask function (it takes the value one in the region where the Poisson equation needs to be solved and zero in the rest of the computational domain) and η is the penalization parameter ($\eta = 5 \cdot 10^{-4}$). The size of the domain is $(2\pi)^3$ for the asymmetric and $(2\pi \times 2\pi \times \pi)$ for the symmetric cross section. The value of the Dirichlet boundary condition is χ_{wall}. This equation is evolved in time, reaching a steady state, numerically $\parallel \chi^{n+1} - \chi^n \parallel < 10^{-6}$. We then recover with sufficient accuracy the solution of the Poisson equation (D.3) taking into account the Dirichlet boundary condition via the penalization term. The solution of this pre-computation will give our basis magnetic field $\boldsymbol{B}_0$ which will be kept constant during the actual simulation.

The resulting poloidal magnetic topology is presented in Fig. D.1 ((a) and (b)) respectively for the considered symmetric and asymmetric geometries (Fig. 3.1).

E

RELATION OF THE DIMENSIONLESS MHD EQUATIONS TO PHYSICAL VALUES FROM THE JET TOKAMAK

The justification of the choice of the parameters we use in our simulations with respect to the experimental values in real life fusion reactors is a difficult exercise, in particular since our assumptions of uniform, scalar transport coefficients are necessarily gross over-simplifications. However, here we present an attempt to estimate the values we would like to use ideally if we would aim to approach physical reality as closely as possible. This estimation is based on the presentation in reference [51].

To determine the dimensionless values that should be introduced in the numerical code we consider the values of the JET experiment [48]. In this device there is a toroidal magnetic field of 28 kG (in SI units $B_{JET} = 2.8\mathrm{T}$), a toroidal current $I = 3.1$ MA, the minor radius is $a = 1.5\,m$ and major radius is $R_0 = 3\,m$. Also we have the plasma density $3.6 \cdot 10^{19}\,m^{-3}$. For our numerical simulations the evolution along the big radius of the imposed dimensionless toroidal electric end magnetic fields are:

$$\boldsymbol{E}_0^*(R) = \tilde{E}^* \frac{R_0}{R} \boldsymbol{e}_T, \tag{E.1}$$

$$\boldsymbol{B}_0^*(R) = \tilde{B}^* \frac{R_0}{R} \boldsymbol{e}_T, \tag{E.2}$$

with R the major radius, r the minor radius, T the toroidal and P the poloidal direction (Fig. E.1). Here and in the following stars indicate dimensionless quantities (*). To determine the dimensionless values $\tilde{E}^*$ and $\tilde{B}^*$ compatible with the JET configuration we

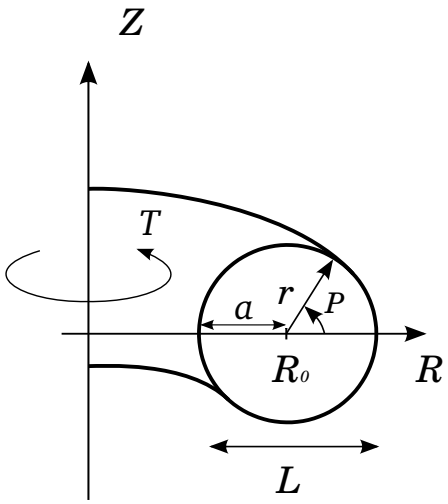

Figure E.1: Toroidal circular geometry.

are going to consider its parameters in SI units. The root mean square value of the toroidal magnetic field is taken to be $B_{JET} = 2.8$T, this is the reference magnetic field.

Note that the reference value of $\boldsymbol{B}$ in our simulation is chosen to be the toroidal magnetic field at $R = R_0$. The value of JET is the surface averaged magnetic field. This introduces a first correction. To find the dimensionless $\tilde{B}^*$ value the integration of $\boldsymbol{B}_0^*$ over the surface of the circular cross section must be equal to one,

$$\frac{1}{A}\int_A \tilde{B}^* \frac{R_0}{R} r dr dP = \frac{1}{A}\int_0^{2\pi}\int_0^a \tilde{B}^* \frac{R_0}{R_0 + r\cos(P)} r dr dP = 1, \tag{E.3}$$

with $a = 1.5\,m$, $R_0 = 3\,m$ and A the area of the cross section (considering a circular cross section $A = \pi a^2$). We calculate this integral using the numerical software Maple. For the circular cross section we find the same value as Kamp and Montgomery [51], which is $\tilde{B}^* = 0.94$. Numerically if the value of the magnetic field is unity it will be in reality $B_{JET} = 2.8$T. Note that the correction induced by the integral (E.3) is of order unity, which is very small compared to the uncertainties of the transport coefficients.

To find the value of $\tilde{E}^*$ we impose a toroidal loop voltage $V_T = 1V$. To have the corresponding electric field in the cross section V_T is divided by the toroidal length,

$$E_{section} = \frac{V_t}{2\pi R_0}. \tag{E.4}$$

To make this value dimensionless we divide $E_{section}$ by $C_a B_{JET}$ ($E^* = E_{section} \,/\, C_a B_{JET}$). With $C_a = B_{JET}/\sqrt{\rho\mu}$ the Alfvén velocity ($C_a = 7.2 \cdot 10^6\, ms^{-1}$), we recall that ρ is the density and μ is the permeability of free space. The integration of $\boldsymbol{E}_0^*$ over the cross section must be equal to the dimensionless value of the electric field E^*. As for the

toroidal magnetic field we write,

$$E^* = \frac{1}{A}\int_0^{2\pi}\int_0^{a} \tilde{E}^* \frac{R_0}{R_0 + rcos(P)} rdrdP. \tag{E.5}$$

Calculating this integral we find $\tilde{E}^* = 2.5 \cdot 10^{-9}$. Then we fix the resistive Lundquist number (S) to have the toroidal current $I = 3.1$ MA. The value of S is determined using the conductivity σ and considering Ohm's law:

$$I = A\ \sigma E_{section}, \tag{E.6}$$

The formula used to find the resistive Lundquist number (S) is:

$$S = C_a L \sigma \frac{4\pi \cdot 9 \cdot 10^9}{c^2}. \tag{E.7}$$

with L the diameter of the cross section (see Fig. E.1) and c the speed of light. The coefficient $4\pi \cdot 9 \cdot 10^9/c^2$ allows us to pass from SI units to cgs units. This way we can compare with the value in the literature [51].

Now we can calculate the dimensionless poloidal magnetic field ($\boldsymbol{B}^*_{0_{pol}}$) induced by the dimensionless toroidal electric field ($\boldsymbol{E}^*_0$). First we consider the dimensional Ampère's law:

$$\nabla \times \boldsymbol{B} = \mu \boldsymbol{j}. \tag{E.8}$$

The second equation needed is the relation between a dimensionless and a dimensional electric field,

$$\boldsymbol{E}^* = \frac{\boldsymbol{E}}{C_a B_{JET}}, \tag{E.9}$$

with $\boldsymbol{E}^*$ being the dimensionless field. We replace the current density in Eq. (E.8) by Eq. (E.9) taking into account Ohm's law ($\boldsymbol{j} = \sigma \boldsymbol{E}$),

$$\nabla \times \boldsymbol{B} = \mu \sigma B_{JET} C_a \boldsymbol{E}^*. \tag{E.10}$$

To make dimensionless this last equation we divide it by B_{JET}/L,

$$\nabla \times \boldsymbol{B}^* = \underbrace{C_a L \sigma \mu}_{S} \boldsymbol{E}^* \tag{E.11}$$

Then we can introduce the dimensionless irrotational electric field profile presented in Eq. (E.1),

$$\nabla \times \boldsymbol{B}^*_{0_{pol}} = S\boldsymbol{E}^*_0. \tag{E.12}$$

We consider a constant resistivity hence the current density profile is proportional to the electric field profile. The relation between the dimensionless imposed current density ($\boldsymbol{j}_0$) and electric field ($\boldsymbol{E}_0$) is the following,

$$\boldsymbol{j}^*_0 = S\boldsymbol{E}^*_0. \tag{E.13}$$

Finally the dimensionless Ampère's law can be written,

$$\nabla \times \boldsymbol{B}^*_{0_{pol}} = \boldsymbol{j}^*_0. \tag{E.14}$$

This equation for $\boldsymbol{B}^*_{0_{pol}}$ can be solved numerically (see Appendix D) considering the solenoidal constraint, and imposing the normal component of the poloidal magnetic field vanishing at the wall as boundary condition.

The resistive Lundquist number is calculated for the circular cross section,

$$S = C_a L \sigma \mu \approx 1.19 \cdot 10^8 \tag{E.15}$$

The characteristic length is $L = a/(0.3\pi)$ because in the numerical code the minor radius has a length of 0.3π ($a = 1.5\,m$ is the real length of the minor radius for JET).

The viscous Lundquist number is defined as $M = C_a L/\nu$. The high boundary of the value of the kinematic viscosity is $\nu = 1.25 \cdot 10^{11} m^2 s^{-1}$. In fact for a magnetofluid exposed to a strong magnetic field a complicated viscous stress tensor results [13] with different viscosity coefficient that span about twelve orders of magnitude [68]. So we have $1.25 \cdot 10^{11} m^2 s^{-1} > \nu > 1.25 \cdot 10^{-1} m^2 s^{-1}$ [51]. For the circular cross section the viscous Lundquist number is,

$$M \in [9.18 \cdot 10^{-5}, 9.18 \cdot 10^7]. \tag{E.16}$$

If we use the arbitrary value $\nu = 1 m^2 s^{-1}$, we find $M = 1.51 \cdot 10^7$. Which is at present impossible to take into account numerically.

To summarize, the parameters of JET tokamak are presented in Tab. E.1. Note that other characteristic quantities of the spherical tokamak NSTX can be found in the Appendix A of the article by Ferraro and Jardin [33].

Parameters	**Values**	**Formula**
Major radius R_0	3 m	
Minor radius a	1.5 m	
Minor radius in the code	0.3π	
Characteristic length L	≈ 1.6	$L = \frac{a}{0.3\pi}$
Root mean square value of toroidal field B_{JET}	2.8 T (Tesla) $\left(\frac{k_g}{As^2}\right)$	
$\tilde{B}^*$ (found in the formula: $\boldsymbol{B}_0^*(R,Z) = \tilde{B}^* \frac{R_0}{R} \boldsymbol{e}_T$)	0.94 (circular cross section)	$\overline{\boldsymbol{B}_0^*} = \frac{1}{A}\int_A \frac{\tilde{B}^*}{R_0 + rcos(P)} rdrdP = 1$
Toroidal loop voltage (arbitrary)	1V $\left(\frac{k_g m^2}{As^3}\right)$	
Plasma density (deuterium + electrons) ρ	$1.2 \cdot 10^{-7}$ kg/m^3 or $3.6 \cdot 10^{19}$ m^{-3}	
Vacuum Permeability μ	$4\pi \cdot 10^{-7}$ Vs/(Am)	
Alfvén velocity C_a	$7.2 \cdot 10^6$ m/s	$B_{JET}/\sqrt{\rho\mu}$
Reference electric field	$2.019 \cdot 10^7$ V/m	$C_a B_{JET}$
Toroidal current I	$3.1 \cdot 10^6$ A	
Dimensionless applied electric $\tilde{E}^*$ (found in the formula: $\boldsymbol{E}_0^*(R,Z) = \tilde{E}^* \frac{R_0}{R} \boldsymbol{e}_T$)	$2.5 \cdot 10^{-9}$	$\overline{\boldsymbol{E}_0^*} = \frac{1}{A}\int_A \frac{\tilde{E}^*}{R_0 + rcos(P)} rdrdP = \frac{1V}{2\pi R_0 C_a \tilde{B}}$
Dimensionless applied current density field $\tilde{j}^*$ (found in the formula: $\boldsymbol{j}_0^*(R,Z) = \tilde{j}^* \frac{R_0}{R} \boldsymbol{e}_T$)	0.298	$\tilde{j}^* = S\tilde{E}^*$
Plasma conductivity σ allowing to have a current of 3.1 MA	$8.27 \cdot 10^6$ Siemens / m (circular cross section)	$\sigma = \frac{I}{AE_{section}}$
S	$1.19 \cdot 10^8$ (circular cross section)	$S = C_a L \sigma \mu$
M	$9.18 \cdot 10^{-5}$ to $9.18 \cdot 10^7$ (circular cross section)	$M = \frac{C_a L}{\nu}$

Table E.1: JET tokamak parameters.

F

LARGE SCALE FORCING OF A PLASMA DYNAMO

The generation of planetary magnetic fields through the turbulent movement of liquid metals in the core is an intriguing phenomenon. It is not only an important issue in geophysics, but also explains the self-organization in Reversed Field Pinch plasma devices. This so called dynamo effect is now reproduced in several experimental set-ups such as the VKS experiment in Cadarache [67], but the detailed physics are still poorly understood. One drawback in the liquid metal experiments is the very low value of the magnetic Prandtl number. Liquid metal experiments require therefore a huge kinetic Reynolds number to obtain only a moderate magnetic Reynolds number. For this reason the construction of a plasma dynamo has been undertaken at the Laboratoire de Physique of the Ecole Normale Supérieure de Lyon. The use of a plasma instead of a liquid metal allows the experiment to attain larger magnetic Reynolds numbers at moderate kinetic Reynolds numbers. The measurement of the dynamics in a plasma experiment, and the forcing of the large scale flow field, is however highly nontrivial. Therefore, in parallel with the experiment, we investigate the plasma dynamics by direct numerical simulations[§].

In this work we model the plasma vessel by imposing solid, no-slip boundary conditions at the walls of a cylinder, periodic in the axial direction. An imposed magnetic field B_0 is pointing in the axial direction. An electric field is created in the radial direction as illustrated in Fig. F.1. The hereby generated current induces a Lorentz force in the azimuthal direction. It is this Lorentz force which is supposed to induce a large scale motion.

For the preliminary results presented here the viscous and resistive Lundquist numbers

[§]This investigation is carried out in collaboration with Francesco Palermo, Fabien S. Godeferd and Nicolas Plihon.

are $M = S = 10$, corresponding to unity magnetic Prandtl number. The imposed electric field, magnetic field and current density are given the value $E_0 = 5$ and $B_0 = 0.5$ and $j_0 = 50$, respectively. Preliminary results are shown in Fig. F.1 (right) in which it is shown how the plasma is set into movement in the horizontal plane containing the electrodes. Three-dimensional flow visualizations are shown in Fig. F.2, where it is observed that a dipolar velocity structure is created in the plasma.

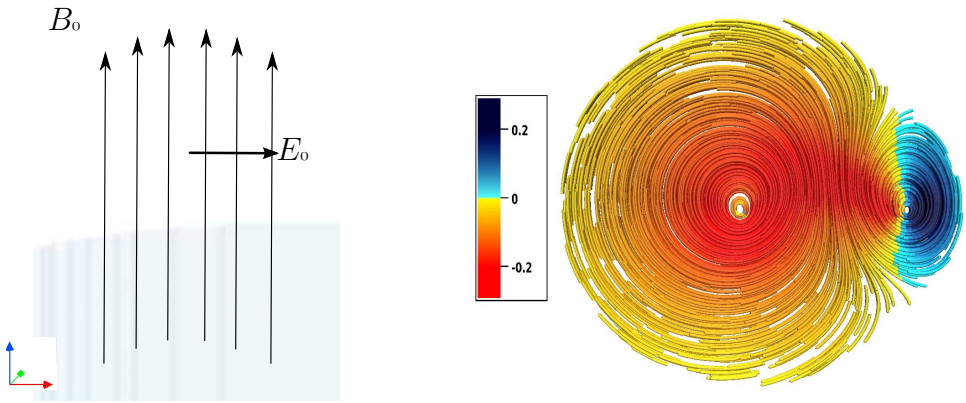

Figure F.1: Studied geometry and imposed fields (left). Two dimensional velocity streamlines colored with the azimuthal velocity in a horizontal plane at the axial coordinate where the electric field is introduced (right).

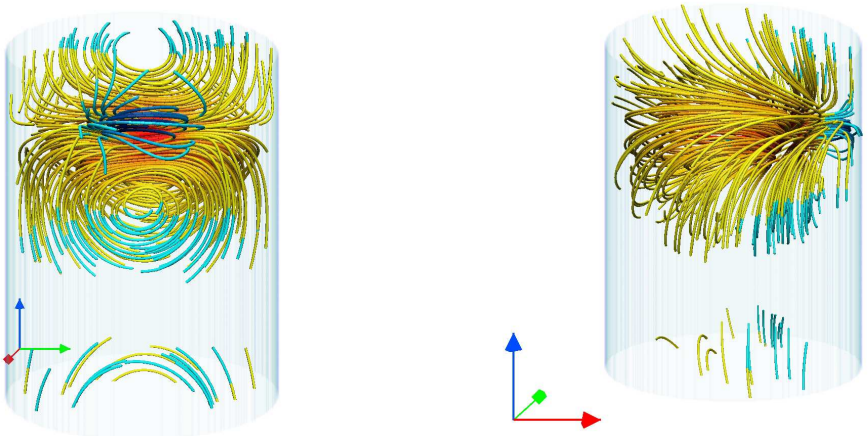

Figure F.2: Three dimensional velocity streamlines colored with the azimuthal velocity for early time simulations at low magnetic and kinetic Reynolds numbers. Two views: from a direction orthogonal to the imposed radial electric field (left), and along the imposed radial electric field (right).

BIBLIOGRAPHY

[1] P. ANGOT, C.-H. BRUNEAU AND P. FABRIE. A penalization method to take into account obstacles in incompressible viscous flows. *Numerische Mathematik*, 81(4):497–520, 1999.

[2] P. ANGOT AND J.-P. CALTAGIRONE. New graphical and computational architecture concept for numerical simulation on supercomputers. *Proc. of 2nd World Cong. on Comp. Mech.*, 1(8):973–976, 1990.

[3] E. ARQUIS AND J.-P. CALTAGIRONE. Sur les conditions hydrodynamiques au voisinage d'une interface milieu fluide-milieux poreux: application à la convection naturelle. *C.R. Acad. Sci.*, 299:1–4, 1984.

[4] A. AYDEMIR, D. BARNES, E. CARAMANA, A. MIRIN, R. NEBEL, D. SCHNACK AND A. SGRO. Compressibility as a feature of field reversal maintenance in the reversed-field pinch. *Phys. of Fluids*, 28:898, 1985.

[5] J. BATES AND R. LEWIS. A toroidal boundary-value problem in resistive magnetohydrodynamics. *Phys. of Plasmas*, 3:2395, 1996.

[6] J. BATES AND D. MONTGOMERY. Toroidal visco-resistive magnetohydrodynamic steady states contain vortices. *Phys. of Plasmas*, 5:2649, 1998.

[7] J. BERKOWITZ, H. GRAD AND H. RUBIN. Proceedings of the Second United Nations International Conference on the Peaceful Uses of Atomic Energy, Geneva, 1958.

[8] D. BONFIGLIO, S. CAPPELLO AND D. ESCANDE. Dominant electrostatic nature of the reversed field pinch dynamo. *Phys. Rev. Lett.*, 94(14):145001, 2005.

[9] D. BONFIGLIO, L. CHACÓN AND S. CAPPELLO. Nonlinear three-dimensional verification of the SPECYL and PIXIE3D magnetohydrodynamics codes for fusion plasmas. *Phys. of Plasmas*, 17:082501, 2010.

[10] F. BONOMO, D. BONFIGLIO, P. PIOVESAN, L. PIRON, B. ZANIOL, S. CAPPELLO, L. CARRARO, R. CAVAZZANA, M. GOBBIN, L. MARRELLI *et al.* Flow measurements and modelling in helical RFX-mod equilibria. *Nuclear Fusion*, 51(12):123007, 2011.

[11] W. BOS, S. NEFFAA AND K. SCHNEIDER. Rapid generation of angular momentum in bounded magnetized plasma. *Phys. Rev. Lett.*, 101(23):235003, 2008.

[12] W. BOS, S. NEFFAA AND K. SCHNEIDER. Self-organization and symmetry-breaking in two-dimensional plasma turbulence. *Phys. of Plasmas*, 17:092302, 2010.

[13] S. BRAGINSKII. Transport processes in a plasma. *Reviews of Plasma Phys.*, 1:205, 1965.

[14] P. BRUNSELL, Y. YAGI, Y. HIRANO, Y. MAEJIMA AND T. SHIMADA. Coherent magnetic field fluctuations and locked modes in a reversed-field pinch. *Phys. of Fluids B: Plasma Phys.*, 5:885, 1993.

[15] Y. CAMENEN, A. BORTOLON, B. DUVAL, L. FEDERSPIEL, A. PEETERS, F. CASSON, W. HORNSBY, A. KARPUSHOV, F. PIRAS, O. SAUTER *et al.* Experimental demonstration of an up-down asymmetry effect on intrinsic rotation in the TCV tokamak. *Plasma Phys. and Controlled Fusion*, 52(12):124037, 2010.

[16] Y. CAMENEN, A. PEETERS, C. ANGIONI, F. CASSON, W. HORNSBY, A. SNODIN AND D. STRINTZI. Transport of parallel momentum induced by current-symmetry breaking in toroidal plasmas. *Phys. Rev. Lett.*, 102:125001, 2009.

[17] C. CANUTO, M. HUSSAINI, A. QUARTERONI AND T. ZANG. *Spectral Methods in Fluid Dynamics*. Springer, 1987.

[18] S. CAPPELLO. Bifurcation in the MHD behaviour of a self-organizing system: the reversed field pinch (RFP). *Plasma Phys. and Controlled Fusion*, 46(12B):B313, 2004.

[19] S. CAPPELLO, D. BONFIGLIO, D. ESCANDE, S. GUO, A. ALFIER, R. LORENZINI AND R. TEAM. The reversed field pinch toward magnetic order: a genuine self-organization. In *AIP Conference Proceedings*, volume 1069, page 27, 2008.

[20] S. CAPPELLO, D. BONFIGLIO, D. ESCANDE, S. GUO, I. PREDEBON, F. SATTIN, M. VERANDA, P. ZANCA, C. ANGIONI, L. CHACON *et al.* Equilibrium and transport for quasi-helical reversed field pinches. *Nuclear Fusion*, 51(10):103012, 2011.

[21] S. CAPPELLO AND D. ESCANDE. Bifurcation in viscoresistive MHD: The Hartmann number and the reversed field pinch. *Phys. Rev. Lett.*, 85(18):3838, 2000.

[22] G. CARBOU AND P. FABRIE. Boundary layer for a penalization method for viscous incompressible flow. *Adv. Differ. Equat.*, 8:1453, 2003.

[23] L. CARRARO, A. ALFIER, F. BONOMO, A. FASSINA, M. GOBBIN, R. LORENZINI, P. PIOVESAN, M. PUIATTI, G. SPIZZO, D. TERRANOVA *et al.* Improved confinement with internal electron transport barriers in RFX-mod. *Nuclear Fusion*, 49(5):055009, 2009.

[24] L. CHACÓN. An optimal, parallel, fully implicit Newton–Krylov solver for three-dimensional viscoresistive magnetohydrodynamics. *Phys. of Plasmas*, 15(5):056103, 2008.

[25] S. CHANDRASEKHAR. *Hydrodynamic and hydromagnetic stability*. Dover Pubns, 1961.

[26] J. DAHLBURG, D. MONTGOMERY, G. DOOLEN AND L. TURNER. Driven, steady-state RFP computations. *J. Plasma Phys.*, 40(01):39–68, 1988.

[27] P. DAVIDSON. *An introduction to magnetohydrodynamics*. Cambridge Univ. Press, 2001.

[28] P. DIAMOND, C. MCDEVITT, Ö. GÜRCAN, T. HAHM, W. WANG, E. YOON, I. HOLOD, Z. LIN, V. NAULIN AND R. SINGH. Physics of non-diffusive turbulent transport of momentum and the origins of spontaneous rotation in tokamaks. *Nuclear Fusion*, 49(4):045002, 2009.

[29] J. DIMARCO. The ZT-40M experiment. *Proc. of the International School of Plasma Physics, Course on Mirx_r-Based and Field-Reversed Approaches to Magnetic Fusion, Villa Monastero, Varenna, Italy*, 2, 1983.

[30] W. DING, L. LIN, D. BROWER, A. ALMAGRI, B. CHAPMAN, G. FIKSEL, D. DEN HARTOG AND J. SARFF. Kinetic stress and intrinsic flow in a toroidal plasma. *Phys. Rev. Lett.*, 110(6):065008, 2013.

[31] D. ESCANDE, S. CAPPELLO, F. D'ANGELO, P. MARTIN, S. ORTOLANI AND R. PACCAGNELLA. Single helicity: a new paradigm for the reversed field pinch. *Plasma Phys. and Controlled Fusion*, 42(12B):B243, 2000.

[32] D. ESCANDE, P. MARTIN, S. ORTOLANI, A. BUFFA, P. FRANZ, L. MARRELLI, E. MARTINES, G. SPIZZO, S. CAPPELLO, A. MURARI, R. PASQUALOTTO AND P. ZANCA. Quasi-single-helicity reversed-field-pinch plasmas. *Phys. Rev. Lett.*, 85(8):1662–5, 2000.

[33] N. FERRARO AND S. JARDIN. Calculations of two-fluid magnetohydrodynamic axisymmetric steady-states. *J. Comp. Phys.*, 228(20):7742–7770, 2009.

[34] L. FRASSINETTI, P. BRUNSELL AND J. DRAKE. Experiments and modelling of active quasi-single helicity regime generation in a reversed field pinch. *Nuclear Fusion*, 49(7):075019, 2009.

[35] J. FREIDBERG. *Plasma Phys. and Fusion Energy*. Cambridge Univ Pr, 2007.

[36] C. GISSINGER, H. JI AND J. GOODMAN. Instabilities in magnetized spherical Couette flow. *Phys. Rev. E*, 84(2):026308, 2011.

[37] M. GOBBIN, L. MARRELLI AND R. WHITE. Numerical studies of transport mechanisms in RFX-mod low magnetic chaos regimes. *Plasma Phys. and Controlled Fusion*, 51(6):065010, 2009.

[38] J.-L. GUERMOND, R. LAGUERRE, J. LÉORAT AND C. NORE. An interior penalty Galerkin method for the MHD equations in heterogeneous domains. *J. Comp. Phys.*, 221(1):349–369, 2007.

[39] J.-L. GUERMOND, R. LAGUERRE, J. LÉORAT AND C. NORE. Nonlinear magnetohydrodynamics in axisymmetric heterogeneous domains using a Fourier/finite element technique and an interior penalty method. *J. Comp. Phys.*, 228(8):2739–2757, 2009.

[40] J.-L. GUERMOND, J. LÉORAT AND C. NORE. A new Finite Element Method for magneto-dynamical problems: two-dimensional results. *Eur. J. of Mech. - B/Fluids*, 22(6):555–579, 2003.

[41] C. GUTHMANN AND J. RAX. *Physique des Plasmas*. Dunod, 2005.

[42] G. HUYSMANS, S. PAMELA, E. VAN DER PLAS AND P. RAMET. Non-linear MHD simulations of edge localized modes (ELMs). *Plasma Phys. and Controlled Fusion*, 51(12):124012, 2009.

[43] R. IKEZOE, K. OKI, T. ONCHI, Y. KONISHI, M. SUGIHARA, S. FUJITA, A. SANPEI, H. HIMURA AND S. MASAMUNE. Extended operational regimes and MHD behavior in a low-aspect-ratio reversed field pinch in RELAX. *Plasma Phys. and Controlled Fusion*, 53(2):025003, 2011.

[44] R. IKEZOE, T. ONCHI, K. OKI, A. SANPEI, H. SHIMAZU, T. YAMASHITA, H. HIMURA AND S. MASAMUNE. Characterization of equilibria in a low-aspect-ratio RFP. *J. Plasma Fusion Res. SERIES*, 8:1066, 2009.

[45] A. ISKAKOV, S. DESCOMBES AND E. DORMY. An integro-differential formulation for magnetic induction in bounded domains: boundary element-finite volume method. *J. Comp. Phys.*, 197(2):540–554, 2004.

[46] S. JARDIN. Review of implicit methods for the magnetohydrodynamic description of magnetically confined plasmas. *J. Comp. Phys.*, 231(3):822–838, 2012.

[47] C. JAUSE-LABERT, F. GODEFERD AND B. FAVIER. Numerical validation of the volume penalization method in three-dimensional pseudo-spectral simulations. *Computers & Fluids*, 2012.

[48] JET-TEAM. Fusion energy production from a deuterium-tritium plasma in the JET tokamak. *Nuclear Fusion*, 32(2):187, 1992.

[49] B. KADOCH, D. KOLOMENSKIY, P. ANGOT AND K. SCHNEIDER. A volume penalization method for incompressible flows and scalar advection–diffusion with moving obstacles. *J. Comp. Phys.*, 231(12):4365–4383, 2012.

[50] L. KAMP AND D. MONTGOMERY. Toroidal flows in resistive magnetohydrodynamic steady states. *Phys. of Plasmas*, 10:157, 2003.

[51] L. KAMP AND D. MONTGOMERY. Toroidal steady states in visco-resistive magnetohydrodynamics. *J. Plasma Phys.*, 70(2):113–142, 2004.

[52] D. KOLOMENSKIY AND K. SCHNEIDER. A Fourier spectral method for the Navier–Stokes equations with volume penalization for moving solid obstacles. *J. Comp. Phys.*, 228:5687–5709, 2009.

[53] R. LAGUERRE, C. NORE, J. LÉORAT AND J.-L. GUERMOND. Induction effects in isolated axisymmetric conductors using a new finite element method. In *Proc. of the Summer Program*, page 1, 2004.

[54] S. LAIZET AND E. LAMBALLAIS. High-order compact schemes for incompressible flows: A simple and efficient method with quasi-spectral accuracy. *J. Comp. Phys.*, 228(16):5989–6015, 2009.

[55] Q. LIU AND O. VASILYEV. A Brinkman penalization method for compressible flows in complex geometries. *J. Comp. Phys.*, 227(2):946–966, 2007.

[56] R. LORENZINI, E. MARTINES, P. PIOVESAN, D. TERRANOVA, P. ZANCA, M. ZUIN, A. ALFIER, D. BONFIGLIO, F. BONOMO, A. CANTON *et al.* Self-organized helical equilibria as a new paradigm for ohmically heated fusion plasmas. *Nature Phys.*, 5(8):570–574, 2009.

[57] R. LORENZINI, D. TERRANOVA, A. ALFIER, P. INNOCENTE, E. MARTINES, R. PASQUALOTTO AND P. ZANCA. Single-helical-axis states in reversed-field-pinch plasmas. *Phys. Rev. Lett.*, 101(2):025005, 2008.

[58] H. LÜTJENS AND J.-F. LUCIANI. XTOR-2F: a fully implicit Newton–Krylov solver applied to nonlinear 3D extended MHD in tokamaks. *J. Comp. Phys.*, 229(21):8130–8143, 2010.

[59] J. MANICKAM. Stability of n=1 internal modes in tokamaks. *Nuclear Fusion*, 24(5):595, 1984.

[60] P. MARTIN, L. APOLLONI, M. PUIATTI, J. ADAMEK, M. AGOSTINI, A. ALFIER, S. ANNIBALDI, V. ANTONI, F. AURIEMMA, O. BARANA *et al.* Overview of RFX-mod results. *Nuclear Fusion*, 49(10):104019, 2009.

[61] P. MARTIN, A. BUFFA, S. CAPPELLO, F. D'ANGELO, D. ESCANDE, P. FRANZ, L. MARRELLI, E. MARTINES, S. ORTOLANI, G. SPIZZO, R. BILATO, T. BOLZONELLA, S. COSTA, A. MURARI, R. PACCAGNELLA, R. PASQUALOTTO, D. TERRANOVA AND P. ZANCA. Quasi-single helicity states in the reversed field pinch: Beyond the standard paradigm. *Phys. of Plasmas*, 7(5):1984, 2000.

[62] P. MARTIN, L. MARRELLI, A. ALFIER, F. BONOMO, D. ESCANDE, P. FRANZ, L. FRASSINETTI, M. GOBBIN, R. PASQUALOTTO, P. PIOVESAN *et al.* A new paradigm for RFP magnetic self-organization: results and challenges. *Plasma Phys. and Controlled Fusion*, 49(5A):A177, 2007.

[63] N. MATTOR AND P. DIAMOND. Momentum and thermal transport in neutral-beam-heated tokamaks. *Phys. of Fluids*, 31:1180, 1988.

[64] P. MININNI AND D. MONTGOMERY. Magnetohydrodynamic activity inside a sphere. *Phys. of Fluids*, 18:116602, 2006.

[65] P. MININNI, A. POUQUET AND D. MONTGOMERY. Small-Scale Structures in Three-Dimensional Magnetohydrodynamic Turbulence. *Phys. Rev. Lett.*, 97(24):1–4, 2006.

[66] N. MIZUGUCHI, A. SANPEI, S. FUJITA, K. OKI., H. HIMURA., S. MASAMUNE AND K. ICHIGUCHI. Modeling of formation of helical structures in reversed-field pinch. *Plasmas and Fusion Research: Regular Articles*, 7:2403117, 2012.

[67] R. MONCHAUX, M. BERHANU, M. BOURGOIN, M. MOULIN, P. ODIER, J.-F. PINTON, R. VOLK, S. FAUVE, N. MORDANT, F. PÉTRÉLIS *et al.* Generation of a magnetic field by dynamo action in a turbulent flow of liquid sodium. *Phys. Rev. Lett.*, 98(4):044502, 2007.

[68] D. MONTGOMERY, J. BATES AND L. KAMP. MHD steady states as a model for confined plasmas. *Plasma Phys. and Controlled Fusion*, 41(3A):A507, 1999.

[69] D. MONTGOMERY, J. BATES AND R. LEWIS. Resistive magnetohydrodynamic equilibria in a torus. *Phys. of Plasmas*, 4(4):1080, 1997.

[70] D. MONTGOMERY, J. BATES AND S. LI. Toroidal vortices in resistive magnetohydrodynamic equilibria. *Phys. of Plasmas*, 9(4):1188, 1996.

[71] D. MONTGOMERY, L. PHILLIPS AND M. THEOBALD. Helical, dissipative, magnetohydrodynamic states with flow. *Phys. Rev. A*, 40(3):1515, 1989.

[72] D. MONTGOMERY AND X. SHAN. Toroidal resistive MHD equilibria. *Comments Plasma Phys. Controlled Fusion*, 15:315, 1994.

[73] J. MORALES, W. BOS, K. SCHNEIDER AND D. MONTGOMERY. Intrinsic rotation of toroidally confined magnetohydrodynamics. *Phys. Rev. Lett.*, 109:175002, 2012.

[74] J. MORALES, W. BOS, K. SCHNEIDER AND D. MONTGOMERY. Magneto-hydrodynamically generated velocities in confined plasma. *http://hal.archives-ouvertes.fr/hal-00849742*, 2013.

[75] J. MORALES, M. LEROY, W. BOS AND K. SCHNEIDER. Simulation of confined magnetohydrodynamic flows using a pseudo-spectral method with volume penalization. *http://hal.archives-ouvertes.fr/hal-00719737*, 2012.

[76] S. NEFFAA, W. BOS AND K. SCHNEIDER. The decay of magnetohydrodynamic turbulence in a confined domain. *Phys. of Plasmas*, 15:092304, 2008.

[77] P. NORDLUND. The structure and stability of the reversed field pinch magnetic equilibrium in Extrap T1. *Physica Scripta*, 49(2):239, 1994.

[78] M. ONOFRI. Single-helicity states in compressible magnetohydrodynamics simulations of the reversed-field pinch with nonuniform resistivity. *Nuclear Fusion*, 51(11):112003, 2011.

[79] M. ONOFRI, F. MALARA AND P. VELTRI. Compressibility effects in the dynamics of the reversed-field pinch. *Phys. Rev. Lett.*, 101(25):255002, 2008.

[80] M. ONOFRI, F. MALARA AND P. VELTRI. Effects of compressibility and heating in magnetohydrodynamics simulations of a reversed field pinch. *Phys. of Plasmas*, 16:052508, 2009.

[81] A. PEETERS, C. ANGIONI, A. BORTOLON, Y. CAMENEN, F. CASSON, B. DUVAL, L. FIEDERSPIEL, W. HORNSBY, Y. IDOMURA, T. HEIN *et al.* Overview of toroidal momentum transport. *Nuclear Fusion*, 51(9):094027, 2011.

[82] C. PESKIN. The immersed boundary method. *Acta Num.*, 11(1):479–517, 2002.

[83] D. PFIRSCH AND A. SCHLÜTER. Der Einfluss der elektrischen Leitfähigkeit auf das Gleichgewichtsverhalten von Plasmen niedrigen Drucks in Stelleratoren. Technical Report MPI/PA/7/62, Max-Planck-Institut, Munich, 1962.

[84] P. PIOVESAN, D. CRAIG, L. MARRELLI, S. CAPPELLO AND P. MARTIN. Measurements of the MHD dynamo in the quasi-single-helicity reversed-field pinch. *Phys. Rev. Lett.*, 93(23):235001, 2004.

[85] P. PIOVESAN, M. ZUIN, A. ALFIER, D. BONFIGLIO, F. BONOMO, A. CANTON, S. CAPPELLO, L. CARRARO, R. CAVAZZANA, D. ESCANDE *et al.* Magnetic order and confinement improvement in high-current regimes of RFX-mod with MHD feedback control. *Nuclear Fusion*, 49(8):085036, 2009.

[86] S. PRAGER. Dynamo and anomalous transport in the reversed field pinch. *Plasma Phys. and Controlled Fusion*, 41(3A):A129, 1999.

[87] I. PREDEBON, L. MARRELLI, R. WHITE AND P. MARTIN. Particle-transport analysis in reversed field pinch helical states. *Phys. Rev. Lett.*, 93(14):145001, 2004.

[88] M. PUIATTI, M. VALISA, M. AGOSTINI, F. AURIEMMA, F. BONOMO, L. CARRARO, A. FASSINA, M. GOBBIN, R. LORENZINI, B. MOMO *et al.* Internal and external electron transport barriers in the RFX-mod reversed field pinch. *Nuclear Fusion*, 51(7):073038, 2011.

[89] K. REUTER, F. JENKO, C. FOREST AND R. BAYLISS. A parallel implementation of an MHD code for the simulation of mechanically driven, turbulent dynamos in spherical geometry. *Comp. Phys. Comm.*, 179(4):245–249, 2008.

[90] J. RICE, R. BOIVIN, P. BONOLI, J. GOETZ, R. GRANETZ, M. GREENWALD, I. HUTCHINSON, E. MARMAR, G. SCHILLING, J. SNIPES *et al.* Observations of impurity toroidal rotation suppression with ITB formation in ICRF and ohmic H mode Alcator C-Mod plasmas. *Nuclear Fusion*, 41(3):277, 2001.

[91] J. RICE, P. BONOLI, J. GOETZ, M. GREENWALD, I. HUTCHINSON, E. MARMAR, M. PORKOLAB, S. WOLFE, S. WUKITCH AND C. CHANG. Central impurity toroidal rotation in ICRF heated Alcator C-Mod plasmas. *Nuclear Fusion*, 39(9):1175, 1999.

[92] J. RICE, B. DUVAL, M. REINKE, Y. PODPALY, A. BORTOLON, R. CHURCHILL, I. CZIEGLER, P. DIAMOND, A. DOMINGUEZ, P. ENNEVER *et al.* Observations of core toroidal rotation reversals in Alcator C-mod ohmic L-mode plasmas. *Nuclear Fusion*, 51(8):083005, 2011.

[93] J. RICE, M. GREENWALD, Y. PODPALY, M. REINKE, P. DIAMOND, J. HUGHES, N. HOWARD, Y. MA, I. CZIEGLER, B. DUVAL *et al.* Ohmic energy confinement saturation and core toroidal rotation reversal in Alcator C-mod plasmas. *Phys. of Plasmas*, 19:056106, 2012.

[94] J. RICE, A. INCE-CUSHMAN, J. DEGRASSIE, L.-G. ERIKSSON, Y. SAKAMOTO, A. SCARABOSIO, A. BORTOLON, K. BURRELL, B. DUVAL, C. FENZI-BONIZEC, M. GREENWALD, R. GROEBNER, G. HOANG, Y. KOIDE, E. MARMAR, A. POCHELON AND Y. PODPALY. Inter-machine comparison of intrinsic toroidal rotation in tokamaks. *Nuclear Fusion*, 47(11):1618–1624, 2007.

[95] G. RÜDIGER AND D. SHALYBKOV. Stability of axisymmetric Taylor-Couette flow in hydromagnetics. *Phys. Rev. E*, 66(1):016307, 2002.

[96] J. SARFF, N. LANIER, S. PRAGER AND M. STONEKING. Increased confinement and β by inductive poloidal current drive in the reversed field pinch. *Phys. Rev. Lett.*, 78(1):62, 1997.

[97] A. SCARABOSIO, A. BORTOLON, B. DUVAL, A. KARPUSHOV AND A. POCHELON. Toroidal plasma rotation in the TCV tokamak. *Plasma Phys. and Controlled Fusion*, 48(5):663, 2006.

[98] K. SCHNEIDER. Numerical simulation of the transient flow behaviour in chemical reactors using a penalisation method. *Comput. & Fluids*, 34(10):1223–1238, 2005.

[99] V. SHAFRANOV. Plasma equilibrium in a magnetic field. *Reviews of Plasma Phys.*, 2:103, 1966.

[100] X. SHAN AND D. MONTGOMERY. Global searches of Hartmann-number-dependent stability boundaries. *Plasma Phys. Controlled Fusion*, 35:1019, 1993.

[101] X. SHAN AND D. MONTGOMERY. On the role of the Hartmann number in magnetohydrodynamic activity. *Plasma Phys. and Controlled Fusion*, 35(5):619, 1993.

[102] X. SHAN, D. MONTGOMERY AND H. CHEN. Nonlinear magnetohydrodynamics by Galerkin-method computation. *Phys. Rev. A*, 44(10):6800–6818, 1991.

[103] C. SUPLEE. *The plasma universe*. Cambridge Univ. Press, 2009.

[104] G. TAYLOR. Stability of a viscous liquid contained between two rotating cylinders. *Phil. Trans. of the Royal Soc. of London*, 223:289–343, 1923.

[105] J. TAYLOR. Relaxation of toroidal plasma and generation of reverse magnetic fields. *Phys. Rev. Lett.*, 33(19):1139, 1974.

[106] J. TAYLOR. Relaxation and magnetic reconnection in plasmas. *Reviews of Modern Phys.*, 58(3):741, 1986.

[107] H. TOYAMA, N. ASAKURA, K. HATTORI, N. INOUE, S. ISHIDA, S. MATSUZUKA, K. MIYAMOTO, J. MORIKAWA, Y. NAGAYAMA, H. NIHEI, S. SHINOHARA, Y. UEDA, K. YAMAGISHI AND Z. YOSHIDA. Unknown. In *Proceedings of the 12th European Conference on Controlled Fusion and Plasma Physics, Budapest*, volume I, page 602. L. Pocs and A. Montvai (European Physical Society, Geneva), 1985.

[108] M. VERANDA, D. BONFIGLIO, S. CAPPELLO, L. CHACÓN AND D. ESCANDE. Impact of helical boundary conditions on nonlinear 3D magnetohydrodynamic simulations of reversed-field pinch. *Plasma Phys. and Controlled Fusion*, 55(7):074015, 2013.

[109] F. WAGNER, G. BECKER, K. BEHRINGER, D. CAMPBELL, A. EBERHAGEN, W. ENGELHARDT, G. FUSSMANN, O. GEHRE, J. GERNHARDT, G. V. GIERKE, G. HAAS, M. HUANG, F. KARGER, M. KEILHACKER, O. KLÜBER, M. KORNHERR, K. LACKNER, G. LISITANO, G. G. LISTER, H. M. MAYER, D. MEISEL,

E. R. MÜLLER, H. MURMANN, H. NIEDERMEYER, W. POSCHENRIEDER, H. RAPP, H. RÖHR, F. SCHNEIDER, G. SILLER, E. SPETH, A. STÄBLER, K. H. STEUER, G. VENUS, O. VOLLMER AND Z. YÜ. Regime of improved confinement and high beta in neutral-beam-heated divertor discharges of the ASDEX tokamak. *Phys. Rev. Lett.*, 49:1408–1412, 1982.

[110] A. WILLIS AND C. BARENGHI. Hydromagnetic Taylor-Couette flow: numerical formulation and comparison with experiment. *J. Fluid Mech.*, 463(1):361–375, 2002.

[111] A. WILLIS AND C. BARENGHI. Hydromagnetic Taylor-Couette flow: wavy modes. *J. Fluid Mech.*, 472:399–410, 2002.